Université des Sciences et Technologies de Lille

N° d'ordre: 40137

THESE

pour obtenir le grade de :

Docteur de l'Université de Lille I

Spécialité :

Lasers, Molécules, Rayonnement Atmosphérique

Soutenue le 10 Décembre 2009 par

Neda BOYOUK

Titre :

Caractérisation des aérosols de pollution dans le Nord de la France: relation entre masse, propriétés optiques, distribution verticale et météorologie

JURY

Jean-Claude Roger, Professeur, Université Blaise Pascal	Rapporteur
Jacques Pelon, Directeur de recherche CNRS	Rapporteur
Jean-François Léon, Chargé de recherche CNRS	Examinateur
Isabelle Chiapello, Chargée de recherche CNRS	Examinateur
Hervé Delbarre, Professeur, Université du Littoral Côte d'Opale	Directeur de thèse

Laboratoire d'Optique Atmosphérique

U.F.R de Physique Fondamentale

Université des Sciences et Technologies de Lille

59655 Villeneuve d'Ascq

France

Résumé

Une atmosphère saine est un besoin élémentaire pour le bien être et la santé humaine. La matière particulaire en suspension (Particle Matter, PM) est bien connue pour avoir un impact significatif sur la santé. Les mesures de PM2.5 et PM10 au niveau du sol reflètent l'influence de la dynamique de la couche limite et du mélange des aérosols locaux ou advectés sur de grandes distances. Le lien entre épaisseur optique en aerosol (aerosol optical thickness, AOT) et PM dépend de la relation entre propriétés optiques et massiques et de la distribution verticale des particules dans l'atmosphère. Nous présentons 3 expériences de terrain dédiées à la caractérisation des aérosols de pollution dans le Nord de la France: la première lors d'un évenement de pollution printanier sur Lille, la seconde durant un événement de pollution hivernal sur Dunkerque et la troisième durant des occurrences de brise de mer sur le littoral Dunkerquois. Nous avons utilisé 2 systèmes Lidar différents, le premier dans le visible (532 nm) et le second dans l'UV (355 nm); un photomètre solaire automatique et des mesures de PM2.5 et PM10 par TEOM. L'altitude supérieure de la couche de mélange (mixed boundary layer, MBL) est détectée par Lidar et nous avons été capable de suivre le développement classique de la couche limite convective ainsi que des décroissances brutales d'altitude de la MBL dues à la brise de mer. Les profils d'extinction aérosols ont été estimés en utilisant un rapport Lidar de 67 sr à 532 nm à Lille, 77 sr à 532 nm et 30 sr à 355 nm à Dunkerque. Nous avons analysé l'impact du transport grande échelle de masses d'air polluée, du développement convectif de la MBL et du développement de la cellule de brise de mer sur les profils verticaux d'extinction en aérosols. Le signal Lidar dans les premières centaines de mètres est très bien corrélé (coefficient de corrélation supérieur à 0.9) avec les concentrations massiques mesurées au sol dans tous les cas. Il est également montré que l'introduction de la hauteur de la MBL permet une meilleure détermination des PM à partir de l'épaisseur optique.

Abstract

Clean air is considered to be a basic requirement for human health and well-being. Particulate matter is known to have a significant impact on health. The variability of Particle Matter (PM2.5 and PM10) concentrations recorded at ground-level is influenced by the boundary layer dynamics, local emissions, and advection and mixing of large scale transported aerosols. The link between columnar aerosol optical thickness (AOT) and ground-level PM depends on the relationship between mass and optical properties and on the vertical distribution of aerosols in the atmosphere. We present three field experiments dedicated to the characterization of pollution aerosols in the North of France: the first one during a spring pollution episode in metropolitan area of Lille (50.61°N, 3.14°E), the second one during a winter pollution episode in the industrial coastal city of Dunkerque (51°04′N; 2°38′E) and the third one during summer sea breezes on coastal area of Dunkerque. We have used 2 different Lidar systems, one in the UV (355 nm) and the other one in the visible (532 nm), an automatic sun photometer, and PM2.5 and PM10 measurements with TEOM. The mixed layer (MBL) top altitude is detected from the Lidar signal and we were able to monitor the classical diurnal evolution of the convective continental boundary as well as short-time decreases in the MBL height due to sea breeze occurrences. The aerosol extinction profiles were estimated using a Lidar ratio of 67 sr at 532 nm in Lille, and 77 sr at 532 nm and 30 sr at 355 m in Dunkerque. We have analyzed the impact of long range transport of polluted air masses, convective development of the MBL, and sea breeze development on the vertical profile of aerosol extinction coefficient. The Lidar signal in the first few hundred meters is well correlated (correlation coefficient above 0.9) with the PM concentrations in all cases. It is found that introducing the Lidar derived MBL height enable a better estimation of PM from measured AOT.

Remerciements:

Ce travail a été réalisé conjointement entre le Laboratoire Optique Atmosphérique de l'Université de Lille1(LOA-UMR 8515) et le Laboratoire de Physico-Chimie de l'Atmosphère de l'Université du Littoral-Côte d'Opale. Je remercie leurs directeurs, pour m'avoir accueillie au sein de leurs unités.

J'adresse également tous mes remerciement à celles et ceux qui ont accepté de participer au jury de cette thèse:

Messieurs Jean-Claude Roger et Jacques Pelon et Mademoiselle Isabelle Chiapello pour le temps qu'ils ont consacré à ce manuscrit et pour leurs questions et conseils. Je remercie, de même, l'Action Marie curie et la région Nord-Pas-de-Calais pour avoir soutenu financièrement cette thèse.

J'exprime toute ma gratitude à Monsieur Hervé Delbarre Professeur à l'Université du Littoral-Côte d'Opale pour m'avoir accueillie dans son équipe et la bonne ambiance qu'il a su instaurer. Je le remercie aussi pour le soutien qu'il m'a témoigné durant toutes ces années passées. Toute ma reconnaissance va également à mon codirecteur Jean François Léon, pour avoir guidé mes premiers pas, ses nombreux conseils ainsi que le temps qu'il a mis pour me corriger.

Je remercie, en particulier, Jean–Luc Deuzé, Didier Tanré pour le temps qu'ils ont consacré à m'écouter et répondre à mes questions et leurs soutiens psychologiques.
Je tiens également à remercier tous ceux avec qui j'ai collaboré durant ces trois années: Thierry Povdin, Patrick Augustin, Fabrice Ducos, Christine Deroo et Romain de Filippi.

J'ai eu la chance d'avoir le soutien psychologique des personnes du labratoire comme ma charmante Isabelle Jankowiak, et notamment pour le temps qu'elle a consacré à ma présentation.

Julie Letertre je te remercie pour les réponses à toutes mes questions sur la langue française. Michel Legrand, je vous remercie pour avoir écouter ma répétition. Céline Cornet, je te remercie pour ton aide sur la programmation de Matlab. Je remercie l'équipe Icare et je n'oublie pas l'équipe LOA.

Finalement, merci à mes superbes parents et mes soeurs, et Frank Wagner pour ses conseils scientifiques et son soutien psychologique.

Contents

Contents

Contents

General Introduction

Air pollution is a major issue for global environment as well as human health and well-being. Particulate air pollutants (particulate matter; PM or aerosols) consist of material in solid or liquid phase suspended in the atmosphere. They may be either emitted into the atmosphere (primary pollutants) or formed within the atmosphere itself (secondary pollutants). The concentration and composition of aerosols vary strongly in space and time, with a typical order from hours to weeks, depending mainly on the particle size, their pathway in the atmosphere and encountered meteorological conditions.

Aerosols have impact on human health. Indeed they can easily penetrate into the respiratory system (World Health Organization, 2006). Their impact on health depends on their physical and chemical properties, including size, shape, chemical composition and solubility. Due to its rather long atmospheric residence time, PM influences air quality far from its sources. PM also contributes to climate change (Forster et al., 2007). Indeed, the role of aerosols in the climate system is of primary importance. Aerosol has a direct impact on the Earth's radiative equilibrium by scattering and absorbing solar and thermal radiations. They also interact with the cloud properties and lifetime and thus exert an indirect effect on the radiative balance. Pollution aerosols augment cloud albedo and thus exert a cooling influence (Penner et al., 2001), while other studies find that the dark haze caused by pollution aerosols absorb solar radiation and reduce certain types of cloud coverage (Ackerman et al., 2000).

Due to importance of aerosol for climate, satellite remote sensing was extensively used for aerosol monitoring (Kaufman et al., 2002). Recently, satellites which are equipped with relevant air quality instruments have been placed into orbit (Tanré et al., 2001). However, aerosol remote sensing in the lowest first few hundred meters from space remains a challenging issue. Passive space remote sensors can measure quite accurately the aerosol optical depth of the whole atmosphere. But the contribution of boundary layer aerosol to the total aerosol optical depth can widely vary depending on local meteorology, including turbulence and convective mixing, or large-scale transport. Therefore, the vertical distribution of aerosols in the atmosphere has to be accounted for when demonstrating the relationship between the aerosol optical depth and air pollution.

The focus of this work is on the analysis of the relationship between ground-level PM observations, aerosol optical depth measurements and the aerosol vertical distribution in the atmosphere. The proposed strategy is based on field campaign measurements operated in the North of France in 2007 and 2008. The North of France is of a particular interest when studying aerosol transport in Europe. Indeed, this area is largely impacted by adverse effect of air pollution and especially particulate matter that conduct to one of the largest loss in statistical life expectancy (see Figure 0.1).

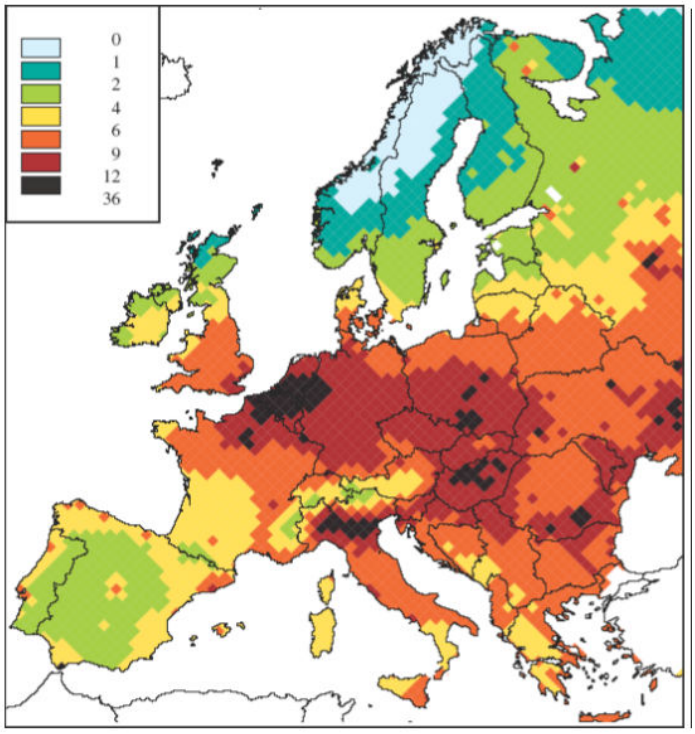

Figure 0.1 Loss in statistical life expectancy that can be attributed to the identified anthropogenic contributions to PM2.5 (in months) for the emissions of the year 2000 and the conditions of 1997 (after Aman et al. (2004)).

During the experiments, we first rely on measurements performed in the frame of operational networks for ground-level PM and aerosol optical measurements. Moreover, the vertical distribution is investigated by using laser soundings. Light detection and ranging is one of the most interesting fields for atmospheric vertical profiling. High spatial and temporal resolutions, observation of the ambient atmosphere, covering the whole troposphere and quantitative impression of aerosol vertical distribution lead us to choose Lidar as the most

effective instrument. The backscatter Lidar systems can monitor atmospheric parameters (backscatter coefficient, extinction coefficient and optical depth) and processes (boundary-layer growth, aerosol and cloud layering…). The influence of local meteorology, on aerosol properties and their mass concentration is also deeply analysed for each experiment. We have selected 3 different meteorological situations leading to pollution events. The first one corresponds to a classical spring pollution event with a continental scale advection of pollution aerosols. The second situation corresponds to a cold winter time pollution episode with a strong temperature inversion. Finally the last meteorological situation is dedicated to the summer time sea breeze influence on the level of pollution in the low level of atmosphere.

In the first chapter we introduce the aerosols, their physical and optical properties, and their transport pathways according to various scales (local, urban, global and continental). We also introduce the boundary layer and related local phenomena like sea breeze, as a key tool for mixing and contribution of aerosol and their dispersion. The second chapter is dedicated to the description of the applied tools and methods in the following chapters. The chapter 3 presents the study of a spring pollution episode in metropolitan area of Lille (50.61°N, 3.14°E). In this period the particle matter concentration passes the European-24 hour limit. This city has 1.2 million inhabitants and industries as source of pollution aerosol. Our objective is to examine the aerosol load during the pollution event and assess a relationship between the aerosol mass on the ground and the aerosol optical thickness considering the impact of boundary layer height calculated from Lidar signal. The chapter 4 is dedicated to a winter pollution episode in the industrial coastal city of Dunkerque (51°04′N; 2°38′E). Winter temperature inversions are for urban sites a major cause for exceeding air-quality legislation thresholds for most primary pollutants (Janhäll et al., 2006). This study is carried out to better understand the impact of regional transport on local aerosol pollution, aerosol optical properties and the role of meteorology on aerosol properties. Finally, chapter 5 presents a field experiment of summer sea breeze on industrial coastal area of Dunkerque. Typical sea breeze days in July have been chosen to investigate the variation of boundary layer height, mass concentration and aerosol optical thickness during the sea breeze.

1 Introduction to aerosol characterization and transport in the troposphere

1.1 Air pollution definition

Air pollution may be defined as a situation in which substances resulting from anthropogenic activities are present with sufficiently high concentrations in the air to produce a significant effect on humans, animals, vegetation or material. Historically, air pollution has been first associated with urban centers and industrialized regions. It is now clear that dense urban centers are just ''hotspots'' in a continuum of trace species concentrations over the entire Earth. The urban smog and stratospheric Ozone depletion explain this idea from the local to planetary scales.

One cubic centimeter of atmosphere air contains approximately $2.5x10^{19}$ molecules. About 10^3 of these molecules may be charged (ions). The molecules of N_2, O_2 and the various trace gases have sized (diameters) of 3 Angströms. The average distance between the molecules is about ten times the molecular size. In addition to the molecules and the ions, one cubic centimeter of air also contains a substantial number of particles varying in size from a few Angströms to several microns (µm). In relatively clean air there are about 10^3 particles per cm^3 with diameters from 1 nm to 50 µm while, in polluted air, this number may be 10^5 or more, including pollen, bacteria, dust and industrial emissions.

As an overview, the air constituents involved may be divided into the following four classes according to their chemical composition:

Nitrogen compounds: combustion sources as power plants and motor vehicles are sources of oxides of nitrogen (NO_x). The irradiation of a system containing these nitrogen and air compounds results in the oxidation of NO after the production of Ozone. However, the addition of organic compounds greatly accelerates the photo-oxidant processes.

Carbon compounds: many hydrocarbons, including aldehydes, ketones and unsaturated hydrocarbons are very reactive in the atmosphere and are collectively known as Reactive Hydrocarbons RHC. They occur from combustion of materials and emission from motor vehicles which contributes to 86% of the reactive oxidants found in large cities.

Sulphur compounds: these compounds SO_2 and H_2S, H_2SO_4, or sulphuric acid, which are advected in the main synoptic wind systems as a constituent of acid rain are produced due to SO_2 oxidization with water in the atmosphere.

Aerosols: the word aerosol was invented by Schmuss (German) in 1920. A suspension of solid, liquid or both particles in a gas medium (in air most of the time) is known as aerosol. It corresponds to air particles with a size ranging between 1 nanometer and 100 micrometers, coming from anthropogenic activities like transport, urban and industrial emissions, together with natural production like sea spray, volcanoes, mineral dust (soil particle).

With every breath, we take gases such as nitrogen dioxide and Ozone into our airways and lungs, with thousands of fine particles. They are deposited in the bronchi and alveoli, where they are able to exert their potential harmful effect. Among the many pollutants highlighted for their adverse health effect, a particular attention has been paid on fine particles, because they penetrate deeply into the lung. Extremely heavy pollutant loads frequently give rise to disturbances and diseases of the respiratory tract in children and adults (e.g. acute breathing difficulties, chronic coughing and expectoration, bronchitis and chronic bronchitis, and respiratory infections).

Various studies (Peters et al. 2001 ; Pope III et al. 1995; Samet et al. 2000) have provided evidence that PM10, and especially PM2.5 (which represents the size range of particles likely to pass through the nose and the mouth) are associated with a range of effects on humans, such as morbidity and mortality rates particularly due to cardiovascular and respiratory illness and atmospheric haze problems. Some trace elements present in PM2.5 are human or animal health hazard including As, Be, Cd, Cl, Co, Cr, Hg, Ni, Pb, Rn, and Se (IDEM, 2001). Elemental Carbon and organic Carbon which contains polycyclic aromatic hydrocarbon has the largest contribution to the particle. However, the underlying biological causes of the health effects of particles and their chemical composition exposures are not clear. Thus an investigation of their physical and chemical characteristics is carried out to explain in detail particles toxicity and evaluate urban air quality (Wang et al., 2006).

1.2 Particulate matter (air quality, size and chemical composition)

Particulate matter may be classified into different groups according to their health effect, size, origin, chemical composition, optical properties and lifetime.

1.2.1 Particulate matter and air quality network assessment

For assessing the air quality, the usual way to quantify the aerosols only refers to the particle mass concentration (in $\mu g.m^{-3}$) of PMx, meaning particles with an aerodynamic diameter lower than x (µm), measured at ground level. European community (1999/30/EC) established limit values and, as appropriate, alert thresholds for concentrations of sulphur dioxide, nitrogen dioxide and oxides of nitrogen and particulate matter to avoid, prevent or reduce harmful effects on human health specifically respiratory health and the environment as a whole.

The number of days with limit value does not have to exceed more than 35 days in a year. The U.S. Environment Protection Agency evaluates daily air quality based on the ratio between 24-hour averages of measured dry particulate mass and the National Ambient Air Quality Standard. The ratio is called air quality index (AQI).

The AQI and its corresponding 24h average of PM2.5 (μgm^{-3}) and air categories are presented in the Table 1.1. In unhealthy for sensitive group (USP) condition people with respiratory or heart disease, the elderly, and children should limit prolonged exertion. People with respiratory disease, such as asthma, should limit outdoor exertion. For unhealthy limit condition, everyone should limit prolonged exertion.

Table 1.1 AQI, its corresponding 24hourly mean PM2.5 (μgm^{-3}) and Air Quality Category, 24hrm is the daily average value. USP: Unhealthy for Sensitive Groups (elderly people, children and people with respiratory disease) (Wang and Christopher, 2003a).

	AQI						
	0~50	51~100	101~150	151~200	201~300	301~400	401~500
24 hrm PM2.5	0~15.4	15.5~40.4	40.5~65.4	65.5~150.4	150.5~250.4	250.5~350.4	350.5~500.4
AQC	good	Moderate	USP	Unhealthy	Very unhealthy	Hazardous	Hazardous

1.2.2 Aerodynamic diameter of particle matter

The aerodynamic diameter is defined as the diameter of a unit density sphere (density of 1 g/cm³) having the same settling velocity in air as the real particle, and has to be distinguished from its physical diameter. Particles with an aerodynamic diameter less than 57 µm are known as total suspended particulate matter (TSP) (Seinfeld and Pandis, 2006).

PM10 can be defined more precisely according to design of standard manual PM samplers. The inlets of the manual PM samplers are designed with specified 50% cut points (D_{50}), which are defined as the particle aerodynamic diameter at which 50% of the particles pass through the inlet and 50% are rejected. PM2.5 is the fine particles that pass through an inlet with a 50% cut point at 2.5 µm aerodynamic diameter. Ultrafine particles are the particle with an aerodynamic diameter less than 0.1 µm.

Figure 1.1 shows the observed aerosol modes according to the aerodynamic diameter for the range between 0.01 and 100 µm A) is the ultrafine particle including nucleation, B) accumulation mode is ranged between 0.1 and 2.5 µm and C) coarse mode are sized between 2 and 20 µm.

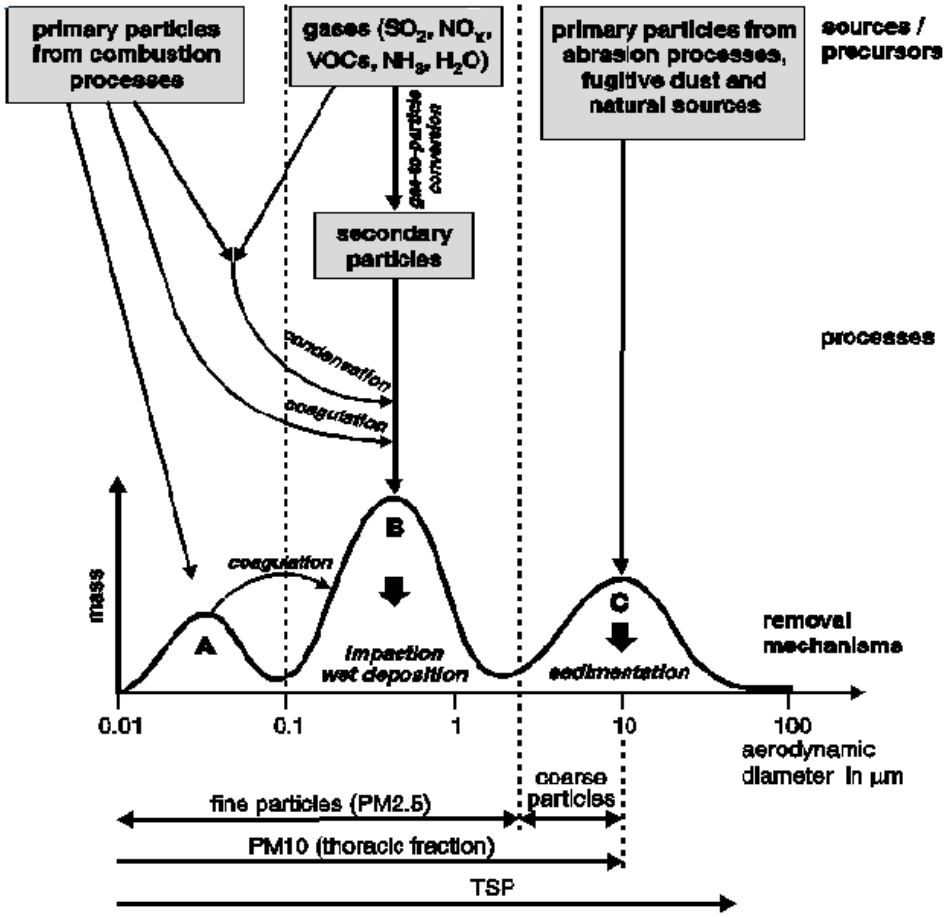

Figure 1.1 Simplified schematic view of the size ranges of atmospheric aerosols in the vicinity of the source and the principal processes involved A: ultra fine particles; B: accumulation mode; C: coarse particles (after (Kacenelenbogen, 2008))

Particle size distribution of urban aerosol is complex because it is a mixture of primary (soot, heavy metal) and secondary (organic carbon) aerosol. In urban areas, the nucleation, accumulation and coarse modes are the dominant modes. Fine particles include most of the total number and only a few percent fraction of mass. Coarse mode is primary but some secondary sulfates and nitrates exist (Seinfeld and Pandis, 2006). The marine aerosol size distribution includes three modes.

1.2.3 Chemical composition and origin of aerosol

Natural sources of particle matter include soil and terrestrial dust, volcanic action, sea spray, biomass burning and reaction between natural gaseous emissions whereas the anthropogenic sources are combustion, transport, fuel and other sources.

Table 1.2 Composition and source of particulate matter

Components		Precursor / cause
Primary components	Soot (EC and primary OC)	Combustion processes
	Geological material	Construction, agriculture, transport, wind
	Heavy metal	Combustion, production
	Abrasion particles	Mechanical shear forces
	Biological material	Fungus spores, plant fragments
Secondary components	Sulphate	Sulphur dioxide
	Nitrate	Nitrogen oxides
	Ammonium	Ammonia
	Organic carbon (OC)	VOC

Table 1.2 presents particles generated from natural and anthropogenic sources. The primary particle released directly to air and secondary particle formed in the atmosphere from precursor gases. Particle matter associated with human activities is produced in combustion processes, transportation, industrial process and construction. They are in the form of ultrafine and fine particles (e.g. soot, heavy metal). Particles in the secondary origin are formed by chemical conversion from SO_2, NO_x, NH_3, and non metal volatile organic compound precursors (ranged between 0.1 and 1µm).

1.3 Optical properties of atmospheric aerosols

1.3.1 Scattering, absorption and extinction

The optical properties of aerosols have been exhaustively described by numerous authors (Lenoble 1993; Liou 2002; Seinfeld and Pandis 2006) and I recall here the main features. Interaction between a light beam and a small particle, results into an oscillatory motion of electric charges in the particle. This oscillation generates electromagnetic radiation scattered

in all directions. A part of the incident radiation is also converted into thermal energy by absorption. The scattered energy F_{scat} (in W) by a particle is proportional to the incident intensity F_0 (in Wm^{-2}),

$$F_{scat} = C_{scat} F_0 \quad [1.1]$$

where the proportionality constant C_{scat} (m^2) may be considered as the single-particle scattering cross section. Similarly, we may define the absorbed energy F_{abs} (Wm^{-2}) also proportional to the incident intensity:

$$F_{abs} = C_{abs} F_0 \quad [1.2]$$

where C_{abs} (m^2) is the single-particle absorption cross section. The combined effect of the scattering and the absorption is referred to the extinction, and an extinction cross section (C_{ext}) can be defined by:

$$C_{ext} = C_{scat} + C_{abs} \quad [1.3]$$

C_{ext} in units of area is the surface of the particle shadow, which is quite different of the real geometrical shadow. The dimensionless scattering efficiency of a particle Q_{scat} is C_{scat}/A where A is the cross- sectional area of the particle. Defining Q_{abs} and Q_{ext} in the same way, we obtain:

$$Q_{ext} = Q_{scat} + Q_{abs} \quad [1.4]$$

1.3.2 Aerosol Single scattering albedo

Aerosol single scattering albedo ω_0 is a first factor imposing aerosol radiative effect. It is a measure of the effectiveness of scattering relative to total light extinction (which is also termed 'attenuance' and is the sum of scattering and absorption) for the light encountering the atmospheric aerosol particles. It is a dimensionless quantity and ranges from 0 to 1. Hansen et al. (1997) show that single scattering albedo determines the sign (cooling/heating, depending on the planetary albedo) of the aerosol radiative forcing, while the asymmetry of the phase function together with optical thickness drive the magnitude of the aerosol forcing. Most of the aerosol optical models (Hess et al. 1998; Koepke and Hess 1988; Shettle and Fenn 1979) associate aerosol radiative properties, aerosol optical thickness, phase function, and single scattering albedo, with physical and chemical characteristics of the atmospheric aerosol: particle sizes, shape, and composition. The values of the single

scattering albedo have been shown in table 1.3 for urban, industrial area, biomass burning and desert and oceanic dust from Aeronet network measurements (Dubovik et al., 2002). The lowest ω_0 and highest absorption with the strong spectral dependency was observed for dust aerosols in Africa and Zambia. The values of ω_0 differ from an urban industrial area compared to another city (non absorbing particle in Paris and Mexico city with absorbing particle) (Seinfeld and Pandis, 2006).

Table 1.3 Single backscattering albedo from worldwide Aeronet network of ground based radiometer (Dubovik et al., 2002) for different wavelengths at 440, 670, 870 and 1020 nm.

Urban industrial	Mexico city (1999- 2000)	Crete- Paris, France(1999)
ω_0 (440/670/870/1020)	0.90/0.88/0.85/0.83±0.02	0.94/0.93/0.92/0.91±0.03
Biomass burning	Amazonia forest,Brazil-1993-1994, Bolivia(1998-1999)	Africa, Zambia1995-2000
ω_0 (440/670/870/1020)	0.94/0.93/0.91/0.90±0.02	0.88/0.84/0.80/0.78±0.03
Desert dust and oceanic	Bahrain- Persian Gulf (1998-2000)	Saudi Arabia 1998-2000
ω_0 (440/670/870/1020)	0.92/0.95/0.96/0.97±0.02	0.92/0.96/0.97/0.97±0.03

Single scattering albedo depends on the size and refractive index of the particles which in turn depends on the particle hygroscopic properties. Table 1.4 taken from Wang and Gordon (1995) illustrates this behavior. The models are from the work of Shettle and Fenn (1979) and depends on relative humidity. The tropospheric and urban particle has the same diameter approximately but for oceanic is different. Urban aerosol contains absorbing component which corresponds to a high value of the imaginary part of the refractive index. The humidity effect increases the size and decreases complex refractive index resulting in an increase of the single scattering albedo.

Table 1.4 Modal diameter D_i, standard deviation S_i, complex index of refraction m_i, and single scattering albedo ω_i for the three component aerosol models (from Wang and Gordon (1995)).

Component	RH	Di	S_i,	m_i	ω_i
Oceanic	70	0.408	0.40	$1.402\text{-}4.10^{-6}i$	0.9999
	80	0.761	0.40	$1.340\text{-}1.10^{-6}i$	1.0000
	90	1.205	0.40	$1.332\text{-}6.10^{-7}i$	1.0000
Tropospheric	70	0.057	0.35	$1.492\text{-}0.0093i$	0.9346
	80	0.078	0.35	$1.393\text{-}0.0037i$	0.9698
	90	0.095	0.35	$1.364\text{-}0.0020i$	0.9829
Urban	70	0.058	0.35	$1.479\text{-}0.0600i$	0.6793
	80	0.084	0.35	$1.379\text{-}0.0202i$	0.8510
	90	0.120	0.35	$1.346\text{-}0.0069i$	0.9435

1.3.3 Aerosol complex refractive index

The single scattering albedo is not independent from indices of refractive index. For the biomass burning the higher value of ω_0 is related to small value of imaginary part of refractive index according to Mie formalism. For urban industrial area, higher value of ω_0 is related to low value of real part of refractive index. The measurements of the aerosol chemical composition, number and/or mass size distribution and optical properties is required to retrieve key parameters such as the spectral dependency of the aerosol complex refractive index. The aerosol refractive index is often provided from bulk chemical compositions and known values of the refractive indices of pure compounds (Chazette and Liousse, 2001). The aerosol refractive index is highly dependent on the aerosol chemical composition. The particle refractive index is related to the surrounding medium (m), it can be written by:

$$N = n + ik \qquad [1.5]$$

The real part n and the imaginary part k of the refractive index respectively represent the non-absorbing and absorbing components, and are both wavelength-dependent. Refractive index N is usually normalized by the refractive index of the medium (the air in our case), N_0, and denoted by m. Table 1.5 shows that the aerosol refractive index depends on the chemical composition and the source of pollution. The real part of refractive index does not show the spectral dependence. For dust and oceanic aerosol there is high spectral dependency of imaginary part. For biomass burning real part is ranged between 1.47 and 1.52.

Table 1.5. Aerosol refractive index from Aeronet network (Dubovik et al., 2002)

Urban- industrial	Mexico city (1993- 2000)	Crete- Paris, France (1999)
n, k	1.47-0.03 τ(440)±0.014; 0.03±0.03	1.40±0.03; 0.009±0.04
Biomass burning	Amazonia forest, Brazil1993-1994, Bolivia(1998-1999)	Africa, Zambia
n, k	1.47-0.03τ(440)±0.01; 0.00093±0.03	1.51±0.01; 0.021±0.03
Desert dust and oceanic	Bahrain- Persian Gulf 1998-2000	Saudi Arabia 1998-000
n, k	1.55±0.03	1.56±0.03

Table 1.6 shows the aerosol refractive index and single scattering albedo for various wavelengths. The values are related to particle pollutant between street and the planetary boundary layer which are related to human activity. Raut and Chazette (2007) show that the aerosol complex refractive index depends on the absorbing and non absorbing particle in the medium. The complex refractive index ranges between 1.56 -0.03i at 355 nm and 1.59 -0.04i at 532 nm for particle containing soot components, thus leading to single- scattering albedo values between 0.80 and 0.88 respectively.

Table 1.6 Mean complex refractive index determined on the ground with Aeronet station in Paris. The uncertainties are specified in the parenthesis (Raut and Chazette, 2007)

Wavelength	Real part of index	Imaginary part of index	Single scattering albedo
355nm	1.561(0.017)	0.028(0.009)	0.879(0.036)
532nm	1.587(0.009)	0.044(0.004)	0.797(0.015)
441nm Aeronet	1.424(0.04)	0.041(0.012)	0.774(0.030)
673nm Aeronet	1.397(0.04)	0.036(0.010)	0.739(0.030)

1.3.4 Phase function

Atmospheric particles (aerosols) scatter light in different directions. Phase function is the angular distribution of light intensity scattered by a particle at a given wavelength at a particular angle θ, relative to the incident beam and normalized by the integral of the scattered intensity at the angles. In the visible range of the spectrum, the Rayleigh scattering regime is suitable for particle with a diameter much smaller than the wavelength of the incident light (say a diameter below 100 nm). The Rayleigh scattering is more or less independent of the particle shape. The scattered light by a spherical shape particle is proportional to $1/\lambda^4$ and the absorption is proportional to $1/\lambda$. Thus, the scattering is more efficient at the short wavelengths (UV, blue) than at long wavelengths (red). A consequence of this phenomenon is the reddening of white light on passing through a population of very small particles. If θ is the angle between the incident beam and the scattered beam, the Rayleigh scattering phase function can be described as a function of the size parameter of $\frac{\pi D_p}{\lambda}$ and particular angle θ:

$$P(\theta) = \frac{\lambda^2}{8\pi^2}\left(\frac{\pi D_p}{\lambda}\right)^6 \left|\frac{m^2-1}{m^2+1}\right| (1+\cos^2\theta) F_0 \qquad [1.6]$$

$P(\theta)$ depends on θ by the function $(1+\cos^2\theta)$ from what we may show that the light pattern is symmetrical in the forward and backward directions. The normalized complex refractive index is m. When the particles are smaller than the wavelength of light, then the light is scattered into the sideways direction. When they become larger than the wavelength, more is scattered into forward direction. If the particle is about the same size of wavelength we use the formal scattering solution based on the Mie theory for a spherical particle. It has been observed that mass scattering varies with systematic variation of real and imaginary part of refractive index of the medium according to Mie scattering theory and equations.

Figure 1.2 shows the angular dependencies of phase function sensitivity of fine and coarse mode aerosol to the real part of the refractive index simulated for a monomodal lognormal size distribution and 2 different modal radius. The angular dependency is clearly different

when considering submicronic or supermicronic particles, especially for large scattering angle more than 135°. The sphericity of the particles has also a large impact in the backscattering direction (from Dubovik et al. (2006)).

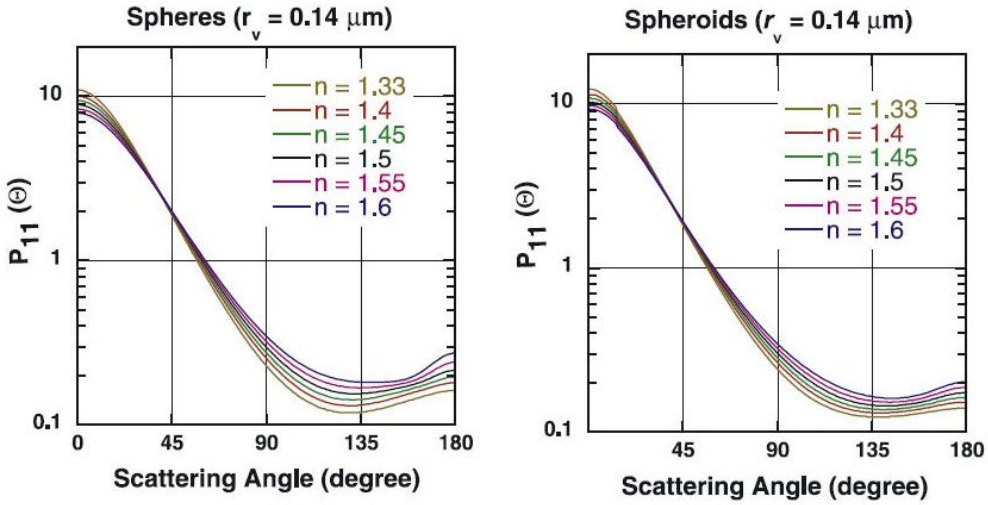

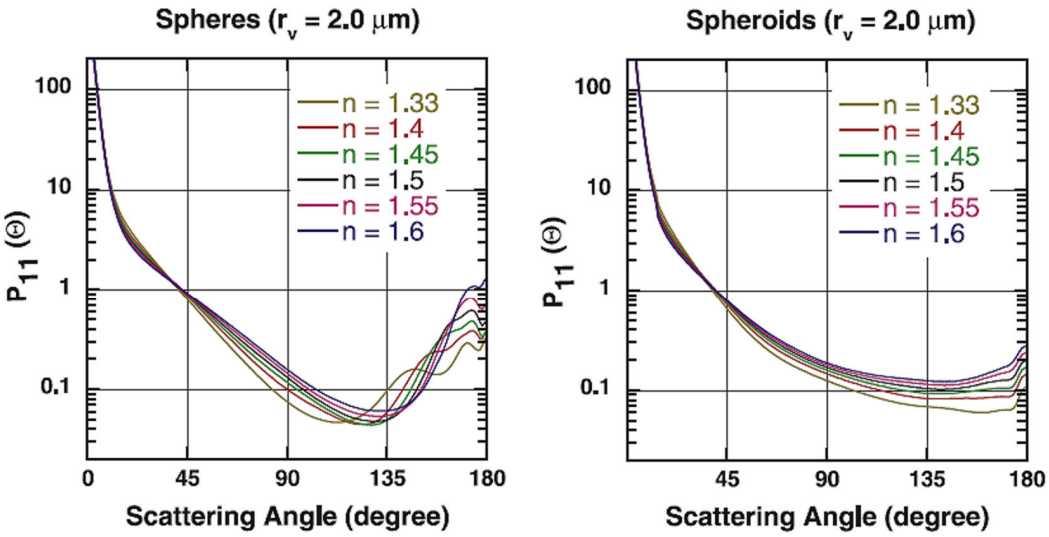

Figure 1.2 The angular dependencies of phase function sensitivity of fine and coarse mode aerosol to the real part of the refractive index simulated for a monomodal lognormal size distribution with a mean modal raidus of 0.14 μm (top row) and 2.0 μm (bottom row) considering sphere (left column) or spheroids (right column), after Dubovik et al. (2006).

1.3.5 Aerosol optical thickness and Angström exponent

The solar radiation passes through the Earth's atmosphere and is attenuated due to the extinction by the aerosol particles and gaseous molecules of the atmosphere. The total optical thickness τ is due to attenuation of molecular (Rayleigh), trace gas (such as Ozone) and of course aerosol. The measurement of relative flux of solar radiation at the Earth's surface as a function of solar zenith angle provides the optical thickness (or depth) (Seinfeld and Pandis, 2006).

The spectral variation of aerosol optical depth $\tau_a(\lambda)$, which is produced through attenuation by aerosol is primarily determined by the aerosol size distribution. Assuming the atmospheric particulates are equivalent to spheres and their refractive index is known, the following Fredholm integral equation which relates the optical depth to an aerosol size distribution is given by:

$$\tau(\lambda) = \int_0^\infty \int_0^\infty \pi r^2 Q_{ext}(r, \lambda, m)\ n(r, z)\ dr\, dz \qquad [1.7]$$

where n(r,z) is the height-dependent aerosol number density in the radius range r to r+dr , m is the complex refractive index of the aerosol particles, λ is the wavelength of the incident radiation, and $Q_{ext}(r,\lambda,m)$ is the local extinction efficiency of the atmosphere (King, 1978).

Table 1.7 shows the aerosol optical thickness for urban and industrial, desert and oceanic area and biomass burning. Urban area AOT (at 440 nm) ranges between 0.1 and 1 and the biomass burning has the highest value of AOT 2.1 and 3 whereas the desert dust and oceanic particle at Saudi Arabia and Bahrain shows the range of 0.1 and 1.2.

Table 1.7 Aerosol optical thickness of different source of aerosol by Aeronet network (Dubovik et al., 2002).

Urban industrial	GSFC, Greenbelt, MD (1993- 2000)	Crete- Paris, France (1999)
Range of AOT	$0.1<\tau(440)<1$	$0.1<\tau(440)<1$
Biomass burning	Amazonia forest, Brazil 1993-1994, Bolivia(1998-1999)	South America 1993-1995
Range of AOT	$0.1<\tau(440)<3$	$0.1<\tau(440)<2.1$
Desert dust and oceanic	Bahrain- Persian Gulf 1998-2000	Saudi Arabia 1998-2000
Range of AOT	$0.1<\tau(440)<1.2$	$0.1<\tau(440)<0.9$

The AOT depends on the wavelength. The AOT spectral behavior is characteristic of the particles size. The variation of extinction coefficient with wavelength can be presented as a power low function with a constant (related to power factor) as the Angström coefficient. Long residence time of air mass over land and in particular the passage over large urban areas may cause high concentrations of fine particles and thus high value of Angström coefficient. The Angström formula relates the spectral dependence of the optical thickness and the atmospheric haziness:

$$\tau_1 = \beta \lambda_1^{-\alpha} \qquad [1.8]$$

$$\tau_2 = \beta \lambda_2^{-\alpha}$$

$$\alpha = \ln(\tau_1 / \tau_2) / \ln(\lambda_1 / \lambda_2)$$

where β is a given coefficient, τ_1 and τ_2 are measured values of aerosol optical thickness at two reference wavelengths λ_1 and λ_2, and α is the Angström exponent respectively. α and β

are independent of wavelength. They can be used to describe the size distribution of aerosol particles and the general haziness of the atmosphere. A typical range for α is 0.5 – 2.5 with an average for natural atmosphere around 1.3±0.5. The range of Angström parameters is 1.2~ 2.5 in urban area, 1.2 to 2.1 for biomass burning and 0 to 1.6 for desert dust and oceanic (Dubovik et al., 2002).

1.4 Transport and dispersion of pollutants in the troposphere

The term "transport" designates the movement of pollution from its source to a receptor. The sun radiation and its effects at Earth surface, Earth rotation, topography, meteorology and the nature of the surface affect transport and mixing of pollutants in the atmosphere. The exact path of pollutants is generally difficult to predict, even near the sources. During the transport of pollution, the composition of the air mass is also changing according to the lifetime of pollutants associated to the deposition and the chemistry and many entries coming from other sources.

1.4.1 Impact of meteorology and dynamics of atmosphere on aerosol transport and dispersion

Meteorology has a close relationship with air quality and participates to the concentration levels of locally emitted primary pollutants, formation of secondary pollutants, and their transport to other areas, and their removal from the atmosphere. Meteorology is a key factor in determining the magnitude, location and the evolution of a pollution event that will be caused by anthropogenic emissions. The dispersion of pollutants depends on the atmospheric turbulence with both mechanical and thermal origins. For instance, the effective emission height and the dispersion of pollutants from a chimney depend on the plume density, the wind speed and the atmospheric temperature profile.

More generally, the behaviour of pollutants in the atmosphere is determined by atmospheric stability. The atmospheric temperature may indeed increase or decrease with altitude in the first layers and mixing rate of pollutants is highly dependent on the vertical profile of the atmospheric temperature. The temperature of an air parcel which raises adiabatically typically decreases with a temperature gradient of 5 to 10° C/km according to its water vapor content. If the atmospheric temperature decreases more quickly with height

than the temperature of the air parcel, then the atmosphere is unstable with strong vertical ascents in both upward and downward directions. On the contrary, if the atmospheric temperature decreases more slowly or even increases with height than the temperature of the air parcel, the atmosphere is stable. If the temperature of an atmospheric layer actually increases with altitude, it is called an inversion layer. An inversion occurs when warm air lies above cool air and this condition is extremely stable.

Air vertical motion may result from convection from solar heating of the Earth's surface, convergence or divergence of horizontal flows, flow over topographic features at the Earth's surface, and float tendency caused by the release of latent heat as water condenses. The surface heating is the driving phenomenon for the stability of the atmospheric layer connected to the ground. Academically, summer day produces the best meteorological conditions for dispersion and a cold winter morning with a strong inversion results in the worst condition of dispersion, but the local meteorological phenomena have also to be taken into account.

1.4.2 Meteorological scales

Air motion is related to meteorological phenomena with various spatial scales extending from a few meters (around a building or a small hill) to thousands of kilometers (a major storm). Our study will be limited to microscale and mesoscale phenomena sufficient for studying the atmosphere behavior in its lowest part. Microscale phenomena occur on spatial scale less than 2 km and typical timescale of 1h like turbulence or thermals. Mesoscale phenomena extend from 2 km to 200 km over hour to a few hours or days. They influence on transport and dispersion of pollutants to areas that are hundreds of kilometers from their sources as land or sea breeze and high or low pressure systems and their associated fronts. Most of anthropogenic and natural pollutants are indeed emitted in the planetary boundary layer. They may be dispersed and diluted rapidly, resulting in low concentrations; in other periods, they may be trapped in a relatively small volume leading to an air pollution episode. The level of local pollution is thus strongly dependent on various meteorological phenomena from microscale and mesoscale.

In order to illustrate this complexity, Figure 1.3 shows the schematic of the atmospheric boundary layer structure over an urban area. Urban boundary layer has different

sub-layers ranging in microscale. The lowest distinct layer, Urban Canopy Layer, ranges from ground up to average height of roughness elements (building). It is part of roughness sub layer. Above the roughness layer there is an inertial sub layer. The urban outer layer is probably to a large extent determined through advective processes. The outer part of boundary layer displays the characteristic of a convective mixed layer (Boubel et al., 1994 ; Seinfeld and Pandis, 2006).

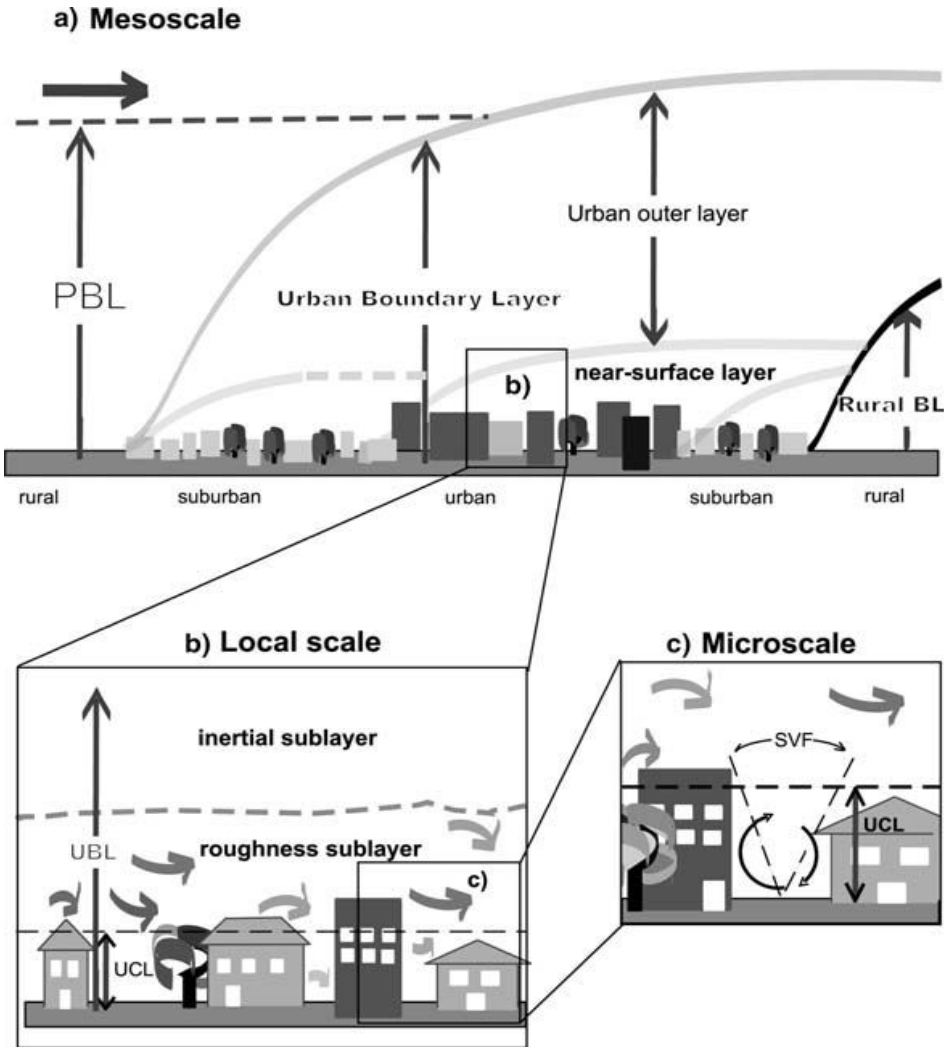

Figure 1.3 Sketch of the urban boundary layer structure indicating the various sub layers and their names (Rotach et al., 2005).

As dynamics and chemistry are unavoidably linked, it is interesting to associate meteorological scales with the scales of chemical phenomenon as done in Table 1.8. The air pollution problem may be classified to local, urban, regional, continental and global. The local scale includes about 5 kilometres and urban in the order of 50 kilometres whereas the regional scale is from 50 to 500 km. Continental scale is extended to several thousands of kilometres. Considering local wind in the urban area, the local pollutant like CO and NO_x will be dispersed at local scale due to movement of thermals and turbulence. The land and sea breeze are responsible for dispersion of pollutant like SO_2, NO_x and Ozone in regional scales. Greenhouse gases and aerosol climate changes is due to mid latitude cycles in the continental scale.

Table 1.8 Spatial scale of air pollution and meteorological phenomena

Scales	Pollutants	Meteorological Length scale, km	Meteorological phenomena
Urban and local Microscales	CO, NOx, motor vehicle pollutant	1-10	Thermals, turbulence
Regional Mesoscales	Ozone, nitrates, sulfates, acid rain	10- 100 100-2000	Land ,sea breeze H and L pressure system
Global scales	greenhouse gases aerosol- climate oxidation	1000-40,000 100-40,000 1-40,000	mid-latitude cyclones motion of whole weather hurricanes front

The importance of the meteorology for air quality in a given area is clear from the measurement of PM. The particle mass concentration varies by the time in different echelon. Both local and regional anthropogenic emissions of the major pollutants (SO_2, NO_2, NO…) vary by a factor of less than 2 from month to month, however the hourly variability can be an order of magnitude higher. This variability of pollutant concentrations and the resulting clean and polluted days in an area with more or less constant emissions are determined by meteorology (Oke, 1978; Rotach et al., 2004). Local wind systems are usually significant in terms of transport and dispersion of aerosol pollutant in horizontal and vertical scales. For example land-sea breeze and mountain-valley winds have impact on local aerosol load.

1.4.3 Dynamical and meteorological processes in the continental atmospheric boundary layer

The planetary boundary layer with height between 1 and 3 km controls the flow of heat, exchange of mass, water vapor and momentum between the surface and the free atmosphere. Aerosol and moisture tend to be trapped within the planetary boundary layer (PBL) and can be used as tracers for study of the boundary-layer vertical structure and time variability. Turbulent motions which transport atmospheric properties both horizontally and vertically are dominant flow with the time scale of 1 hour. The mean properties of the flow in this layer- the wind speed, temperature, and humidity- experience their sharpest gradients in the first 50-100 m, appropriately called the surface layer.

In surface layer the turbulence fluxes changes by less than 10% of their magnitude. In this layer the flow is insensitive to the earth's rotation and the wind structure is determined primarily by surface friction and the vertical gradient of temperature. The inversion acts as a limit for vertical motions.

In the mixed layer the shearing stress is variable and the wind structure is influenced by surface friction, temperature gradient, and the earth's rotation. The sharp gradients in the mean wind speed, wind direction, and temperature occur in the first 10% or so of the convective boundary layer (CBL); in the upper 90% of the CBL strong convective mixing smoothes out almost all vertical variations in the mean profiles.

In day time the temperature decrease rapidly with height in the lower layer and parcels accelerate vertically away from their original positions; and are convectively mixed. With the time of sun set one or more shallow layers may form due to variation of temperature gradient.

In clear sky at night with low winds condition, the ground and low level of atmosphere become cooler than air above it. This is known as radiation inversion which happened in surface layer. The night time stable boundary layer is where the temperature drops less rapidly with height and parcels staying to their original positions. The plumes lose their energy source near the surface where the ground is cooling quickly from radiative heat loss to space. The air immediately above the surface cools and mixes progressively upward through the action of turbulence generated by wind shear. The inversion that begins to form at the surface grows steadily to a depth of 100-200 m by midnight. The upper limits for these two

states define the depths of the daytime (the base of the inversion layer) and nighttime boundary layers.

Figure 1.4 shows the major parts of boundary layer: a very turbulent mixed layer; residual layer containing former mixed-layer air; and a nocturnal stable boundary layer.

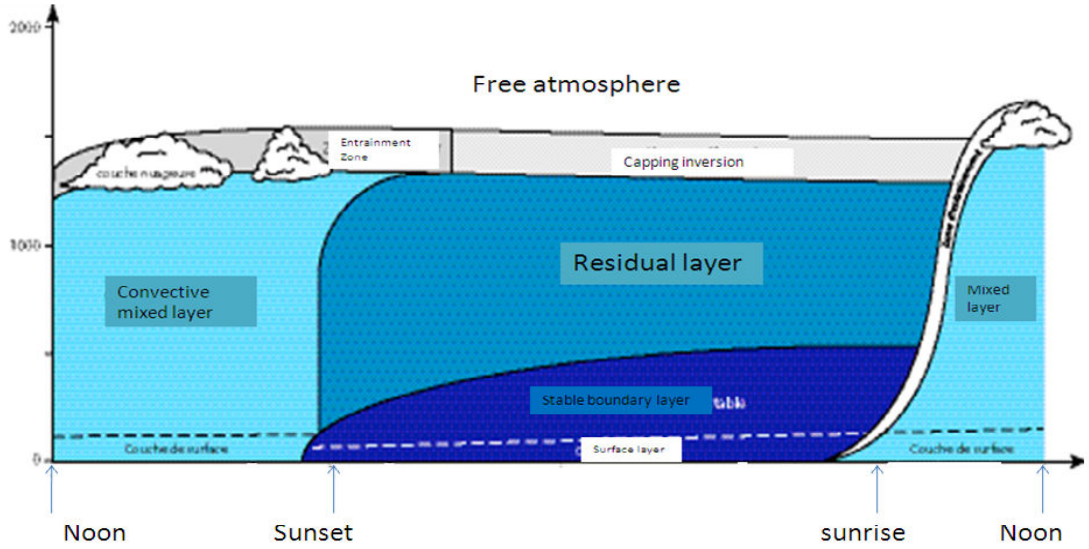

Figure 1.4 Evolution of the convective and stable boundary layers in response to surface heating and cooling (Stull, 1988).

Figure 1.5 also shows that the entrainment process by which air from above the inversion base is drawn into the CBL in the regions of down trending motion. Energetic thermals affect above inversion but mostly they make the upper interface of the CBL to appear highly mixed up. Horizontal roll vortices and dust devils also appear when conditions favor their development, adding to the modes available for convective mixing in the CBL.

Efficient mixing process occurs in the boundary layer, transporting air masses up and down ward. Vertical uplifting of polluted air masses from the boundary layer to the free troposphere occurs through deep convection, orographic lifting and uplifting associated with cyclones.

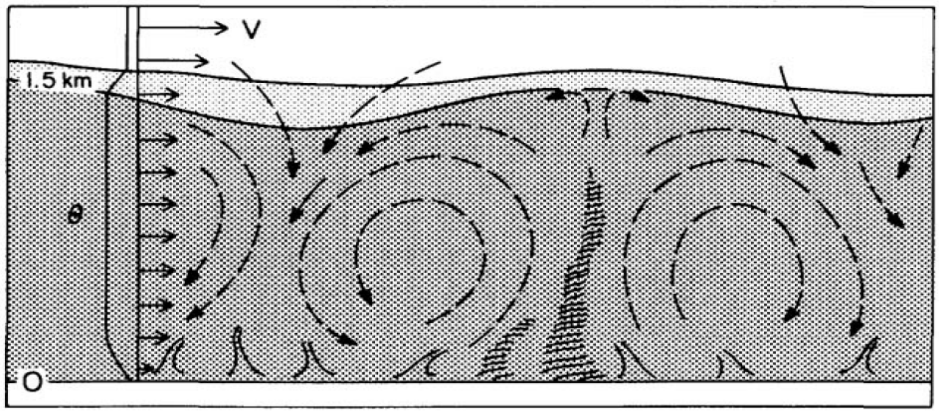

Figure 1.5 Schematic of convective boundary layer circulation and entrainment of air through the capping inversion (Stull, 1988).

The scattering and absorption of aerosols diminish the surface radiation and keep from sensible heat flux and evaporation and inducing feedbacks such as the enhanced stratification and change in relative humidity in the surface layer. The reduced sensible heat due to aerosol backscattering lowers the air temperature and suppresses the growth of the ABL (Yu et al., 2002). Aerosol absorption decreases the turbulent heating but simultaneously increases the solar heating, increasing the air temperature and decreasing the strength of capping inversion. The resultant rise of the top of the ABL compensates the lowering due to the reduced buoyancy flux. With strong aerosol absorption, the increased entrainment heating enhances the ABL warming. Absorbing aerosols within the ABL decrease the probability of formation of boundary layer clouds, causing additional warming through cloud-feedbacks. The results are sensitive to the vertical distribution of absorbing aerosols. Absorbing aerosol above the ABL increases the strength of capping inversion and reduces the top of the ABL, hence decreasing the entrainment drying and moistening the ABL (Wyngaard, 1990).

Export of pollution from the atmospheric boundary layer to the free troposphere can occur whenever an air parcel is transported above the boundary layer height. Since over land the atmospheric boundary layer has a distinct diurnal cycle with a maximum during a day and a minimum during the night, a residual layer is formed upon the transition from day to night.

Transport of pollutants from the free troposphere to the boundary layer is not well observed because descent into the atmospheric boundary layer often does involve not large

concentrated plumes, but background air. In addition, venting through the top of the atmospheric boundary layer often involves small scale processes not directly from global scale.

1.4.4 Sea breeze characteristic and impact on aerosol transport

Lakes and oceans lessen the temperature of water –surface due to their high heat capacity during diurnal cycle. The land surface, however, warms and cools more dramatically because the small molecular conductivity and heat capacity in soils prevents the diurnal temperature signal from propagating rapidly cooler away from the surface as a result; the land is warmer than the water during the day and cooler at night.

During mid morning (10:00 local time) after the elimination of the nocturnal surface boundary layer, air begins to raise over the warm land near the shore line and cooler air from the water flows into land. This is known as the sea breeze (lake breeze**).** The inland limit of cool air progression over land is known as the sea breeze front**,** and is marked by low level convergence (in a band about 1 to 2 km wide), a marked temperature drop (often several °C); hence, it is a mesoscale cold front; an increase in humidity, upward motion (of about 0.5 to 2.5 m/s), and sometimes enhanced cumulus clouds. During the day, the temperature and consequently pressure difference increase in lower layer and cause flow of breeze in low layer. At night this pressure difference disappears and is sometimes reversed, causing a land breeze.

The onset of the sea breeze is sometimes in the form of a sudden squall, resembling a minor cold front, which is called the sea breeze front. In the tropical countries with steady gradient pressure, we can expect the sea breeze every day at the same time, reaching strength of 6 or 7 ms^{-1}. In hot countries arrival of the sea breeze is very welcome as a gust of cooling wind in the hottest part of day. The depth of the sea breeze has been observed to be on the order of 100 to 500 m and the total circulation depth including the return circulation can range from 500 m to 2000 m. Figure 1.6 shows an idealized sea breeze circulation. The air mass over sea which is cold progresses in warm land and consequently a convective layer is formed (thermal internal boundary layer; TIBL). Vertical exchange of pollutants happens more on breeze nose between 300 to 2500 m (Barbato, 1975). Breeze nose has an average height of 700 m. Nose of sea breeze may have a depth of two times more than trailing flow.

When there is not a background synoptic flow, sea breeze progresses in land normal to coast with a speed of 1 to 5 m/s. If the background synoptic flow is in the same direction as sea breeze, sea breeze can progress more than 100 km inland. The return circulation at 1 to 2 m/s aloft brings warmer air back out to sea where it descends toward the sea surface to close the circulation (Stull, 1988).

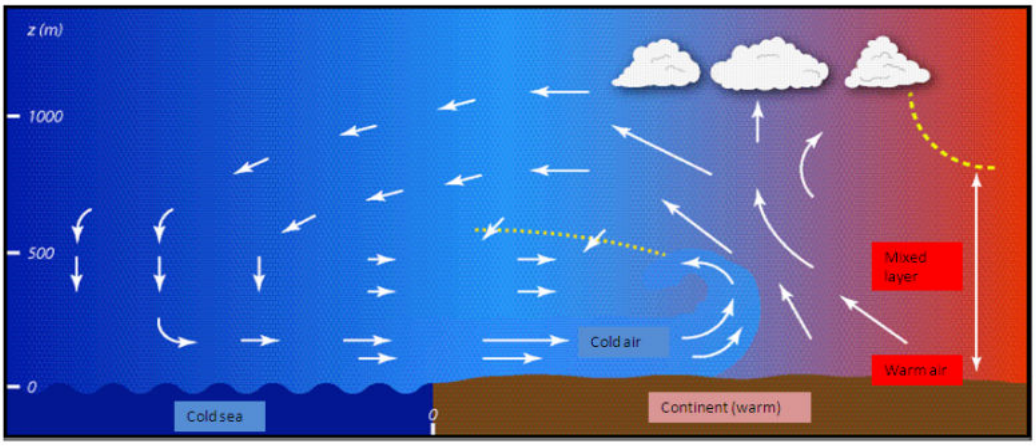

Figure 1.6 Idealized sea or lake breeze circulation (Stull, 1988)

Some recirculation of sea breeze polluted material exists not very far behind the sea breeze front; however, the really serious problems of pollution carried by the sea breeze are related to the land- and sea-breeze reversal. The sea-breeze carries pollutants far inland during day and land breeze carries them back to the sea with wind reversal. This gives a mechanism for a complete layer of polluted air to be maintained at high concentration and returned to the same locality 24 hours later (Simpson, 1994).

From June to October, the land/sea breeze is a mesoscale process occurring almost daily but confined within the boundary layer (Stull, 1988). Rimetz-Planchon et al. (2008) investigate PM10 pollution episodes associated with meteorological situations in an urban and industrialized coastal site of the southern part of the North Sea. These pollution episodes predominantly occur during sea breeze days, but also as a result of occasional industrial releases. The high PM10 concentrations appear under high-pressure conditions. The highest polluted days are characterized by the highest temperatures and hardly any rain.

Sea breeze has important role in aerosol transport in higher altitude and long range distance. Verma et al. (2006) show the mechanisms leading to lofting and large-scale advection of aerosols over Indian ocean due to interaction of the sea breeze winds along the coast on Indian ocean. Lofting of air observed as high as 800 hPa (approximately 2 km above sea level) could lead to entrainment of aerosols into the free troposphere and long-range transport. Upward motion of air was observed everywhere, on average higher in March than in February, because of convergence between the sea breeze and the synoptic-scale flow. Colbeck et al. (2002) shows that wind regime exhibited a distinct influence such that the sea-breeze circulation strongly enhanced the formation of secondary aerosols. During "normal" days, any differences in concentrations were possibly due to local emissions. Elevated concentrations in the fine mode were detected during the sea-breeze days.

1.4.5 Long range transport of aerosol

The transport distance of particles strongly depends on particle size and meteorological conditions. Long range transport (LRT) can remain for long periods (days- weeks) under dry conditions. Typically they undergo from hundreds to thousands of kilometers. The particle concentration may rise to extraordinarily high level due to LRT when air masses arrive during suitable meteorological conditions (no rain and weak mixing of air masses). The local scale episodes (due to winter time inversions, resuspension of road dust, emissions from stationary emission sources) and the regional scale photochemical pollution episodes (common in warm and hot regions such as southern Europe) can occur at the same time. The source identification of particle especially in urban areas is complicated. The most common particle sources of LRT episodes are strongly dependent on season and region but they can be roughly divided into three major types of biomass burning, desert dust storm and emission from heavily polluted area due to anthropogenic activities. The aerosol load over Europe and the contribution of long and medium range sources have been observed from the North American boundary layer and mineral dust from North Africa is transported across the Atlantic Ocean during spring. Schematic of long range transport pollutant from the up- wind "source" continent to the downwind receptor is shown in Figure 1.7. Long range transport occurs through episodic events or through increasing in the global background. Emission from the upwind "source" may be transported into the boundary layer or mixed vertically in the free troposphere for rapid transport. For example, Lin et al (2005) have studied the impact of long range transport on air quality of Taiwan over the winter monsoon period of 2000 and

2001 in three LRT events. They have found that the contribution of LRT on CO and SO_2 are about 230 and 0.5 ppb respectively. They have shown the LRT can increase PM10 and SO_2 up to 100%.

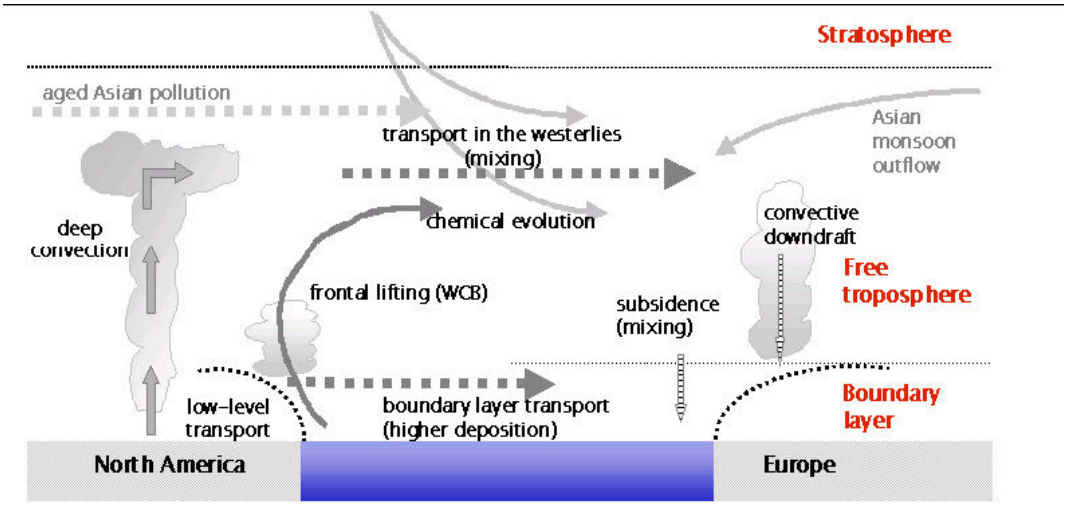

Figure 1.7. Process in long range transport (I. Bey presentation to the ACCENT T&TP startup meeting, 2004)

Trajectories are the paths of very small particles of air as they move through time and space. Particles in space at a given time can be traced forward or backward in time along their trajectory. Backward trajectories indicate the past path of a particle. By locating the plume vertical height, back trajectory analysis using NOAA HYSPLIT (HYbrid Single-Particle Lagrangian Integrated trajectory) algorithm can be used to examine the source regions.

In this chapter we have explained the microphysical and optical properties of aerosol and the structure of the classical boundary layer and local meteorological phenomena as they are important issues for transport and mixing of pollutants. In following chapter the applied methods and instrument and the experiments will be described.

2 Instrumentation and method

2.1 LIDAR vertical soundings

The Lidar (light detection and ranging) technique has became an efficient tool for continuously monitoring, in real time, gases or aerosols which may be used as a tracer for investigating the structure and the dynamics of the atmosphere. The ground-based Lidar systems have been developed and designed as portable, multi-wavelength and femtosecond systems for various applications. The remote sensing of vertical distribution of aerosol particles, produced locally over the measuring site (car traffic, domestic heating, industrial activities), or transported by the atmospheric circulation (air pollution over frontiers) can be carried out by Lidar. Moreover, the small divergence of the laser beam makes Lidar very attractive for studying the ABL and its correlation with ground air pollution levels.

Lidar can be used in investigation of air-quality issues as it records inversion layer and helps for the validation of regional forecasting models, in the horizontal mapping of urban and industrial areas to detect the sources of pollution and analyze the local pollution phenomena (3D tracking). Atmospheric studies of urban pollution and photochemical reaction, vertical concentration profiles of trace species like SO_2, O_3 and NO_2 and sulphur components are some of areas of Lidar research.

Through its high spatial and temporal resolution, Lidar as a long-range system monitors the evolution of some meteorological phenomena (stratification, front passage, turbulence…) and concentration levels of trace gas and distinguish droplets from ice crystal. First, it may be used for studying the concentration of gases (e. g. O_3, NO_2, N_2O and SO_2) and aerosol related to climate change above natural variability (it requires long-term climatology of aerosol including vertical distribution of sources and impact on radiation). Second, air quality and long range transport of pollution between region needs the aerosols on elevated layers which are excellent tracer for of pollution. Third, we quantify the pollution sources and their atmospheric pathway to sensitive downwind receptor. Furthermore Lidar provide us direct observations of plumes from major events such as dust storm which are associated with the characteristic aerosol emissions (large parts of plumes are within elevated layers). Understanding transport of pollutants at elevated layers and down mixing inside the boundary layer is essential for air quality forecast.

2.1.1 Historical evolution of Lidar systems

Incoherent backscattering Lidar systems are key tools to retrieve spatial distribution and optical properties of aerosols and clouds. Lidar actually started with using the CW searchlights to measure stratospheric aerosols and molecular density in the 1930s, well before the first (ruby) laser was invented in 1960. In 1938 the pulses of light by electric spark and flash lamp made the replacement of the bistatic by monostatic setup. Lidar research has been involved in laser development. Many laser-based instruments designed for Lidar had to reach high requirements like laser power, wavelength, pulse width, beam shape. In addition to lasers, advanced systems like optical filter, efficient detector, data acquisition system and computer were needed for advanced Lidar system.

The rapid development of modern Lidar started with the invention of laser on 1960 and Q-Switch technique on 1962. Early year ruby, nitrogen and CO_2 laser were used while ND:YAG and Excimer laser have been used since 1980. Various wavelengths from 250 nm to 11 μm were produced by CO_2 (10.6 μm), Dye, ND:YAG and Eximer laser for different applications. Generation of ultra short laser pulses was made possible by development of chirped pulse amplification (CPA) techniques in 1985. This technique allows producing femtosecond pulses with the peak power up to 10^{12} W (TW) giving enormous short-time intensities. Using this latter techniques, Wöste et al. (1997) recently demonstrated that white-light pulses may be produced by a femtosecond TW laser and allow range-resolved broadband absorption measurements, which opens the way to a real multi-components Lidar for the simultaneous detection of several trace gases. Presently new laser types such as microchip or solid state Raman laser are also under investigation.

Lidar instrument now allows observation of atmospheric constituents from the ground, aircraft or satellite. The evolution of Lidar system from ground-based measurement to long-duration space borne experiments started in 1964. The first airborne Lidar flight on a small aircraft was made on 1969. Four years later, the long range measurement was carried on a large aircraft (McCormick, 2005). Finally, Lidar in space technology has started with the LITE experiment (Winker et al., 1996) followed by the Geosciences laser altimeter system GLAS (Schutz et al., 2005) in 2003 and the Cloud-Aerosol Lidar and Infrared Pathfinder Satellite Observations CALIPSO in 2006 (Winker et al., 2003). Spaceborne Lidar on low

Earth orbit flight can provide measurements of sea ice roughness and thickness, cloud and atmospheric properties, land topography, vegetation canopy heights, ocean surface topography, surface reflectivity.

2.1.2 Basic physical processes and Lidar techniques

In this work, we will use elastic Lidar (so-called Rayleigh-Mie Lidar). Elastic scattering in Lidar refers to the Rayleigh scattering from molecules and Mie scattering in which particles return to their original states and there is no frequency shift in the scattered light except Doppler effects. The specific application of an elastic backscatter Lidar is measurement of visibility, detection of aerosol and cloud.

There are several other Lidar techniques based on basic physical processes due to light-matter interactions that can use for aerosol research, namely Raman Lidar, DIAL Lidar or Doppler Lidar. Inelastic scattering in Lidar refers to the Raman scattering from molecules or small particles, in which the particles change their initial states to different final states and the scattered light experiences frequency shift due to vibration-rotation Raman shift or pure rotation Raman shift. This shift is characteristic for scattering molecule. Raman Lidar systems detect, in addition to backscattering at laser wavelength (elastic backscattering) also signals at different wavelengths.

Raman Lidar technique is applied to determine the profile of the particle extinction coefficient directly. Raman Lidar has been applied for measurement of atmospheric temperature and detection of a variety of atmospheric species, like for instance the water vapor profiles (Whiteman et al., 1992). Veselovskii et al. (2002). show that Raman lidar signal can be combined to elastic backscatter signals to provide more information on aerosol microphysics

Differential absorption in Lidar refers to using two wavelengths, one on resonance with an absorption line, while another off resonance. The difference in the absorption cross-sections at these two wavelengths results in the signals difference between two channels. This is very useful in determining concentration of molecular species. Differential absorption Lidar DIAL makes use of single absorption lines or broad absorption bands of gases. It is used for measurement of different gases in the atmosphere.

Resonance fluorescence in Lidar usually refers to the fluorescence from the metal atoms in the Middle and upper atmosphere. Of course, some molecules in upper atmosphere also can give resonance fluorescence, e.g., N2+. The process contains two steps: the first is for ground-state atoms to absorb incident laser photons and the second is for the excited atoms to spontaneously emit fluorescence photons. This is a first-order process, so has much higher cross-section than non resonance scattering process.

All atoms and molecules in the atmosphere experience Doppler effects. The Doppler frequency shift depends on the radial velocity along the laser beam and the Doppler frequency broadening due to the thermal velocity distribution of atoms and molecules in thermal equilibrium. Small particles, like aerosols, will also have Doppler effects, but due to their very slow velocity, their Doppler effects are usually small enough to be negligible. Doppler Lidar is another ground based Lidar for measurement of turbulence and wind.

2.1.3 Rayleigh-Mie Lidar signal theory

Using Lidar equation, we relate the received photon counts (or light power) with the transmitted laser photon counts (or laser power), probability of scattered photon, medium transmission and system efficiencies, etc. Lidar equation for backscatter elastic signal by air and molecule is written by formula [2.1]

$$P(R) = \frac{E_0}{R^2} G(R)\ \eta_l \beta(R) \exp[-2\int_0^R \alpha(r)dr] \qquad [2.1]$$

P(R) is the received signal from distance R due to Rayleigh and Mie backscatter by molecules and aerosols, E_0 is the transmitted laser pulse energy, η_l describing the efficiency of the optical and detection units, and G(R) is the geometrical form factor, mainly concerning the overlap of laser irradiation with the field of view of the receiver optics. $\beta(R)$ ($km^{-1}sr^{-1}$) and $\alpha(R)$ (km^{-1}) are backscattering and extinction coefficients, respectively. The exponential term describes the attenuation of light by scattering and absorption on its way through the atmosphere. According to the Lambert–Beer–Bouguer law, it depends on the volume extinction coefficient $\alpha(r)$ and the length of the light path, which is in case of Lidar twice the distance between the instrument and the backscattering volume.

At first, we have corrected the Lidar signal from the background noise. At day time the background noise is dominated by direct or scattered Sun light whereas at night time by the moon and stars. Detector noise is another source of undesired signal. The background noise is estimated by taking the average of the backscatter signal between 22 and 30 km, and is subtracted from the Lidar signal. The Lidar signal which is corrected from background noise in the far range and overlap function is used as general term in our calculations.

$$S(R) = \mathrm{R}^2\,\mathrm{P}(\mathrm{R})/\mathrm{G}(\mathrm{R}) \qquad [2.2]$$

Secondly, we need to separate the scattering from the extinction. Since scattering and extinction of molecules and particles are independent of each other, the corresponding coefficients can be split in a molecular and particle term. Formula [2.1] can be developed as following considering the backscattering and extinction of aerosol (β_{aer} and α_{aer}) and molecules (β_{mol} and α_{mol}):

$$S(R) = E_0 \eta_L [\beta_{aer}(R) + \beta_{mol}(R)] \exp[-2\int_0^R [\alpha_{aer}(r) + \alpha_{mol}(r)]dr] \qquad [2.3]$$

Molecular absorption is removed from signal before using in the method. $\beta_{mol}(R)$ and $\alpha_{mol}(R)$ are obtained from the available approximated meteorological data of temperature and pressure and in standard conditions. For standard condition P_s =1013.25 and T_s = 288.15 K represent reference pressure and temperature at which β_s was calculated. P and T are any pressure and temperature.

$$\beta_{mol}(\lambda, r) = \frac{N(r)}{N_s}\beta_s = \frac{P(r)}{P_s}\frac{T_s}{T(r)}\beta_s \qquad [2.4]$$

When we have the standard condition then:

$$\beta_s(\lambda) = \frac{N_s\,\sigma(\lambda)}{L_{mol}} \qquad [2.5]$$

where L_{mol} is the molecular Lidar ratio (or molecular extinction-to-backscatter ratio).

$$L_{mol} = \frac{\alpha_{mol}}{\beta_{mol}} = \frac{8\pi}{3} \qquad [2.6]$$

In that N_s is the molecular number density and σ is Rayleigh cross section. The total Rayleigh scattering cross section is given by formula [2.7] where λ is the wavelength, n_s is the refractive index for standard air at λ and N_s is the molecular number density for standard air and ρ_n a term for anisotropy of airaltitude is also depends on the wavelength (Bucholtz, 1995).

$$\sigma_{(\lambda)} = \frac{24\pi^3 (n_s{}^2 - 1)^2}{\lambda^4 N_s{}^2 (n_s{}^2 - 2)^2} \left(\frac{6 + 3\rho_n}{6 - 7\rho_n}\right) \qquad [2.7]$$

The best fit equation for the scattering cross section as a function of the wavelength is defined by Bodhaine et al. (1999).

$$\sigma(x10^{-28} cm^2) = \frac{1.0455996 - 341.29061\lambda^{-2} - 0.90230850\lambda^2}{1 + 0.0027059889\lambda^{-2} - 85.968563\lambda^2} \qquad [2.8]$$

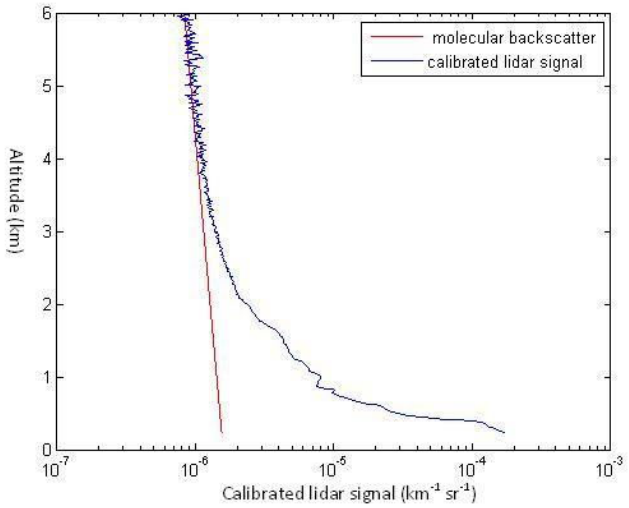

Figure 2.1 Example of a Range-corrected Lidar signal S(R)-black color, molecular backscatter in red color.

The range-corrected signal S(R) represents the Lidar signal corrected from its quadratic dependence. The reference altitude is the altitude in that the aerosol backscattering is negligible in comparison to molecular backscatter. Figure 2.1 shows the range-corrected Lidar signal obtained by CIMEL Lidar and the corresponding molecular backscatter profile. The Lidar profile is calibrated by overlap function and is averaged to increase the signal to noise ratio.

2.1.4 Ultraviolet-visible backscatter Lidar system

Short wave and long wave have been used to study different feature of atmosphere (e.g. gas concentration, air quality, water vapor and meteorology parameters (wind speed and direction, relative humidity…). UV-VIS measurements are of particular interest from a public health standpoint as they are linked to the evolution of the Ozone layer and aerosols. In this study, we will use mainly the 532 and 355 nm wavelengths to study optical characteristics of aerosol and their vertical distribution. In the following section, we present the Cimel and Leosphere EZ aerosol ground-based Lidar as they are working on UV-VIS wavelength. A backscatter Lidar system consists of a transmitter, a receiver and a detector. The use of a Nd:YAG laser with primary emission at 1064 nm, double (532 nm) and triple (354,7 nm) is one of the standard solutions. The required wavelength stability, bandwidth and spectral purity are usually met by standard commercial lasers. The transmitter system consists of

beam expanding optics to decrease the beam divergence and the power density of the transmitted beam. Figure 2.2 shows a schematic of a Lidar system consist of transmitter, receiver, system control and data acquisition and data analysis.

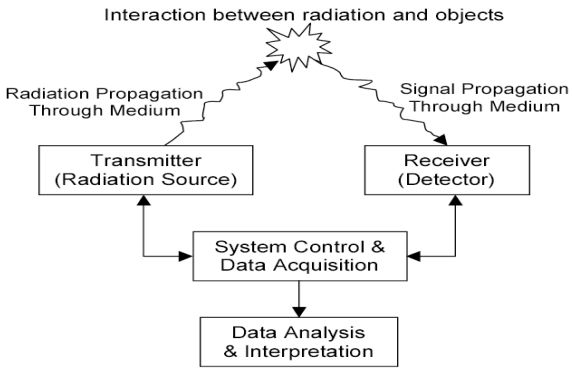

Figure 2.2 Schematic of a Lidar system consisting in a transmitter, receiver, system control and data acquisition.

The main requirements for laser transmitter are: emission at suitable wavelengths (typically UV or visible wavelengths to ensure molecular backscattering), short pulse length (a few 10 ns), low pulse energy to provide eye safety for full-time, long-term unattended operation (typically a few µJ in the visible region or mJ in the UV region), and low divergence (less than 1mrad, usually achieved through beam expanding optics).

The requirements for a receiving telescope are quite easy to meet for Lidar applications. The most important parameter is the area of the lenses, and of course its transmittance. The optic devices have to match that product in order to avoid transmission losses and shadowing effects. To separate the signal from unwanted background, the field of view of the receiver can be made rather narrow, a little wider than the divergence of the transmitted beam. Further reduction of the background is accomplished by spectral filtering. For elastic backscatter, the bandwidth can be made quite narrow, and efficient filtering is easily achieved using standard components. The simplest elastic-backscatter Lidar at UV- Vis wavelength may be compact, portable, eye safe and is now available in a commercial way. Lidar systems have windows-

based software package run by a PC laptop computer. Cimel Lidar is a manageable system can be easily mounted by a person on robot to be tunable to various pointing angles. EZ Aerosol Lidar system is completely flexible to angular measurement.

2.1.4.1 Cimel CE-370 aerosol and cloud micro Lidar

The Cimel Lidar, is used to retrieve aerosol and cloud optical properties. The laser is passively Q-switched. For standard operation, the laser frequency is set around 4.6 kHz and approximately 4 μJ per pulse exit the laser at this rate. The pulse length is less than 10 ns and the beam divergence is approximately 55 μrad. The solid-state diode-pumped system features appreciable operational lifetime (> 30000 hours). The telescope is a 1000 mm height cylinder with a 220 mm diameter and a focal length around 1 m (Figure 2.3).

Figure 2.3 Schematic of Cimel Lidar system 532 nm (Cimel document) receiver and transmitter part

An optical fiber is used to connect the telescope to the optoelectronic part of the Lidar. The fiber determines the diameter-divergence product of the beam. The receiver field of view is approximately 55 μrad. This extremely narrow field of view eliminates most multiple scattering problems and limits detection of ambient solar background. A laser pulse interacts with the optical fiber surface creating backwards scattering that reaches the detector. This energy is high enough to momentarily saturate the photodiode and a run-on signal is created, which decays gradually through the length of the sampling period. This so-called afterpulse

should be taken into account in data post processing. An acousto-optical modulator placed along the receive path enables to reduce the after pulse signal. An avalanche photodiode detector manages signal acquisition using photon counting detection mode to provide an accurate detection of low-level Lidar signals. Our Lidar featured 15 m maximum vertical resolution and its design allows for up to 30 km altitude.

A special signal handling problem in Lidar is the backscatter intensity which has basic $1/R^2$ dependence thus the detection system must be able to handle close- range signal at almost the same time as weak signal from afar. The main problems in the detection of Lidar signals are the huge dynamic range which spans many orders of magnitude. It is needed to compress the Lidar signal to reduce the dynamic range. Special hard- and software is generally used to accumulate a larger number of shots.

2.1.4.2 Leopshere EZ 540 aerosol and cloud Lidar

The EZ Leosphere Lidar system is designed to measure optical properties of aerosol layers and low level and cirrus cloud. Additionally it is as a device for global tracking of large scale transport of aerosol. The Lidar is safe and secure to measure every kind of pollution. The EZ Lidar is a bistatic backscatter Lidar (UV). It is able to measure the low diameter aerosol (0.3 μm). The system is easy to use, portable, robust and able to work in an unattended mode. The EZ LIDAR is composed of two main elements. First, the optical head contains the laser emission and optical receiver modules (Figure 2.4).

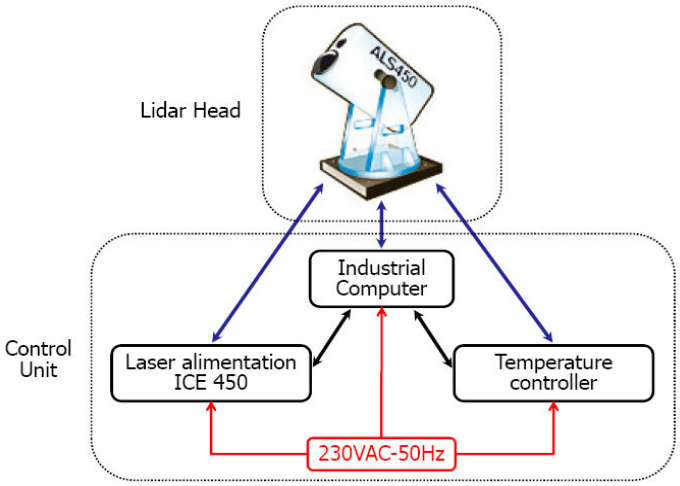

Figure 2.4 EZ aerosol Lidar diagram (Leosphere documents)

Second, the control unit includes the EZ LIDAR electronics control and acquisition. EZ LIDAR might include optional units as a thermal regulation system, the automatic scanning system and the external cooling system. The transmitter is a UV laser (tripled Nd-YAG) at 354.7 nm with a 20 Hz frequency and output energy of 30 J/m^2. The pulse energy is 16 mJ (±5% shot by shot). The EZ Lidar range detection is between 150 m to 15 km. The spatial resolution is 15 m and typical temporal resolution is between 10 to a few minutes.

Table 2.1 summarizes the characteristics of both UV and VIS systems.

Table 2.1 The performance, and technical specification of Cimel and leosphere lidar

	Cimel	Leosphere
Wavelength	532 nm	355 nm
Nd-YAG Q - switch mode	Frequency -doubled	tripled
Laser pulse energy	14 µJ	16 mJ
Pulse repetition frequency	4.7 KHZ	20 Hz
Vertical resolution	15 m	15 m
Weight	30kg	35kg
Range	250 m to 30 km	200 m to 15 km
Overlap correction up to	1100m	200m

2.1.5 Geometric form factor in a Lidar equation

The return signal in the inhomogeneous atmosphere changes dramatically with increasing distance. For a Lidar system with a narrow field of view and the usual separation between transmitter and receiver optical axes, an exact interpretation of Lidar return signal in the short range is complicated by the incomplete overlap between the transmitted laser beam and the field of view of the receiving optics. To interpret the Lidar signal properly at short ranges, it must be corrected by G(R) factor. Theoretical calculation of the geometric factor is possible when the specification and configuration of optical elements are known. However, considering a mobile system, an experimental estimate of G(R) is more suitable (Dho et al., 1997). Practically, the best experimental scheme is a horizontal Lidar beam to approach the homogeneous atmosphere as close as possible. If we multiply both sides of [2.1] by R^2 and use the logarithm it yields.

$$\mathrm{Ln}\left[\mathrm{P}(\mathrm{R})*\mathrm{R}^2\right] = \ln \mathrm{C} + \ln \beta(\mathrm{R}) + \ln \mathrm{G}(\mathrm{R}) - 2\int_0^R \alpha(r)\,\mathrm{dr} \qquad [2.9]$$

G(R) ranges between 0 and $G_{max} = 1$. R_1 is a distance which beyond it, $\ln G(R \geq R_1) = 0$. So the right hand side of [2.11] can be described by a linear function.

$$\text{for } \mathrm{R} \geq \mathrm{R}_1,\ \mathrm{Ln\,C} + \ln \mathrm{B}(\mathrm{R}) - 2\int_0^R \alpha(r)\,\mathrm{dr} = \mathrm{AR}+\mathrm{B} \qquad [2.10]$$

where A and B are the coefficients of the linear function. Below the appropriate distance R_1, $G(R) < 1$ and we write:

$$\mathrm{G}(\mathrm{R}) = \exp(\mathrm{Ln}\left(\mathrm{P}(\mathrm{R})\mathrm{R}^2\right) - (AR + B) \qquad [2.11]$$

After linear fitting, R_1 is obtained using the linear equation and for each range we calculate the geometric overlap function. Figure 2.5a shows the linear function of $\ln(PR^2)$ which has drew to find the reference range beyond it the G(R) is unity. Figure 2.5b shows the geometric factor which have been calculated using the linear function described through formula [2.10] to [2.11]. The geometric factor for both lidar has been presented in Table 2.1.

It can be observed for Cimel the data under 1200m had to be corrected from geometric factor whereas for Leosphere is less than 200 meter (table 2.2).

Table 2.2 value of geometric factor

Cimel	Above 1100m G(r)=1
Leosphere	Above 200m G(r)=1

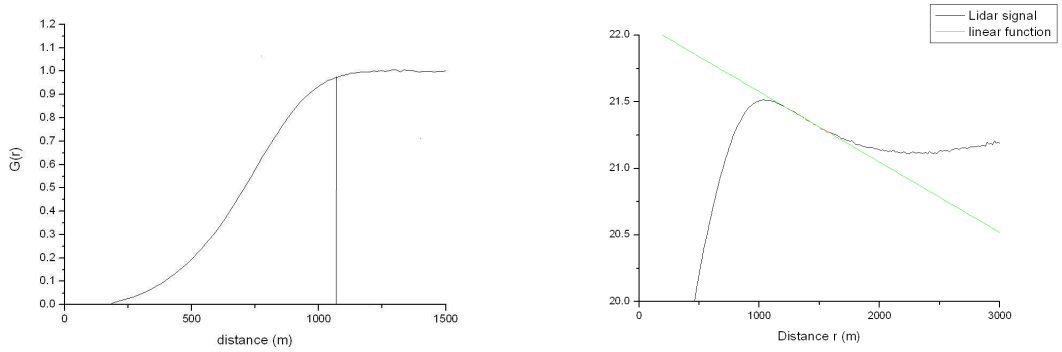

Figure 2.5 Geometric function of Lidar signal a) Geometric factor which is equal to 1 above 1100 m and under this height is corrected b) linear function fitting

2.1.6 Backscattering and extinction coefficient retrievals

The solution of the Lidar equation helps us to retrieve two unknown aerosol scattering and absorption quantities α and β. The simple relationship of total backscatter coefficient $\beta(R)$ which is proportional to $\alpha^k(R)$ allows us to transform the integral of Lidar equation into the corresponding Bernoulli's differential equation to obtain extinction and backscatter aerosols coefficients. We are summarizing the resolved Lidar equation for calculation of aerosol backscatter coefficient which is well described by Ansman and Muller (2005) using Klett method (Klett, 1981). In the same way as the molecular Lidar ratio, we introduce the particle Lidar ratio denoted L_{aer}. L_{aer} depends on the size distribution, shape and the chemical composition of the particles and it is consequently related to range.

$$L_{aer}(R) = \frac{\alpha_{aer}(R)}{\beta_{aer}(R)} \qquad [2.12]$$

The most critical input parameter in Klett method is the particle Lidar ratio $L_{aer}(R)$. It depends on the micro-physical, chemical, and morphological properties of the particles and relative humidity. The Lidar ratio is a function of altitude especially when the different source of aerosol (marine, anthropogenic urban, biomass burning, and/ or desert dust particles or mixtures of these) are present in superimposed layers. Typical Lidar ratios of the mentioned different aerosol types given in Table 2.3 are measured with Raman Lidar at 532nm (Ansmann and Müller, 2005).

Table 2.3 Typical Lidar ratio for different aerosol types at 532 nm wavelength determined with a Raman Lidar (Ansmann and Müller, 2005).

Marine particles	20-35 sr
Saharan dust	50-80 sr
Less absorbing urban particles	35-70 sr
Absorbing particles from biomass burning	70-100 sr

The Lidar ratio has a value between 20 and 100 sr and this variability makes difficult its estimation in real cases. Even in the well-mixed layer, the Lidar ratio is not constant with height because relative humidity increases with height. In cases with accompanying Sun photometer observations that deliver the optical depth, a column-related Lidar ratio can be estimated from the ratio of the optical depth to the column-integrated backscatter coefficient. This Lidar ratio can only be considered as a first guess, the true Lidar ratio profile remains unknown. The Lidar ratio is also wavelength dependent. Table 2.4 shows the aerosol Lidar ratio in different geographical area in that the aerosol type is different. The data presented in the table were acquired in the framework of EARLINET (Bösenberg and et al., 2003; Mattis et al., 2004). The central European haze and free tropospheric lofted particle layers such as Saharan dust, forest fire smoke from Siberia and North America and anthropogenic haze plumes from North America have been observed. During the Second Aerosol Characterization Experiment (Russel and Heintzenberg, 2000) in the summer of 1997, the pure marine particles which originated from the North Atlantic, and aged urban particles

which were advected from central and south Europe have been observed. Due to local and regional anthropogenic haze over the central European site Lidar ratios typically ranges from 45-60 sr with a mean value of 53 sr at 532 nm. Aging and mixing with dust and anthropogenic particles over southern Europe caused average Lidar ratios of 45±10 sr. The values are 10 to 40 % larger at 355 nm.

Table 2.4 Mean values and standard deviation of particle Lidar ratio at 355 and 532 nm (Müller et al., 2007).

Urban haze		S355, sr	S532, sr	S355/S532
Central Europe (EARLINET)	PBL	58 ± 12	53 ± 11	1.1 ± 0.3
Southwest Europe (ACE 2)	Free troposphere		45 ± 9	
North America (EARLINET)	Free troposphere	53 ± 10	39 ± 10	1.4 ± 0.2

At first we want to solve Lidar equation [2.3] to obtain aerosol backscattering coefficient, we introduce the function of Y(R):

$$Y(R) = L_{aer}(R)\,[\beta_{aer}(R) + \beta_{mol}(R)] \qquad [2.13]$$

Y(R) in equation [2.13] is a function of $\alpha_{aer}(R)$. The backscattered signal is the first parameter obtained by Lidar with good accuracy. We obtain the aerosol extinction $\alpha_{aer}(R)$ from the relationship between aerosol and molecular backscatter and extinction coefficient. The equation [2.3] can be written as formula [2.15] with replacement of equation [2.14].

$$S(R)L_{aer}(R)\exp\{-2\int_0^R [L_{aer}(r) - L_{mol}]\beta_{mol}(r)dr\} = E_0\eta_l Y(r)\exp[-2\int_0^R Y(r)dr] \qquad [2.14]$$

We take the logarithm of both sides of equation and differentiating them with notation to R

$$\frac{d\ \ln(S(R)L_{aer}(R)\exp\{-2\int_0^R [L_{aer}(r)-L_{mol}]\beta_{mol}(r)dr\}}{dR} = \frac{1}{Y(R)}\frac{dY(R)}{dR} - 2Y(R) \qquad [2.15]$$

We solve the Bernoulli equation, for the boundary condition at reference altitude R_0.

$$Y(R_0) = L_{aer}(R_0)\ [\beta_{aer}(R_0) + \beta_{mol}(R_0)] \qquad [2.16]$$

Total backscattering is obtained as following

$$\beta_{aer}(R) + \beta_{mol}(R) = \frac{S(R)\exp\{-2\int_{R0}^{R} [L_{aer}(r) - L_{mol}(r)]\beta_{mol}(r)dr\}}{\frac{S(R_0)}{\beta_{aer}(R_0) + \beta_{mol}(R_0)} - 2\int_{R0}^{R} L_{aer}(r)T(r,R_0)S(r)d} \qquad [2.17]$$

In that the transmission function is explained by equation [2.19]

$$T(r,R_0) = \exp\{-2\int_{R0}^{r} [L_{aer}(r') - L_{mol}]\beta_{mol}(r')dr'\} \qquad [2.18]$$

Then we have calculated particle extinction coefficient $\beta_{aer}(R)$ by subtracting the molecular from total backscatter. We integrate the equation [2.17] by starting from the reference range at the remote end of the measuring range using a backward integration (Ansmann and Müller, 2005). Klett- backward inversion method (Klett, 1985) avoids numerical instability. The R_0 reference is chosen where the particle backscatter coefficient is negligible compared to the known molecular backscatter value, $\beta_{aer}(R_0) << \beta_{mol}(R_0)$. The reference altitude has been chosen to minimize the impact of aerosol scattering typically is arrange above 3 to 4 km (see Figure2.4).

2.1.7 Determination of the Planetary Boundary Layer (PBL) top height

Lidar permits the detection of the boundary layer (BL) top with a vertical resolution of few meters and a temporal resolution in the range of seconds to minutes. Even the highest BL top of 3-4 km in Europe or 4-6 km over the Sahara can be detected. The detection of the lowest BL is limited by the lowest detected height by lidar system (above a few hundred meters). Water clouds with optical depth above 2 are caused the light to be attenuated which is the only limit of Lidar for detection. In the presence of a cumulus cloud deck, the BL top cannot be detected. But in case of broken cloud fields during convectively active days, Lidars can detect the BL top (Baars et al., 2008). Clouds can form at the top of mixed layers, and at the bottom of stable boundary layers. The thermodynamic variables (water, temperature, potential temperature variables) are used to describe the state of the cloudy boundary layer. If a parcel of air is composed in part of water vapor, is forced to rise, it may eventually reaches a pressure and temperature at which condensation will occur. The lifting condensation level (LCL) is the saturation level for and unsaturated parcel lifted dry adiabatically (Stull, 1988). The height of PBL in presence of cloud is normally known lifting condensation level (LCL) height and often defines cloud base. When sufficient moisture and buoyancy is present there is cumulus cloud. If a cloud is detected in Lidar profile, only the values below cloud base are used for determination of the BL top. If no significant gradient can be detected, it is very probable that this cloud has formed within the BL and no BL top height is provided (Brooks, 2003).

The top of the boundary layer can be determined using different instrument, parameters and methods (Seibert et al., 2000). Active remote sensing of meteorological parameters like wind profiler and remote sensing of trace gases are applied for detecting the PBL height. Sodar technique, radio acoustic sounding, ceilometers, and Lidar appear to be most appropriate instrument for continuous BL top detection (Wiegner et al., 2006). Here we describe the methods which are well known for PBL height detection from Lidar signal. We can identify two different methods, the first one based on the aerosol gradient at the interface between the free troposphere and the boundary layer, and the second one based on the Lidar signal fluctuation measurements in the transition zone.

The derivation of the Lidar signal is the most direct way to find the temperature inversion layer which is related to the top of the boundary layer. In gradient method, the mixing height

(PBL height) corresponds to the altitude of the absolute negative minimum of the first derivation of the range corrected Lidar signal (RSCS). The logarithm of the range-corrected signal might also be used. The minimum in the second derivative of the RSCS (inflection point method) corresponds to a mixing height located just below altitude obtained by gradient method and best fits with PBL height derived from radio soundings (Menut et al., 1999). A recent approach (Steyn et al., 1999) has been made by fitting an ideal backscatter profile to real profile to determine the midpoint and the extent of the transition zone. The artificial profile is defined as

$$B(z) = \frac{B_m + B_u}{2} - \frac{B_m - B_u}{2} erf(\frac{z - z_i}{d}) \qquad [2.19]$$

where B_m and B_u are mean coefficient of ideal backscatter profile in and above PBL, respectively *erf* is the error function and *d* is related to thickness of the transition zone. The advantage of this method is that beside the PBL top height also information on the extent of the transition zone can be achieved by analyzing the parameter *d*. Cohn and Angevine (2000) have proposed a method based on a wavelet covariance transform (WCT) to find the transition zone associated with the gradient in the RSCS (see also Brooks (2003)). The WCT is defined as

$$W_f(a,b) = \frac{1}{a}\int_{z_b}^{z_a} f(z)h((z-b)/a)dz \qquad [2.20]$$

Where f(z) is the signal of interest, in our case a Lidar backscatter profile, and z_b and z_a are the lower and upper limits of the profile. The Haar function *h* is defined by

$$h(\frac{z-b}{a}) = \begin{cases} +1 : b - \frac{a}{2} \le z \le b \\ -1 : b \le z \le b + \frac{a}{2} \\ 0 : elsewhere \end{cases} \qquad [2.21]$$

A local maximum in $W_f(a,b)$ identifies a step in f(z).

The identification of boundary layer depth with gradient methods works well when background gradients are negligible and the transition zone sharp and well defined, but these conditions are frequently met. Under stable conditions, where mixing is poor, vertical

gradients are common both within and above the boundary layer, and the inversion layer may be a significant fraction of the depth of the BL as a whole, here the problem of identifying the BL depth in an automated manner becomes more complicated. It should be noted that under some conditions the boundary layer may be so ill–defined that an absolute top cannot sensibly defined.

Mixing takes place at the top of the PBL due to entrainment of free-troposphere or residual–layer air. This leads to a high variability of the measured atmospheric quantities in the transition zone, because alternating characteristic of the free-troposphere and PBL air are observed. The transition zone (or entrainment layer) is defined as the layer in which mixing of polluted boundary layer and clean free troposphere air significantly influence the aerosol concentration. The height at which the variability takes its maximum could be interpreted as the PBL top height (Menut et al., 1999). The variance is computed using equation [2.23] over a given time step. During nighttime under statically stable conditions, this method may fail because of the low exchange rate at the top of the PBL.

$$Var(z) = \frac{1}{k}\sum_{i=1}^{k}(S(z)_i - \overline{S(z)})^2 \qquad [2.22]$$

Figure 2.6 and 2.7 present an example of BL top retrieval by the aforementioned methods. The Lidar profile was acquired in Lille on 14 April 2007 at 12:00 UTC. The Lidar signal is plotted on left side of panel 2.6 and 2.7. The first significant gradient (Figure 2.6b) corresponds to the PBL top and gives an altitude of 645 m. The second derivative method gives an altitude a little bit lower than the first derivative, at 615 m. The altitude given by the first derivative corresponds to the top of the mixed layer while the altitude given by the second derivative corresponds to the middle of the transition zone (Menut et al., 1999). The first derivative of the Lidar signal logarithm (Figure 2.6d) gives an altitude at of 660 m, one step higher than the gradient method. When we compare with the temporal variance over 1 hour of the measured Lidar signal (Figure 2.7b) we find a maximum at also 645 m. The variance method in stable night time condition can be failed because of the low exchange rate at top of the atmosphere. Figure 2.7d shows the wavelet function to obtain atmospheric boundary layer. The ideal dilation is as large as the transition zone. Here we have calculate the WCT for a=30, 45, and 75 m. For a=75 m, we find the PBL top at 615 m. The value is exactly the same as found by the fitting method (Figure 2.7c). The retrieved BL height is 615 m and the width of the transition zone *d* is 105m.

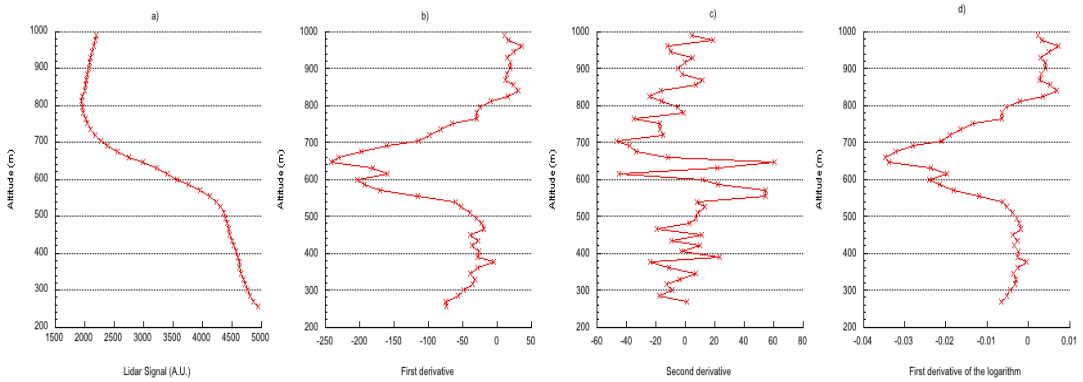

Figure 2.6 Comparison of different methods for the retrieval of BL top: a) lidar signal, b)The first significant gradient gives an altitude of 645 m; c)The second derivative method gives an altitude a little bit lower than the first derivative, at 615 m; d) The first derivative of the Lidar signal logarithm gives an altitude of 660 m.

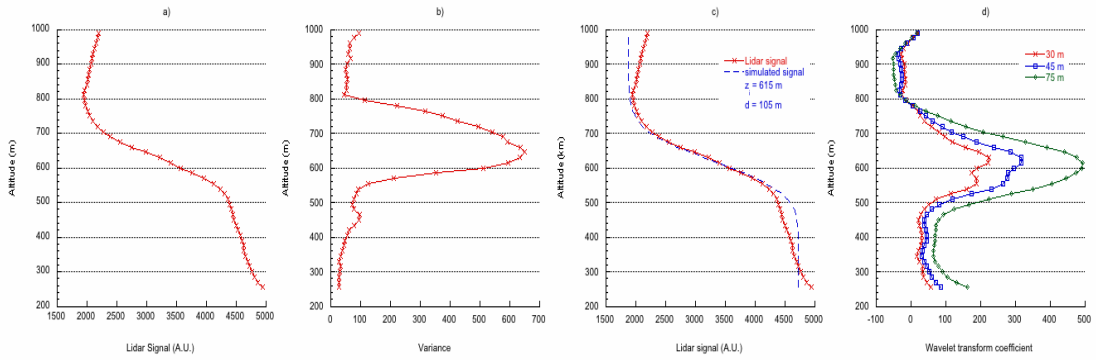

Figure 2.7 Comparison of different methods for the retrieval of BL top a) lidar signal; b) the temporal variance over 1 hour of the measured Lidar signal a maximum at also 645 m; c) the fitting method The retrieved BL height is 615 m and the width of the transition zone *d* is 105m; d) the wavelet function gives a PBL top at 615 m.

All those methods give very similar results, but the implementation differs significantly. More advanced methods like the WCT or fitting method are time consuming but provide more information on the width of the transition layer. However when the gradient are not well defined, it is necessary to supervised the retrieval. As we are interested in the top of the mixed layer we will used in the following the gradient method and the variance method.

2.2 Atmospheric column optical properties and ground-level mass concentration

2.2.1 Automatic Sun photometer

The measurement of aerosol optical properties is made by CIMEL sun/sky radiometers, which are a part of AERONET (**AE**rosol **RO**botic **NET**work, www.aeronet.gsfc.nasa.gov) global network. The instruments we used in this study belong to the French part of AERONET, the PHOTON network (loaphotons.univ-lille1.fr). The AERONET is a ground-based remote sensing aerosol network providing a long-term, continuous and readily accessible public domain database of aerosol optical, microphysical and radiative properties for aerosol research and characterization, validation of satellite retrievals, and synergism with other databases. The automatic-tracking sun and sky scanning radiometers measure sun and sky radiance in order to derive total column water vapor, Ozone and aerosols properties using a combination of spectral filters and azimuth/zenith viewing controlled by a microprocessor. A comprehensive description of the Sun photometer and AERONET is given by Holben et al. (1998).

2.2.1.1 Aerosol optical depth

The direct sun measurements are made within a 1.2° field of view at least every 15 minutes in eight spectral bands (340, 380, 440, 500, 675, 870, 940, 1020 nm). The direct sun measurements are then used to compute aerosol optical depth $\tau_a(\lambda)$ at each wavelength except for 940 nm which is used for precipitation of water in centimeters (Holben et al., 2001). Aerosol optical depth data are computed for three data quality levels: level 1.0 (unscreened), level 1.5 (cloud-screened), and level 2.0 (cloud-screened and quality assured).

The intensity of a beam of sunlight of a particular wavelength that reaches Earth's surface is given by

$$I = I_0 e^{-\tau m} \qquad [2.23]$$

Where I_0 is the intensity of sunlight just above Earth's atmosphere, τ is the total atmospheric optical thickness and m is the relative air mass and equal to 1 when the sun is directly overhead and is otherwise approximately equal to $Sec(\theta)$ where θ is the solar zenith angle. The total atmospheric optical thickness can be divided into three parts. One part is due to gases absorption and is assumed to be well-known for in the aerosol retrieval process. One

part is due to the fact that the atmosphere scatters sunlight out of a direct beam from the sun (Rayleigh scattering) and another part due to the scattering by aerosols. The Rayleigh optical thickness τ_R can be estimated at a given location from meteorological information (refer to section 2.1.4). The instrument is carefully calibrated using Langley plot method and integrating sphere for the sun and sky channels. So if a sun photometer measures light intensity then the voltage signal produced by instrument is directly proportional to intensity, and then

$$\tau_a = (\left[\ln\{(V/V_0)(r_0/r)^2\} \right] / m) - \tau_R \qquad [2.24]$$

where r_0/r is the ratio of the average to actual Earth-Sun distance. V and V_0 are the digital voltage and calibration voltage respectively. The accuracy in the estimation depends on the uncertainty in V and in V_0. The calibration accuracy becomes an obstacle because it causes an error of at least of 5%-10% of the optical thickness for $\tau_a(440\text{ nm}) \leq 0.2$. Total uncertainty in AOT is 0.01 above 440 nm and 0.02 below.

2.2.1.2 Size distribution and volume concentration

The AERONET inversion algorithm provides improved aerosol retrievals by fitting the entire measured field of radiances- sun radiance and the angular distribution of sky radiance- at four wavelengths (440, 670, 870, 1020 nm) to a radiative transfer model (Dubovik and King, 2000). Sky measurements are performed in the sun Almucantar. The objective is to get several scattering angles for the retrieval of aerosol optical properties and size distribution. Modeling the aerosol effects on atmospheric radiation, by solving the radiative transfer equation, requires the aerosol optical properties as aerosol optical thickness $\tau(\lambda)$ (loading), phase function $P(\Theta,\lambda)$ (angular dependence of light scattering), and single scattering albedo $\omega_0(\lambda)$ (ratio of the scattering efficiency to the total scattering efficiency).

The radiation field is driven by the aerosol complex index of refraction and particle size distribution in the size range 0.05 to 15 μm (Dubovik et al., 2002). The retrieval of particle volume size distribution was demonstrated to be adequate in practically all situations for $\tau_a(440\text{ nm}) \geq 0.05$. The error of the retrieved volume density changes as a nonlinear function of particle size distribution. In particular, for the intermediate size particle size range $0.1 \leq r \leq 7.0$ μm, the retrieval errors do not exceed 10% in the maxima of size distribution and may

increase up to 35% for the points corresponding to the minimum values of size distribution in this size range. For the edge $0.05 \leq r \leq 0.1$ µm of the assumed particle size interval, the accuracy of the size distribution retrieval drops significantly, because of the low sensitivity of the aerosol scattering at 440, 670, 870 nm to particles of this size. The retrieved size distribution volume is not independent in the sense that the retrieval technique insures only the fact that the retrieved combination of all of the parameters would accurately reproduce the measured radiation field in the scope of chosen radiative transfer model (Dubovik and King, 2000). The retrieval accuracy of size distribution also depends on the accuracy of radiative transfer model.

For each mode of the volume particle size distribution [dV(r)/ d lnr] the particle volume concentration, the median radius, and the standard deviation are computed. For this analysis, we defined all particles with radius smaller than 1 µm as belonging to the fine mode and all particles with radius larger than 1 µm as belonging to coarse mode. In fact practically all observed size distributions have bimodal structure with quite wide local minimum with low values of dV(r)/dlnr around 0.6 µm. The size size distribution can be written as

$$dV(r)/d\ln r = \sum_{i=1}^{2} \frac{C_{v,i}}{\sqrt{2\pi}\sigma_i} \exp\left[-\frac{(\ln r - \ln r_{v,i})^2}{2\sigma_i^{\,2}}\right] \qquad [2.25]$$

The exact location of the inflection point is not critical for estimating volume concentration (C_{vi}), the modal radius (r_{vi}) and width of the distribution (σ_i). It should be noted that the equations for computing c_{vi}, r_{vi} and σ_i are simple, general and their formulation does not assume any function for the size distribution.

$$\ln r_v = \frac{\int_{r_{\min}}^{r_{\max}} \ln r \frac{dV(r)}{d\ln r} d\ln r}{\int_{r_{\min}}^{r_{\max}} \frac{dV(r)}{d\ln r} d\ln r} \qquad [2.26]$$

$$\sigma_v = \sqrt{\frac{\int_{r_{min}}^{r_{max}} (\ln r - \ln r_V) \frac{dV(r)}{d\ln r} d\ln r}{\int_{r_{min}}^{r_{max}} \frac{dV(r)}{d\ln r} d\ln r}} \quad [2.27]$$

Volume concentration (in $\mu m^3/\mu m^2$) is given by [2.28]

$$c_V = \int_{r_{min}}^{r_{max}} \frac{dV(r)}{d\ln r} d\ln r \quad [2.28]$$

2.2.2 Monitoring of particle mass concentration

France is concerned about atmospheric pollution. 72% of the French people consider atmospheric pollution as a genuine health threat, and 45% state that they have been a victim of this type of pollution or personally know someone who has. French Environment and Energy Management Agency (ADEME, www.ademe.fr) support these basic rights by funding and providing technical assistance to an air-quality monitoring and pollution-forecasting program. The agency works in cooperation with the Ministry of Ecology and Sustainable Development, in accordance with its public health objectives. They publish the *Bulletin de l'Air* based on ATMO indexes calculated by certified air-quality monitoring associations (AASQA, see www.atmo-france.org and Figure 2.8). Each day, the bulletin indicates the current level of pollution in France's major urban areas and provides a next-day forecast. In 2006, there were 34 agencies managing 2,200 fixed sensors in total over 750 measuring stations in the entire territory. These sensors measure: sulphur dioxide, particulate matter, carbon monoxide, Ozone and nitrogen dioxide, benzene, heavy metals and polycyclic aromatic hydrocarbons. These associations have a website on which information relative to air quality can be obtained in almost real time.

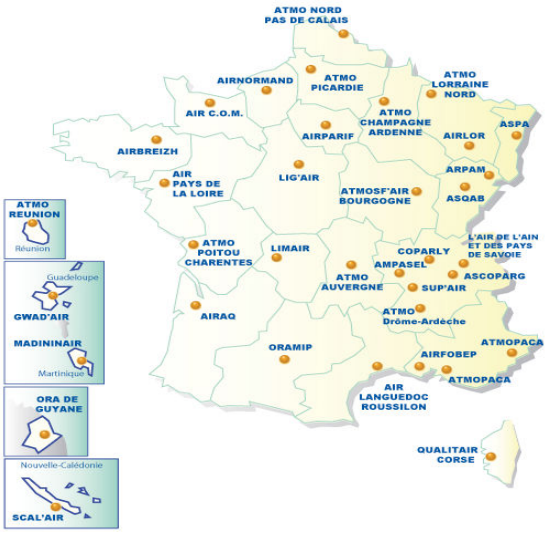

Figure 2.8 Map of regional AASQA (credit *www.atmo-france.org*).

Particle mass automatic station measurements are classified to different category based on the distance between the sources of emission of particle matter. The rural station (*peri-urbaines*) are placed at a distance between 10 km and 50 km (3 km and 10 km) from the important source of emission whereas the urban stations are near to the roads with less than 2500 vehicles per day (in the diameter of 50 m). The traffic stations are situated in the way of the automobile circulation. The concentrations of SO2, NO, NO2, CO, O3, PM10 and recently PM2.5 have continuously been monitored and data are available on an hourly basis. In the following we have used the data collected by ATMO Nord-Pas de Calais (www.atmo-npdc.fr and Figure 2.9).

Figure 2.9 Particle mass monitoring stations in France and Nord Pas de Calais operating by ATMO Nord Pas de Calais (credit *www.atmo-npdc.fr*).

The measurement methods are manual gravimetric method and automated continuous monitors. In manual gravimetric method the aerosol samples are deposited or filters or foils, which are conditioned at the reference air humidity, and then weighted and automated continuous monitors use alternative methods for generating a quasi-continuous signal for mass concentration. When these devices are used, their equivalence to standard methods must be checked at each location, or a conservation algorithm has to be applied. One problem that is frequently encountered concerns losses of volatile components from filters that are slightly heated in order to avoid condensation.

Tapered element oscillating microbalance measures the change in resonant frequency of the oscillating filter that gets loaded with particles (Patashnick and Rupprecht, 1991). Earlier measurement systems (filters at 50 degrees) show average mass losses of up to 30%. By contrast, new systems with FDMS (filter dynamics measurement system) cover this problem. Collected mass in the substrate is proportional to the decrease in the resonant vibrational frequency of the tube. This approach appears to have fewer artefacts, although variation in temperature, humidity, pressure and external vibrations can sometimes affect the accuracy of the measurement (Baron and Willeke, 2005). Figure 2.10 shows a typical arrangement for TEOM.

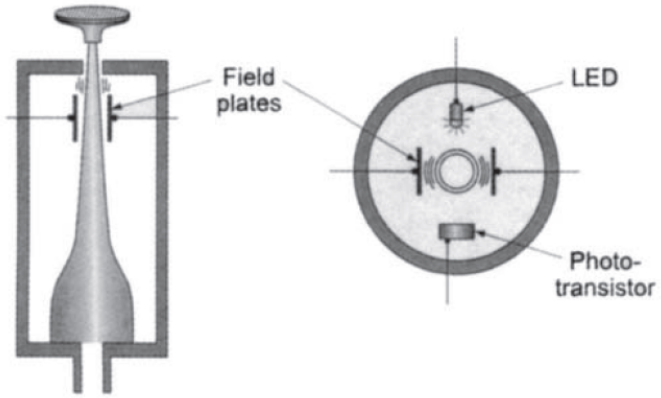

Figure 2.10 Typical arrangement for TEOM (after Baron and Willeke (2005))

The equation describes TOEM system and it is derived from an equation of motion of simple harmonic oscillator:

$$\Delta m=k_0[(1/f_b)^2-(1/f_a)^2] \quad [2.29]$$

Δm is the collected mass, f_b is the oscillating frequency after collection and f_a is the frequency before the sample collection. K_0 is a constant, unique to each tapered. As the collection medium collects aerosol, the mass increases, thereby decreasing the frequency of oscillation. As TEOM uses a filter collection medium then particles which are not collected by filter do not represent significant mass. If the collection filter became sufficiently loaded may be the saturation occurs which is cause an error. The volatilization problem applies to the TEOM. To reduce relative humidity, this instrument is often operated at 323 K (50°C), which is high enough to vaporize semi volatile aerosol material such as ammonium nitrate and certain organic compounds.

2.2.3 Time variation of particulate matter and aerosol optical thickness

The evolution of particle mass concentration and aerosol optical thickness depends on several factors including meteorology and geographical distribution of local source of pollution. On a given location, there is a significant seasonal variation in both AOT and PM. For example, the temperature inversion in winter favors an increase in ground-level PM2.5. Moreover, condensation of semi-volatile species favored by cold temperature increases PM2.5 during wintertime (Van Dingenen et al., 2004). In this work, we have studied the

monthly evolution of PM10, PM2.5 in Lille and Dunkerque in 2007 and 2008. The first one was organized in Lille in spring 2007, the second one in winter 2007-2008 in Dunkerque and a summer sea breeze study in Dunkerque. We present here the annually, monthly and daily average of particle mass concentration and AOT for three stations: Lille-Faidherbe (referred as Lille), Dunkerque-centre (DC-traffic) and Dunkerque-Petite-Synthe (PS-urban) as those two latter sites were also measuring PM2.5 in the Dunkerque area. The distance between Lille and Dunkerque is about 65 km. Position of Faidherbe, Petite-Synthe, Dunkerque Centre stations, Lidar and Sun photometer in Lille and Dunkerque urban area is shown in figure 2.11 and 2.12.

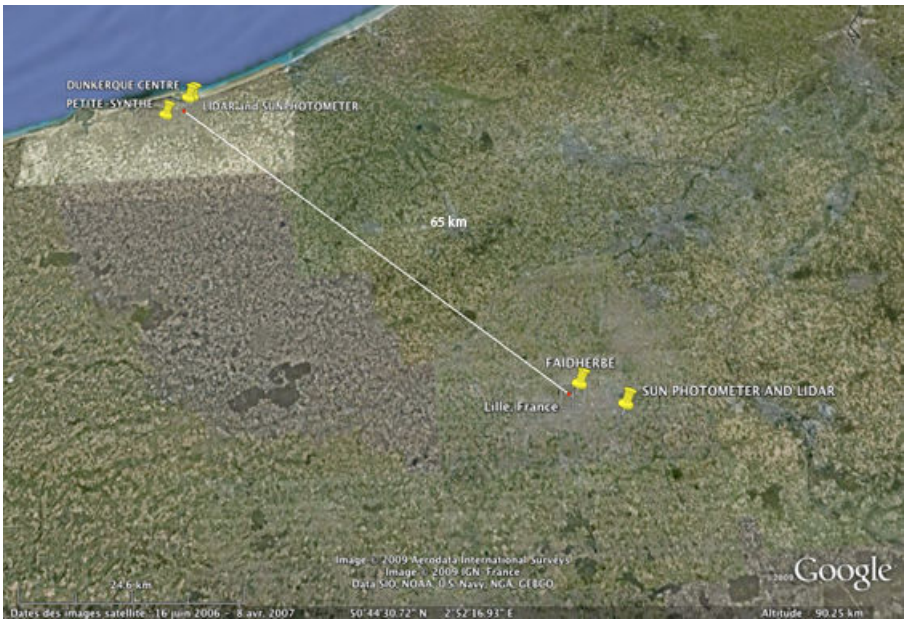

Figure 2.11 Position of Faidherbe, Lidar and Sun photometer stations in Lille urban area

The industrial activities are located in the northern part of Dunkerque while the population is in the central area. We have used here the uncorrected PM2.5 and PM10 data as the correction was not available over 2007 and 2008. The validated corrected PM2.5 data were available after 2008. So in the chapter 3 and 4 I have corrected the PM2.5 data using the described method in chapter 3. In the chapter 5 the corrected data have been used. Regarding the AOT and Sun photometer derived optical properties, we consider only two sites: Lille

(building of Laboratoire d'Optique Atmosphérique in Villeneuve d'Ascq) and Dunkerque (building of Laboratoire de Physico-Chimie de l'Atmosphère).

Figure 2.12 Position of the Petite-Synthe, Dunkerque Centre and Sun photometer stations in the Dunkerque urban-industrial area.

There is not a strong difference between Lille and Dunkerque on an annual basis. Table 2.5 presents the annual average for the three considered stations in 2007 and 2008. The annual average is very close for the two stations in Dunkerque and slightly higher than in Lille. As a comparison, the regional aerosol background annual average for continental Europe are 7.0±4.1 μgm^{-3} and 4.8±2.4 μgm^{-3} for PM10 and PM2.5 respectively (Van Dingenen et al., 2004). It is observed from the annual average in 2008 compared to 2007 that the particle mass concentration has decreased between 10 and 20% in the three stations. The AOT is close to 0.2 for both sites (Table 2.6). A decrease in the AOT is observed in 2008 (compared to 2007) in Dunkerque but not in Lille. When comparing seasonal cycle of AOT and PM, we need to keep in mind that we have much less sun photometer observations than ground-level PM because of the cloud cover. The number of days with AOT observations is close to 200 (±20) days per year for both sites while the PM concentration measurement is 363. PM can be measured in clear and cloudy days. But the days in that we have the AOT

measurement are the clear days or with thin clouds. This is crucial in winter when cloud cover is persistent.

Table 2.5 Annual average of PMx and PM2.5/PM10 for 2007 and 2008 in Lille and Dunkerque. The number in paranthesis are the standard deviation.

	PM2.5 (µg/m^3)			PM10 (µg/m^3)			PM2.5/PM10		
	Lille	D.C.	P.S.	Lille	D.C.	P.S.	Lille	D.C.	P.S.
2007	12 (4)	15 (3)	14 (3)	21 (5)	24 (5)	25 (5)	0.59	0.65	0.57
2008	10 (2)	12 (3)	13 (2)	18 (4)	21 (3)	22 (3)	0.57	0.56	0.60

. Table 2.6 Annual average of AOT for 2007 and 2008 in Lille and Dunkerque. The numbers in paranthesis are the standard deviation

	AOT	
	Lille	D.C.
2007	0.20(0.07)	0.24(0.09)
2008	0.23(0.08)	0.19(0.04)

The 24-h average of PM2.5 exceeds the US environment protection agency (EPA) regulatory threshold of 15.4µg/m^3 about 59 days in Dunkerque-Centre, 48 days in Dunkerque-Petite-Synthe and 37 days in Lille for 2008. Over 2007-2008, 6 days in Lille and 8 days in Dunkerque are above the U.S. EPA "unhealthy conditions for special groups" category threshold (more than 40.4µg/m^3). Table 2.7 gives the corresponding dates when the daily PM2.5 is over 40.4µg/m^3 in Lille or in Dunkerque. We observe that:

- Most of the time, the 40.4 µg/m^3 threshold is reached in both cities and corresponds to winter conditions.
- The associated AOT is variable and can be a factor 2 for the same PM2.5 value (e.g. on day 12/31/2008 and 12/20/2007 in Lille).
- Most of the time the associated AOT are higher in Dunkerque than in Lille.

Table 2.7 USP condition days (the daily average of PM2.5 higher than 40.4µg/m^3) in Lille and Dunkerque. The associated AOT is also given.

PM2.5 (µg/m^3)			AOT		
Lille	P.S.	D.C.	Lille	Dunkerque	Date
36	46	49	0.63	0.43	3/28/2007
47	51	54	0.19	0.21	12/19/2007
63	60	67	0.16	0.24	12/20/2007
47	41	49	0.14	0.21	12/21/2007
40	52	54	0.17	0.22	2/19/2008
29	52	58	0.28	0.53	2/20/2008
46	52	46	0.12	0.12	12/30/2008
63	53	51	0.32	0.22	12/31/2008

On a monthly basis the correlation between Dunkerque (D.C.) and Lille station is very high (R^2=0.83 for PM2.5 and R^2=0.69 for PM10). The seasonal cycle is weak but significant. On both sites, the pollution level is increasing continuously from January 2007 to April 2007 and then decreases until September. The concentrations increase again during winter. The monthly average AOT time series follows the same trend as the PM in the beginning of the year, increasing from January to April. The wintertime maximum is clearly observed on the monthly PM2.5 and PM10 average time series (Figure 2.13 and 2.14). In spring, we observe high AOT and PM2.5 while in winter we can observe low AOT but high PM2.5 (Figure 2.15). The AOT signal is also very close for both sites. The PM2.5 concentration trend in the three stations follows a very similar pattern during 2007 and 2008 despite of March 2007, January and February 2008 which is observed long range transport of aerosol over Europe. After a moderate rise from January to April 2007 then the mass concentration declines during summer 2007. After October there is another increase in level of pollution. Both peaks are in moderate situation. In 2008, two peaks of pollution are observed in February and May, whereas after August there is a smooth upward trend.

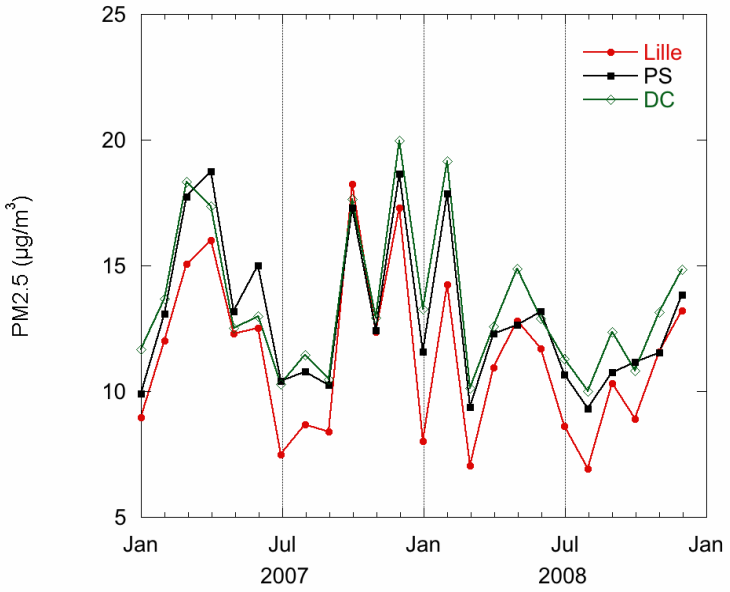

Figure 2.13 Monthly average of PM2.5 in Lille, DC and PS between 2007 and 2008

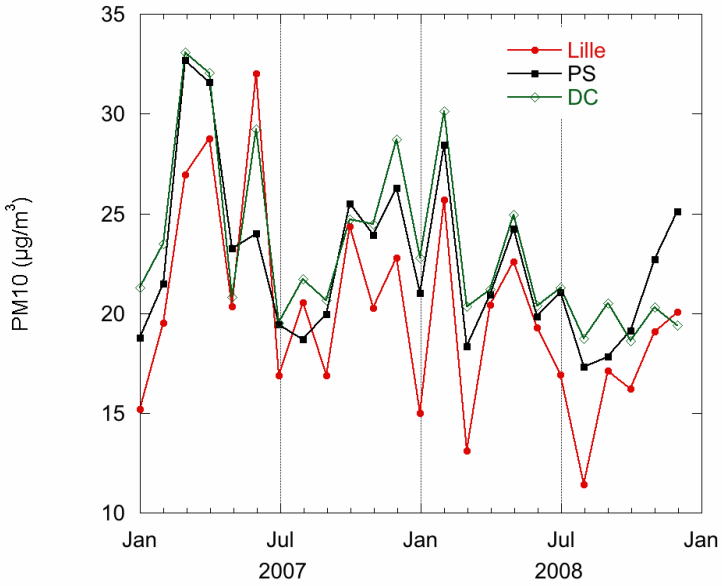

Figure 2.14 Monthly average of PM10 in Lille, DC and PS between 2007 and 2008

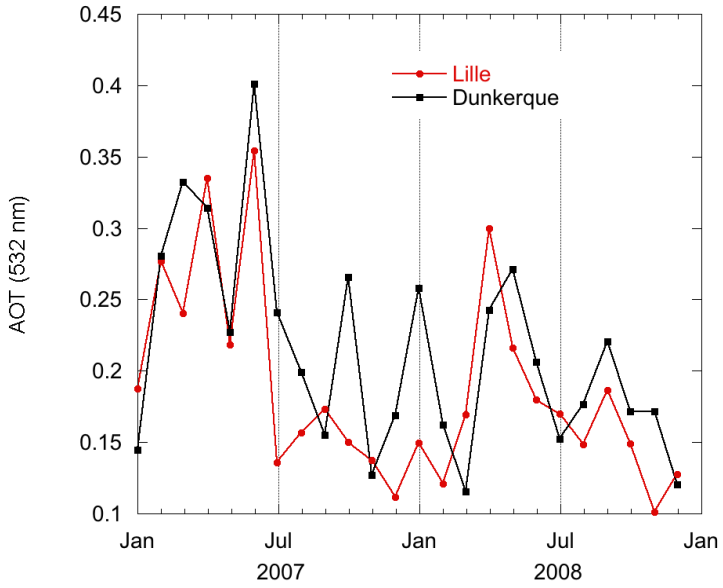

Figure 2.15 Monthly average of sun photometer aerosol optical thickness (level2) 2007 and 2008 in Lille and Dunkerque.

Figure 2.16 is a zoom on spring 2007 showing the daily evolution of both PM2.5 and AOT for Lille (see chapter 3). Both parameters show the same tendency during this period. AOT are rather high, indicating a contribution of long range transport. When zooming on the winter condition (Figure 2.17 and see chapter 4), the two parameters tend to be less related. In fact the winter pollution episodes are characterized with a moderate wind and high inversion of temperature during morning which means the higher temperature in the ground compare to the altitude. It will create warm air coverage over the pollutants and does not let them to be dispersing in the atmosphere. Further more certain measurement has shown that the semi-volatile composition (nitrate or organic composition) are appeared in the low temperature in winter more than summer.

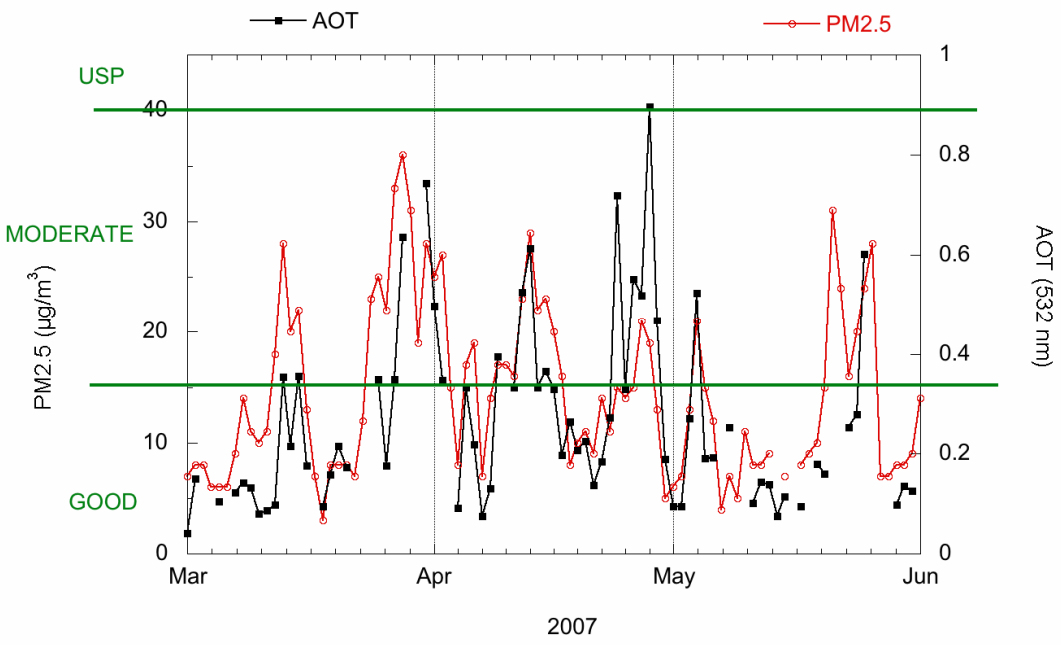

Figure 2.16 Daily average of aerosol optical thickness and PM2.5 mass concentration in Lille during spring 2007.

During summer, the daily PM2.5 concentration is much less than in winter. As it can be observed in Figure 2.18 there is not high concentration of the particle mass in USP conditions. We can observe an increase in PM concentration at the end of July, which in coincidence with sea breeze event that will be examined in chapter 5.

The relationship between AOT and PM is sensitive to aerosol vertical distribution and aerosol physical properties. The observed variability of the particle concentration and size distribution results from different processes including local dynamics and in particular changes in the mixing layer height bringing more or less concentrated boundary layer air to the sampling site depending on emission intensity at the surface, seasonality of air mass origin advected to the site, and photochemical processes leading to secondary particles formation. In addition, the frequency of new particle formation events changes according to season leading to both seasonal and diurnal variability. It is not easy to dissociate the each processes role as they may be enhanced or suppressed by identical variables.

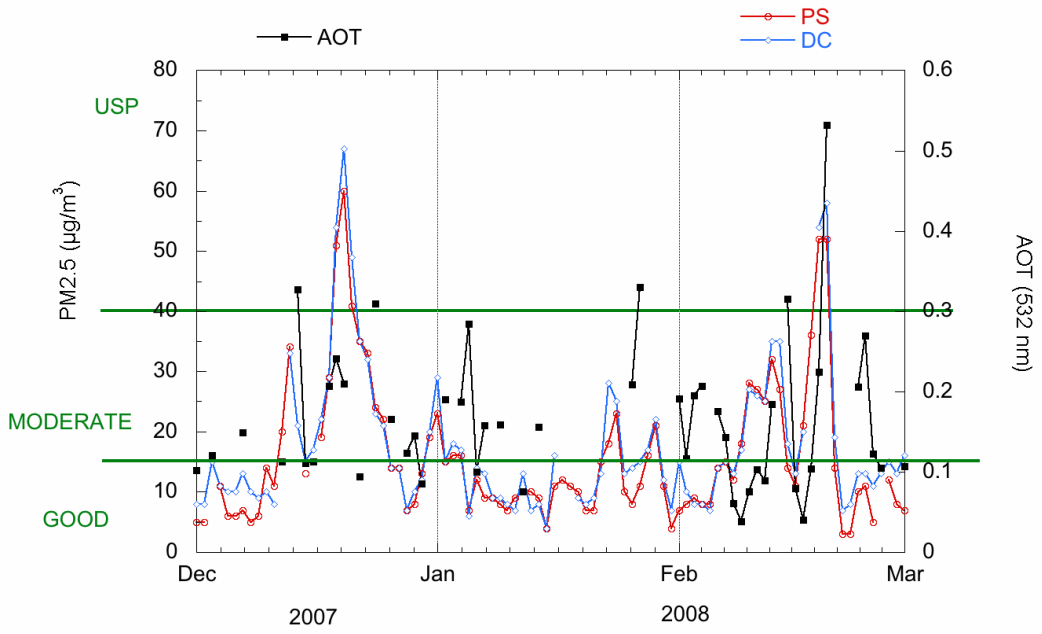

Figure 2.17 Daily average of aerosol optical thickness and PM2.5 concentration in Dunkerque during winter 2007-2008.

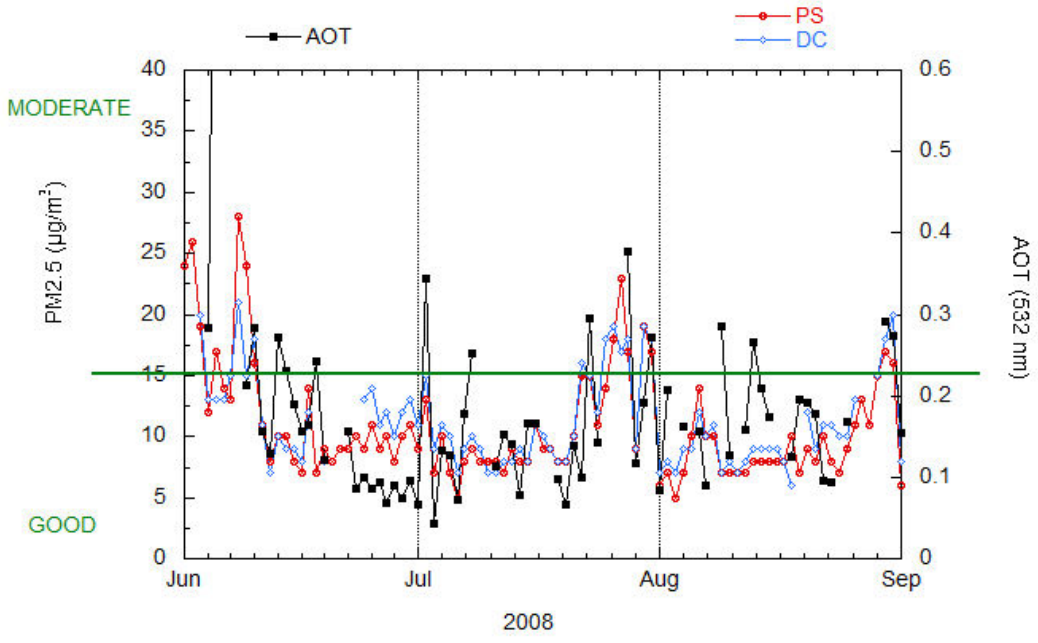

Figure 2.18 Daily average of aerosol optical thickness and PM2.5 mass concentration in Dunkerque during summer 2008.

Between summer and winter, we can notice a change in the shape of the size distribution (Figure 2.19 for Lille and Figure 2.20 for Dunkerque). This change is also related to a change in the volume fine fraction. In winter in Lille, the volume fine fraction is 50% while it is 28% in spring. This change can be related to the hygroscopic growth of aerosol or the condensation of volatile components due to colder air temperature in winter. In general, the volume fine fraction is lower in Dunkerque than in Lille. For example, in summer the volume fine fraction is 52% in Lille while it is 40% in Dunkerque. This difference could indicate the impact of the maritime aerosol on the total aerosol content or a higher humidity due to the proximity of the sea shore. This difference is not observed in the ratio PM2.5/PM10. It is 0.6 for Lille and Dunkerque (Centre and Petite-Synthe) over 2007 and 2008 (Table 2.5).

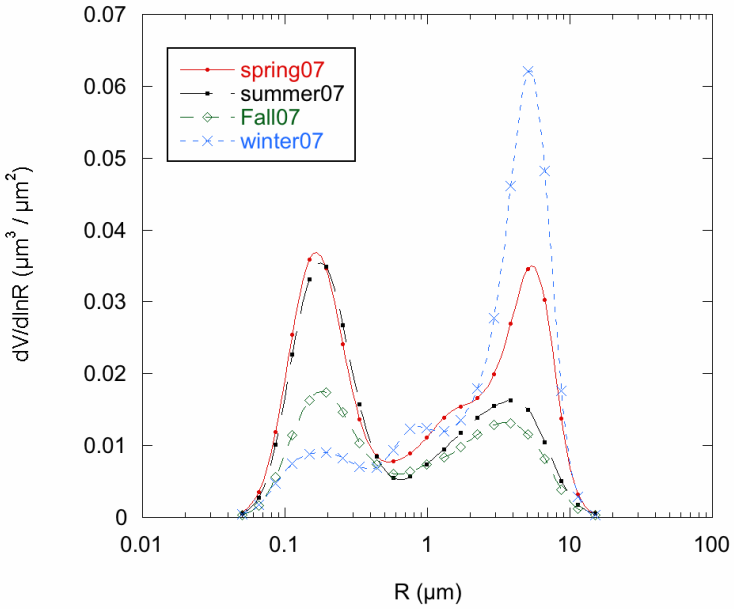

Figure 2.19 Seasonal average of Aerosol size distribution derived from sunphotometer in Lille 2007.

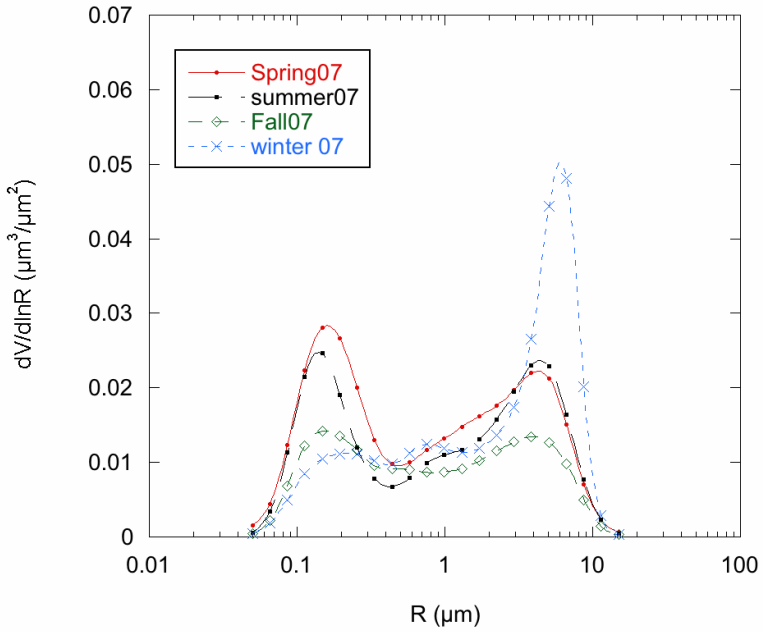

Figure 2.20 Seasonal average of Aerosol size distribution derived from sunphotometer in Dunkerque 2007.

One of the main objectives of this work is to study the relationship between AOT and PM at short time and space scale. In the following chapters, we particularly focus on the impact of the dynamic of the atmospheric boundary layer. We present 3 different field experiment focused on the time period presented in Figures 2.16, 2.17 and 2.18.

3 Impact of the mixing boundary layer on the relationship between PM2.5 and aerosol optical thickness

This chapter has been published in Atmospheric environment Boyouk et al. 2009

3.1 Introduction

Most of the pollution aerosols emitted in the atmosphere are released in the atmospheric boundary layer and then become gradually dispersed and mixed through convection and turbulence. In addition to boundary layer features (e.g. depth, turbulent flux) that are keys to understanding of the impact of aerosol on air quality, aerosol mass concentration measurements by air quality monitoring networks help to understand the dispersion of aerosols confined within the boundary layer. However, the aerosol vertical distribution and its temporal evolution are also of primary importance to understanding of changes in the aerosol mass concentrations at ground level, and to better characterize the distribution between local pollution events and large scale transport. In addition to ground-level observations, Lidar vertical soundings provide a detailed description of scattering aerosols in the atmosphere. Primary parameters derived from elastic backscattering Lidar profiles are the vertical distribution of aerosol backscattering and extinction coefficients. The vertical structure of the atmosphere can be inferred from a change in the backscattering vertical profile. Because the mixed layer has in general a higher aerosol backscattering coefficient than the free troposphere, the Lidar can also detect the boundary between the two layers (Menut et al., 1999).

The relationship between aerosol mass and optical properties depends on the chemical composition, size and shape of the particles. Many studies (Chu et al., 2003; Gupta et al., 2006 ; Kacenelenbogen et al., 2006; Liu et al., 2004 ; Pelletier et al., 2007a ; Schaap et al., 2008 ; Wang and Christopher, 2003b) have been devoted to finding the relationship between the columnar aerosol optical thickness (AOT) and the mass fraction PM2.5 or PM10. The PM data can be derived from AOT measurements using a simple linear model (Chu et al., 2003; Kacenelenbogen et al., 2006; Wang and Christopher, 2003b). However, the relationship depends on the season and on the site location. There are auxiliary parameters such as meteorological variables or the characteristics of the mixing layer that need to be accounted for (Pelletier et al., 2007a). Liu et al. (2004) and Van Donkelaar et al. (2006) improved the

capability of the multi angles imaging spectroradiometer-derived AOT in estimating surface level PM2.5 by using aerosol vertical profiles simulated by a global atmospheric chemistry model. This result suggests that the use of vertical information, namely the altitude of the mixed layer or the aerosol extinction profile can improve the determination of PM from AOT measurements. Gupta et al. (2006) highlighted the impact of the mixing height on the relationship between AOT and PM2.5. From their dataset over Texas, they found that the best correlation between PM2.5 and AOT is seen when the mixing height is between 100 and 200 m and when the relative humidity is less than 50%. However Schaap et al.(2008) did not find a significant improvement in the correlation between AOT and PM when including the Lidar-derived mixing layer height in their study in the Netherlands. However they found that the PM2.5-AOT correlation increased when the comparison time slot was centred around and on noon, which suggests that the aerosols were well mixed in the boundary layer. The relative humidity also had an impact on the AOT via an increase in the size of the particles and a change in the refractive index (Hänel, 1976). Shinozuka et al. (2007) found that the fraction of ambient AOT due to water uptake was 37 % ± 15% during their field campaign in North America. The change in aerosol scattering or extinction as a function of relative humidity can be parameterized (Kotchenruther and Hobbs, 1998 ; Raut and Chazette, 2007) but in most cases the relative humidity vertical profile and the aerosol hygroscopic properties remains unknown.

In this chapter, we present observations performed at an urban site in the North of France. The experimental site is located on the outskirt of the city of Lille, France. Lille (50.61°N, 3.14°E) is a conurbation of 1.2 million inhabitants and in the vicinity of many urban and industrial aerosol pollution sources. We present the study of a pollution event that occurred during the month of April 2007. In March and April 2007, daily PM10 concentrations often exceeded 50 $\mu g.m^{-3}$ corresponding to the European-24 hours limit that must not to be exceeded on more than 35 days per year. The pollution events were also observed by Schaap et al.(2008) at Cabauw, The Netherlands. This period was chosen according to the availability of data for all of the instruments that were used in this study. We analyze the evolution of the aerosol mass at the ground in conjunction with Lidar soundings and Sun photometer measurements. The objective is to analyze the built-up and removal of the aerosol load during the pollution event and to assess the variation in the relationship between aerosol mass at the ground and aerosol optical thickness.

3.2 Data and Methods

3.2.1 Ground-level measurement of the particulate mass concentration

During the last decades a number of epidemiological studies have shown a link between pollution by airborne particulate matter (PM) and respiratory and cardiovascular diseases either for short-term or long-term exposure (Dockery et al., 1993; Künzly et al., 2000; Pope III et al., 1995). The particle mass concentration measured at ground level is a way to evaluate the impact of aerosols on air quality. PMX means the mass concentration of particles with an aerodynamic diameter lower than X. In the present study we are using PM2.5 and PM10 data collected by a Tapering Element Oscillation Microbalance TEOM (Patashnick and Rupprecht, 1991) operated by the regional air quality network ATMO Nord-Pas de Calais. The measurement site is located downtown Lille (Faidherbe street) at less than 3 km from the Lidar site at Université des Sciences et Technologies de Lille. Comparisons of TEOM to gravimetric measurements (Allen and Ress, 1997; Van Dingenen et al., 2004) show that routine TEOMs can underestimate PM10 by up to 35%. As this TEOM is not equipped with a Filter dynamics measurement system (FDMS), we have to apply a so-called correction factor on our PM10 and PM2.5 measurements. This factor is provided by air quality network ATMO Nord-Pas de Calais, and used for PM10. The factor is derived from a systematic comparison with data acquired by two other TEOM-FDMS located in the administrative area Nord-Pas de Calais (Calais and Tourcoing). During the experimental period, the PM2.5 was not measured with the TEOM-FDMS, so the correction factor for PM2.5 remains unknown. Since May 2008, the PM2.5 is also monitored by a TEOM-FDMS. We have compared the correction factor used for PM10 and for PM2.5 for the last ten days of May 2008, corresponding to a similar meteorological situation for our observation period. Both correction factors are well correlated (R=0.95) and the PM2.5 correction factor can be derived from the PM10 one by using a linear relationship:

$$PM2.5_{corrected} = PM2.5 \times (\frac{PM10_{corrected}}{PM10} - 0.1) \times 1.25 \quad [3.1]$$

In this regression, we have only considered PM10 higher than 10µg/m^3.

3.2.2 Columnar integrated aerosol optical properties using Sun photometer

We have used the data collected by a sky-scanning ground-based automated Sun photometer (referred in the AERONET data base as Lille) belonging to the Aerosol Robotic Network (Holben et al., 1998). A full description of the instrument and the retrieval procedure can be found in Holben et al.(1998) and Dubovik et al. (2000). The primary parameter that can be derived from the Sun photometer is the aerosol optical thickness (AOT) at four wavelengths (440, 670, 870, 1020 nm) and with an absolute uncertainty of ~0.010-0.021 (Holben et al., 2001). To be coherent with the Lidar wavelength, we interpolate the AOT at 532 nm according to the Angström law and using the channels at 440 and 670 nm.

The columnar integrated volume size distribution dV/dlnr (in $\mu m^3/\mu m^2$) in range of radii between 0.05 and 15 μm is also derived from sky brightness measurements (Dubovik and King, 2000). The retrieval of particle volume size distribution was demonstrated to be adequate in practically all situations (Dubovik et al., 2002). The error in the retrieved volume density changes as a non-linear function of particle size, aerosol type and actual values of size distribution. In particular, the intermediate particle size ranges between 0.1 and 7.0 μm, the retrieval errors do not exceed 10% in the maximum of size distribution and may increase up to 35% for the points corresponding to the minimum values of size in this size range. The retrieved size distribution volume is not independent in the sense that the retrieval technique insures only the fact that the retrieved combination of all of the parameters would accurately reproduce the measured radiation field in the scope of chosen radiative transfer model.

3.2.3 Vertical profile of aerosol observed by Lidar

We have used an aerosol micropulse Lidar manufactured by CIMEL (Pelon et al., 2008). It uses a Q-switched frequency-doubled ND:YAG laser with an expanded beam (8-10 μJ with a 200 mm exit-lens diameter) and a pulse repetition frequency of 4.7 kHz. The wavelength is 532 nm. During a 10 min data acquisition sequence, 10 individual profiles are acquired and averaged. Then the system waits for 20 min before starting another acquisition sequence. The duration of a pulse is 100 ns leading to a vertical resolution of 15 m. The profiles are averaged to reduce the influence of background noise. During the day time the background noise is dominated by direct or scattered sunlight causing a sharp decrease in the signal-to-noise ratio. The background noise is estimated by taking the average of the backscatter signal

between 22 and 30 km, then subtracting it before evaluating the signal. The data processing includes the correction of the spurious signal due to the detection of the scattered light in the receiver, called the afterpulse signal and the correction of the overlap function (Pelon et al., 2008). The Lidar backscatter signals are calibrated for a reference altitude in which the particle backscatter coefficient is negligible compared to the known molecular backscatter. In this study the reference altitude is between 4 ~ 4.5 km on cloud-free days. Because of the after pulse the attenuated backscatter coefficients are not useful between 0 and 225 m.

We compute the aerosol extinction and backscatter coefficient using the Klett method (Klett, 1981) that requires a given Lidar ratio. Using Raman Lidar, *Ansmann and Müller* (2005) have given a range of Lidar ratio between 35 and 70 sr at 532 nm for less absorbing urban aerosols (Ansmann et al., 2001; Franke et al., 2001). The Lidar ratio can be estimated using the aerosol scattering phase function and single scattering albedo derived from the Sun photometer using:

$$L_{aer} = \frac{4\pi}{\omega_0 P(180)} \qquad [3.2]$$

Where ω_0 is the single scattering albedo and P(180) is the backscattering phase function. Using this approach, *Cattral et al.* (2005a) have estimated that the Lidar ratio for urban/industrial pollution is 71 sr. Lidar ratio value is obtained by linear interpolation at 532 nm of AERONET retrieved phase function and single scattering albedo between 675 nm and 440 nm. We have estimated an average Lidar ratio for the site of Lille of 67 sr with a standard deviation of ± 11 sr using 23 retrievals. This average value has been used throughout this study for determining the extinction coefficient.

The use of Lidar data to detect the mixed layer top height or entrainment zone thickness has been widely investigated (Baars et al., 2008; Flamant et al., 1997; Lammert and Bösenberg, 2006 ; Menut et al., 1999 ; Seibert et al., 2000). The top of the mixed boundary layer (MBL) is detected using the modulus (absolute) of the minimum of the first derivative of the range corrected signal (Flamant et al., 1997). Indeed, a decrease in the range corrected Lidar signal is observed in the transition zone between the aerosol loaded boundary layer and the free troposphere. We have then determined the altitude of the boundary layer by using a simple gradient method applied to the Lidar profiles acquired during the day and night at a time resolution of 30 min.

3.2.4 Retrieval of ground-level PM2.5 from Lidar and Sun photometer observations

We have explored the relationship between the ground-level aerosol mass concentration and the optical measurements acquired by the Lidar and the Sun photometer using three different methods based on a simple correlation analysis. First, the range corrected attenuated backscattered Lidar signal $S(z_l)$ at the lowest available altitude can be used to infer the mass concentration close to the ground. The Lidar signal is not available in the first hundred meters because of the afterpulse effect. We have estimated that the first level that can be used is at z_l = 240 m.

Secondly, we have compared the Sun photometer AOT with PM2.5. The relationship between columnar AOT and ground-level PM2.5 is not straightforward and depends on the vertical distribution and the optical, size distribution and hygroscopic properties of the aerosol. Under the basic assumption that the aerosol mass is well mixed in the boundary layer and that the relative humidity has a negligible impact on the extinction coefficient, we have computed the Sun Photometer derived PM2.5 using :

$$PM2.5_{AOT}^{Aeronet} = \frac{\tau}{\sigma^* H_{BL}} R_{BL} \qquad [3.3]$$

Where τ is the AOT derived from Sun photometer data, H_{BL} the MBL top and R_{BL} the Lidar derived AOT ratio between the boundary layer and the total column. σ^* is the specific mass extinction coefficient (Hand and Malm, 2007).We took a value of 4.75m^2/g that is justified *a posteriori* to get a regression slope as close as possible to one. We have tested one after the other the impact of using H_{BL} and R_{BL}. At last, we have considered the Sun photometer derived fine mode volume fraction as a better proxy for the PM2.5. We define $V_{1\mu m}$ the fine mode volume as

$$V_{1\mu m} = \int_{0.05\mu m}^{1\mu m} \frac{dV(r)}{d\ln r}\, d\ln r \qquad [3.4]$$

The Sun photometer derived PM2.5 is then obtained given the following equation:

$$PM2.5_{Volume}^{AERONET} = \frac{\rho V_{1\mu m}}{H_{BL}} \qquad [3.5]$$

ρ is the density of dry aerosol and we took ρ = 1.7 g/cm^3 (Sloane, 1984). During the observation period, the fine mode dominates the size distribution and have the major contribution to the AOT . Figure 3.1 shows that the fine mode volume fraction is well correlated with the total AOT as opposite to the total volume fraction. This latter parameter is not considered in the following of the study as it is poorly correlated with the ground-level PM2.5.

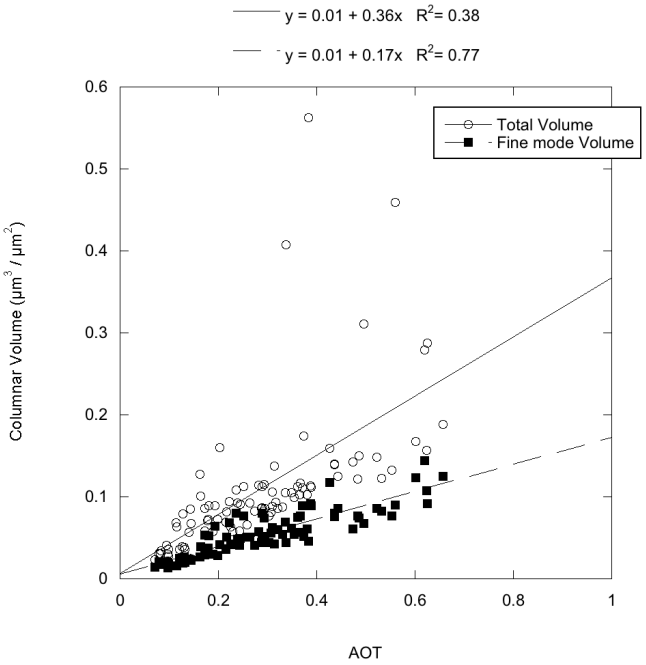

Figure 3.1 Comparison between aerosol optical thickness and total and fine volume fraction (columnar integrated) derived from Sun photometer.

The errors and uncertainties are due to the inversion method used, calibration of the instruments and the difference in the time and space location of the different measurements. This latter error is probably the largest but remains extremely difficult to quantify. Using the first available level of the Lidar signal, the error in estimating ground-level PM2.5 is proportional to the error in the Lidar backscattered signal in the first hundred meters. Due to the overlap function, Pelon et al. (2008) have estimated that error in the Lidar backscattered signal is ± 10% above 600 m and can be up ± 50% when the signal is extrapolated down to

ground level. An additional source of error comes from the impact of the relative humidity on the aerosol optical properties. This impact can be modeled (Hänel, 1976) when the aerosol type (hygroscopic factor) and the vertical profile of relative humidity are known (Raut and Chazette, 2008). Since we have the relative humidity measured at the ground, we have only applied a correction factor for the Lidar signal by defining a corrected signal $S^*(z_l)$:

$$S^*(z_l) = S(z_l) * (1 - RH)^{0.55} \quad [3.6]$$

where RH is the relative humidity and z_l is the lowest valuable level. Eq. 6 stems from a modeling of the scattering cross section and size growth factor due to water uptake (Hänel, 1976; Jeong, 2007; Kotchenruther and Hobbs, 1998). This equation is only applied here at the lowest level of the Lidar measurements (zl=240 m). Within such a short range, the Lidar signal is proportional to the Lidar backscattering at the first order so the dependence of the scattering cross section with relative humidity (depicted in Hänel, 1976) is well appropriate. The exponent factor 0.55 has been chosen by optimizing the final correlation factor between the Lidar retrieved PM2.5 and ground PM2.5 measurements, and is found to be close to the value in Raut and Chazette (2007). The overall uncertainty is between 20 and 40%.

In equation (3), the error in the retrieved mass is proportional to the error in τ, H_{BL}, R_{BL}, and σ^*. Calibration accuracy causes instrumental error of 0.01 in τ which is in the order of 5 to 10% of optical thickness for $\tau_{aer}(440) \leq 0.2$. The estimation of H_{BL} was manually checked and the relative error was ~5%. R_{BL} uncertainty depends on the error in the retrieved extinction profiles, which depends on the choice of the Lidar ratio. Considering the Lidar ratio variability given in paragraph 2, we have estimated the uncertainty of R_{BL} to be 30-40%. However, as we use a constant Lidar ratio, this error can be larger. As we have used a constant value for σ^*, a change in the aerosol type will introduce significant error to the estimation. However, we consider a relatively short period of time (less than 1 month) which was dominated by fine pollution particles and we have estimated the error to be ~10%, the same as the error in the density. Considering equation (5),it can be seen that the use of the fine mode aerosol volume fraction introduces an error due to its retrieval of ~15% (Dubovik et al., 2000). However, the error can be much larger (up to 100%) when the coarse mode dominates the size distribution, which is not the case during our observation period.

3.3 Results

3.3.1 Evolution of aerosol mass, optical thickness and mixed boundary layer height

Figure 3.2 shows the daily average variation of PM2.5 and AOT during April 2007. We can observe a sharp increase in AOT and PM2.5 between 7 and 13 April and a second increase between 25 and 28 April. Our Lidar data set begins on April 13, 2007. The daily average PM2.5 value starts from less than 18 µg/m^3 on April 7 and reaches 62µg/m^3 on April 13.

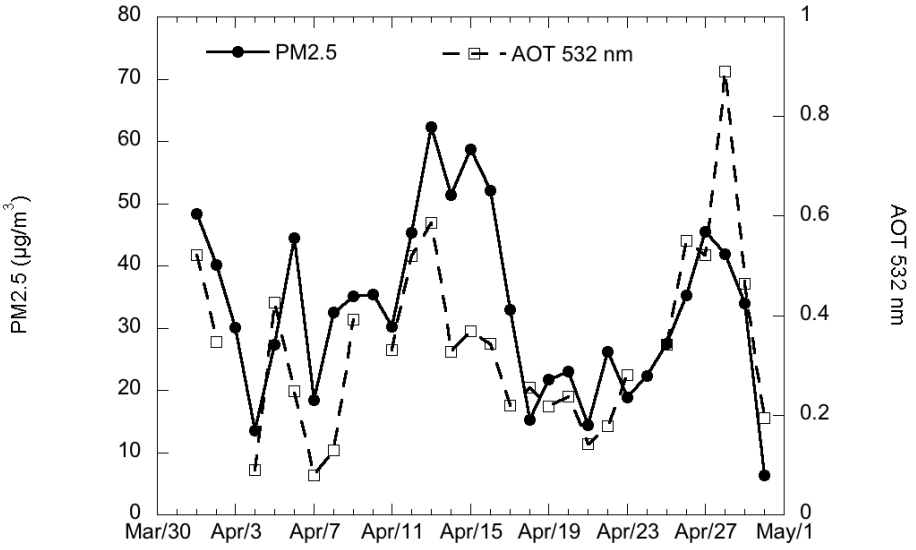

Figure 3.2 Daily average of PM2.5 and aerosol optical thickness measurement during April 2007 in Lille. The PM2.5 data have been corrected according to the described method in section 3.2.1.

The AOT changes from 0.1 to 0.6 in the same time. From the 18 to the 25 April, the daily average PM2.5 is between 15 and 22 µg/m^3 and on average the AOT is 0.3. A second increase is observed at the end of the month with a maximum in PM2.5 on 27 April (45 µg/m^3) and a corresponding daily average AOT of 0.5. The maximum in AOT is reached on 28 April. We have based our study on the hourly data and we have selected the hours for which all the necessary data (Lidar profiles, Sun photometer inversions and PM2.5 measurements) were available. The Lidar system was stopped between 12 April 07:00 and 13

April 07:00 UTC for maintenance so we considered the Lidar data since 13 April. The data set includes measurements acquired on April 14 to 22 and on April 26, 27 and 30.

During the observation period, a ridge of high pressure dominates over Europe until mid-April and is then slightly perturbed by northern and eastern low-pressure areas. This scheme ensures a fine weather with clear skies over the region before April 17 and some elevated clouds after, which are well detected in the Lidar profiles. Temperature time series show respectively a clear diurnal cycle from 10 to 25°C and from 5 to 15°C before and after 17 April. Northerly air masses during this period are characterized by a low wind speed (<5 m/s) at the ground level, mainly driven by turbulent momentum transfer. The MBL development is then systematically associated with an increase in wind speed in the morning, which highlights the turbulent activity. Solar radiation ranges from 550 W/m^2 (cloudy days) to 750 W/m^2 (clear sky) in the area. Such wind speed and solar radiation ensure a highly or moderately unstable atmosphere during convective periods, according to the Pasquill classification. The MBL dynamics retrieved from Lidar signal fit well with humidity and wind time series. This analysis particularly shows that fog is a major local phenomenon before 17 April and after 25 April, which delays the boundary layer development by a few hours. This feature is illustrated on figure 3 showing the diurnal development of the MBL (between 8:00 and 18:00 UTC) for 15 and 21 April.

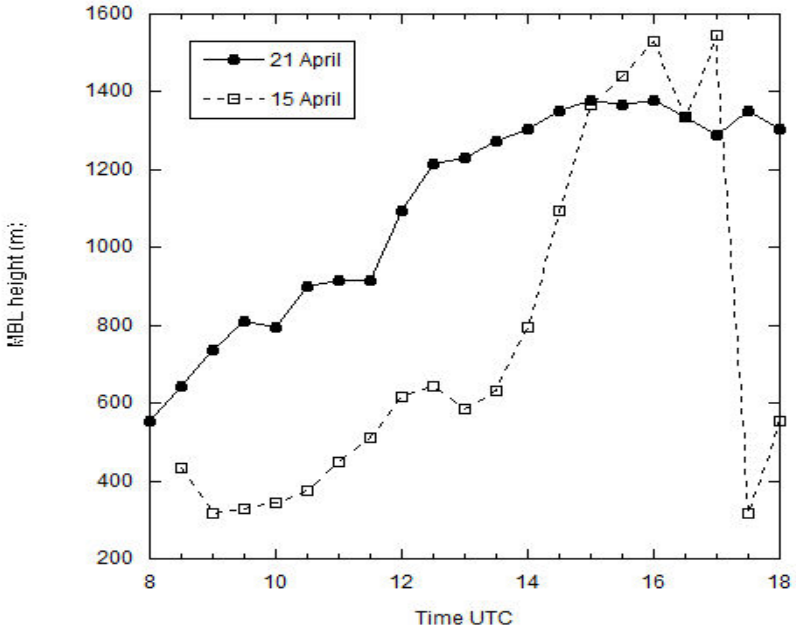

Figure 3.3 Top altitude of mixed boundary layer for 15 April and 21 April with time step of 30 min

The complete daily cycle of the MBL height is illustrated on Figure 3.4 along with the variation of the logarithm of the range corrected attenuated backscattering coefficient between 15 and 16 of April and between 21 and 22 April, 2007. The panels illustrate the diurnal variability in the vertical structure of the atmosphere. We can observe significantly higher value of the backscattering coefficient close to the ground level during the first period (Figure 3.4 top). The white color shows missing data on April 15 in the early morning due to condensation of water on the optical system. The urban boundary layer has a complicated three-dimensional structure which is difficult to describe comprehensively. Fine resolution of time- height Lidar data is useful to reveal the daily cycle of convective boundary layer growth and collapse. The mixing layer height depends on the meteorological conditions and other primary factors: wind speed and buoyant forcing (convection) due to solar heating of the surface (Stull, 1988). On 15 April (Figure 3.4 top), we can observe three different aerosol layers between 9:00 and 15:00 UTC. The bottom layer corresponds to the mixed boundary layer (black dots) that increases in height in the morning and the early afternoon and collapse in the late afternoon (17:00-18:00 UTC) to form the nocturnal boundary layer (also observed on 16 April). The residual layer is observed in the morning and during the night with a top

height at 1.3-1.4 km. During the period of low PM2.5 and AOT (21-22 April, see Figure 3.4 b), the MBL height diurnal cycle is clearly smoother.

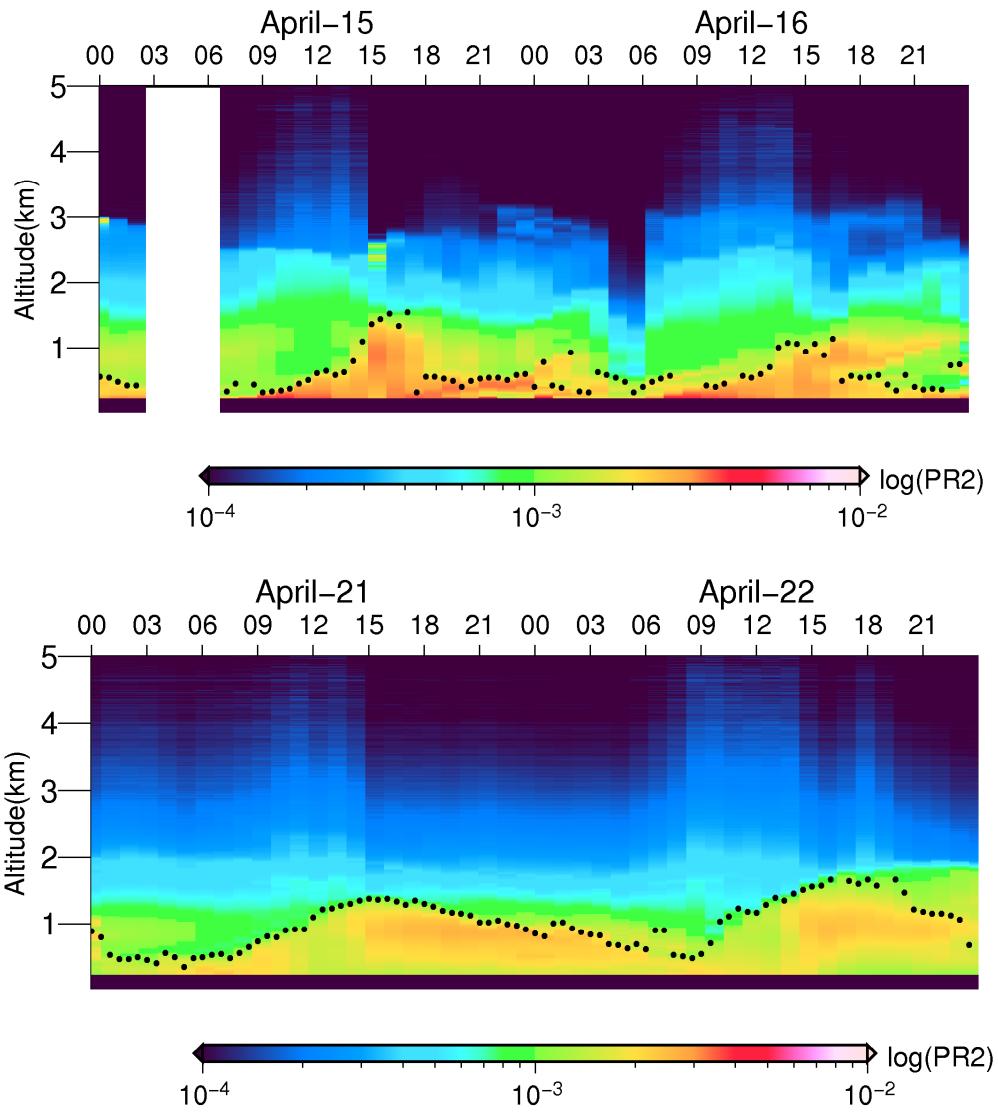

Figure 3.4 Logarithm of the range corrected Lidar signal for (top) April 15 to 16 and for (bottom) April 21 to 22 2007. The time step is 30 min. The black dots are located at the top of the mixed boundary layer.

During the build-up of the pollution event, the wind direction at the ground level is North-East. Air mass back-trajectories (Figure 3.5) computed for 13 April confirms the eastward continental origin of the air mass. The wind direction moved to the North and North-West

after 13 April bringing air mass from the North Sea. Figure 3.5 gives an example of the LRT during a pollution episode observed in Lille during April 2007 . The 7-day back-trajectories have been calculated using the HYSPLIT 4 model with specifying the altitudes of boundary layer and higher and upper altitudes in the trajectory model. We have observed the transport from the northwest marine area and it changes to east at (12:00 UTC) on 13 April during the pollution episode. Later days, the direction of plume is changing from west to northwest in lower altitude and north for higher altitude. The back-trajectories help explain the long life of the plume.

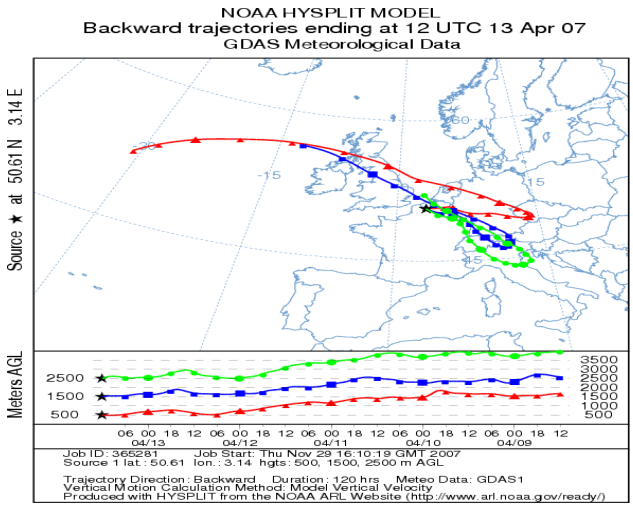

Figure 3.5 7 days backward trajectories on 13 April 2007

We can also observe an aloft layer up to 3 km during the beginning and the end of the observation period that disappears during the period of low PM2.5 and AOT. This feature is presented in Figure 3.6 which shows the retrieval of the aerosol extinction coefficient on 15 and 21 of April at 16:00 UTC and 26 at 17:00 UTC. This aloft layer appears after 17:00 UTC on April 13, 5 hours after the maximum aerosol concentration measured at ground level. The presence of the aloft layer affects the AOT ratio between the MBL and the total column, R_{BL}. It is 44.6% on 15 April, 72.8% on 21 April and 33.1% on 26 April, 2007.

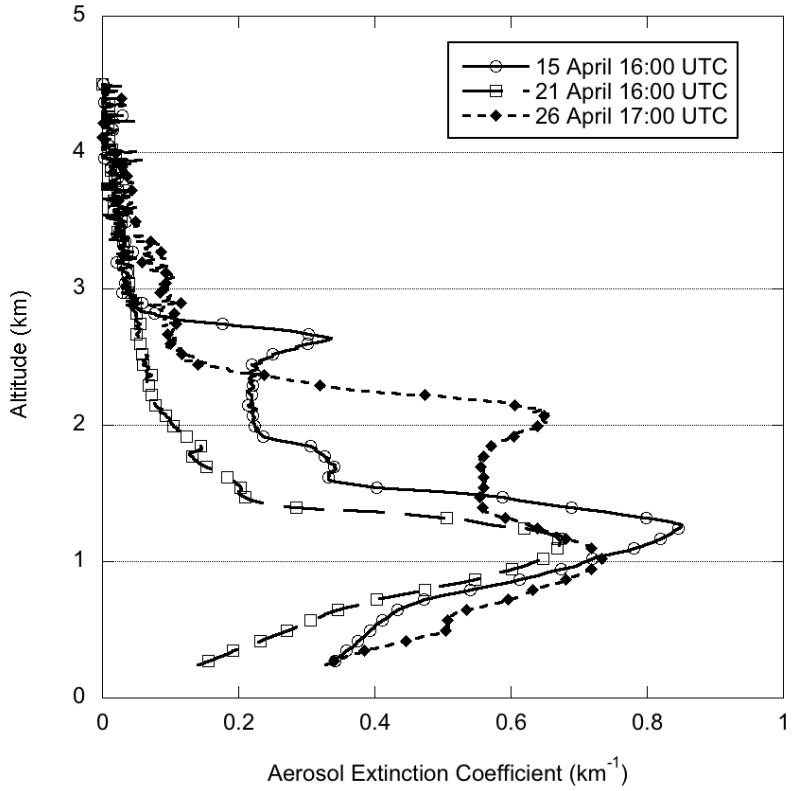

Figure 3.6 Vertical profile of aerosol extinction coefficient at 532 nm on April 15 and 21 at, 2007 at 16:00 UTC and April 26, 2007 at 17:00 UTC.

3.3.2 Retrieval of ground-level PM2.5

Comparison between ground-level PM2.5 and retrieved PM2.5 has been shown on Figure 3.7 According our methods we have used the fine volume fraction (V-H) or the AOT (AOT-H) corrected for the MBL height, and the Lidar signal at 240m (S-RH) corrected for relative humidity effect. The figure 3.7 shows the relationship between the retrieved PM2.5 using the volume of fine fraction which is corrected by the height of the boundary layer H_{BL} in red color. And we have found the correlation coefficient of 0.81 whereas this correlation is improved using the AOT corrected by H_{BL} to a value of 0.85.

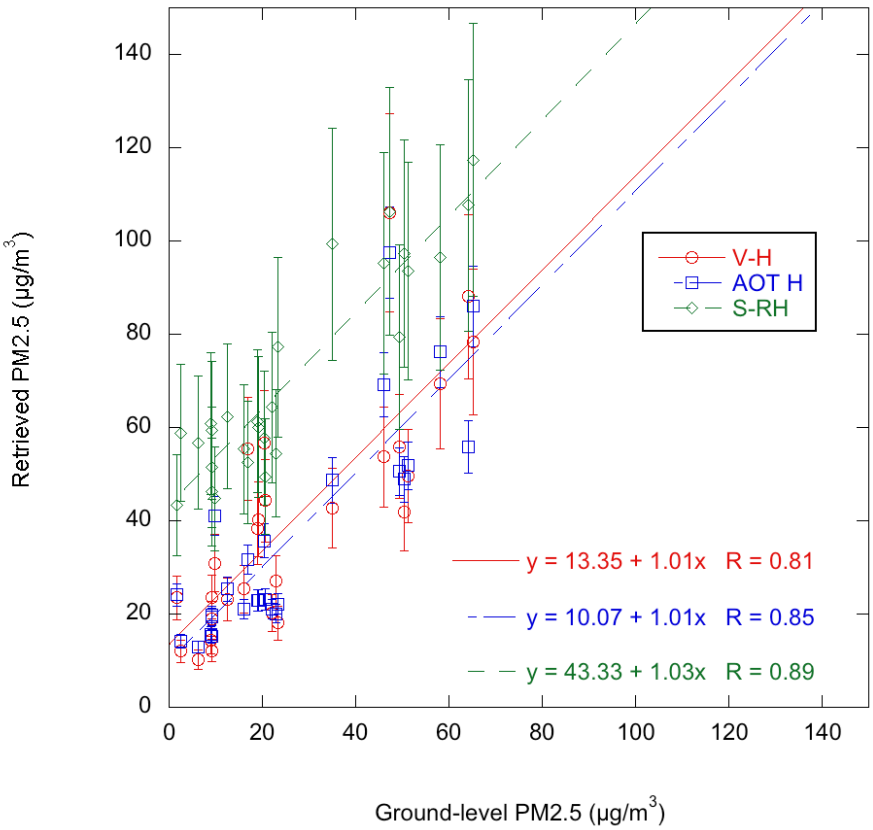

Figure 3.7 Comparison between ground-level PM2.5 and retrieved PM2.5 using the fine volume fraction (V-H) or the AOT (AOT-H) corrected for the MBL height, and the low level Lidar signal (S-RH) corrected for relative humidity effect**.**

The results of the comparison is summarised in Table 3.1. The Lidar signal in the lowest level is well correlated with the ground-level PM2.5. The regression is adjusted to have a slope close to 1. The correction for relative humidity impact increases the correlation (R^2 = 0.84). The total AOT is also correlated to ground-level PM2.5. There is a significant improvement in the relationship (correlation, regression coefficient and RMSE) when the MBL height is accounted for. However, we cannot observe any improvement when we consider the AOT ratio between the MBL and the total column. The uncertainty of this parameter remains high because it depends on the Lidar ratio vertical profile. Moreover, there is a clear impact of the relative humidity profile in the MBL that is not currently accounted for. Using the fine mode volume fraction instead of total AOT does not significantly improve the relationship. The AOT is

directly measured with excellent accuracy, whilst accuracy of the fine volume fraction retrieval primarily depends on AOT and contributions from the coarse mode. Considering the use of AOT and MBL height, the remaining offset is ~12µg/m^3. This offset can be attributed to the distance gap between the ground station and the Sun photometer which is crucial when considering low AOT and mass concentration. Moreover, equation (1) is not valid for low aerosol concentration that may correspond to situation with a significant contribution from volatile compounds.

Table 3.1: Summary of the correlation study between ground level PM2.5 and the Lidar signal (S) at 240 m, the Lidar signal at 240 m with a correction for relative humidity impact (S-RH), the aerosol optical thickness (AOT), the AOT and the MBL height (AOT-H_{BL}), the AOT, MBL height and ratio of MBL AOT to total AOT, (AOT-HBL-RBL), and the fine mode volume fraction and MBL height (Vol-HBL). The uncertainties on the parameters derived from a least squared fit to a straight line model are given within the brackets.

	R^2	R	RMSE	Slope	intercept
S	0.80	0.89	10	1.0 (0.1)	34 (3)
S-RH	0.84	0.92	9	1.0 (0.1)	42 (3)
AOT	0.61	0.78	16	1.0 (0.2)	22 (5)
AOT-H_{BL}	0.73	0.85	12	1.0 (0.1)	10 (4)
AOT-H_{BL}–R_{BL}	0.56	0.75	15	0.8 (0.1)	28 (5)
Vol-H_{BL}	0.65	0.81	15	1.0 (0.1)	13 (5)

Conclusion

We have performed ground-based measurements in the North of France (Lille, 50.61°N, 3.14°E) to analyze the relationship between the aerosol optical thickness and the mass concentration at the ground. A set of backscattering Lidar soundings, ground-level aerosol mass concentration along with Sun photometer observations were acquired during the month of April 2007. During this period, the aerosol mass concentrations were highly variable with AOT between 0.11 and 0.66 (at 532 nm) and PM2.5 between 2 and 65 µg/m^3. Lidar analysis reveals also a large variability in the MBL height diurnal cycle and in the aerosol extinction

vertical distribution. The Lidar backscattering coefficient at the lowest possible level is well correlated to the ground-level PM2.5. When considering the total aerosol optical thickness, we obtain a fairly good estimate of the PM2.5 at the ground-level under the assumption that the MBL height is known. As the AOT is the primary parameter derived from aerosol satellite measurements (King et al., 1999), the relationship between AOT and ground-level mass concentration has a crucial importance for the monitoring of aerosol pollution from space. Using the Sun photometer retrieved aerosol fine mode volume concentration did not improve the correlation with PM2.5. Moreover we did not improve this relationship by using the AOT ratio between the MBL and the total column. However this parameter depends on the Lidar ratio profile that cannot be determined using a single wavelength backscatter Lidar. The proposed approach will benefit from additional observations including different aerosol types and meteorological situations. Further improvements on the overall accuracy of the method are also expected from a dedicated aerosol optical properties joint retrieval between combined Sun photometer and Lidar observations.

4 Winter study of aerosol pollution and classification of relationship between aerosol optical thickness and particulate matter in Dunkerque, France

This chapter has been presented to the Earthcare workshop (Boyouk et al. 2009)

4.1 Introduction

The air quality in cities varies depending on the industrialization, population and traffic density, and meteorological and topographical properties of the region. The pollutants exhausted, emitted and discharged by the industrial foundations have the most significant effect in environmental pollution. By increasing industrialization and energy consumption, there is a rapid increase in pollution level which seriously threatens the human health (Mayer, 1999). Among the many pollutants highlighted for adverse health effect, particular attention has been focused on fine particulates (Dockery and Pope, 1994 ; Schwartz, 2003). Atmospheric particulate matter (PM) is made up of a mixture of solid and aqueous species which enter the atmosphere by anthropogenic and natural pathways. In addition to the local and regional anthropogenic particulate emissions, both the levels and composition of ambient air particle matter depends on the climatology (temperature, humidity, radiation, rain scavenging potential, re-circulation of air masses vs. dispersive conditions) and on the geography (topography, soil cover, proximity to arid zones or to the coast) of a given region (Querol et al., 2004). Among the meteorological parameters, wind speed can be effective in decreasing pollutant concentration. For example, Romero et al. (1999) investigated the air pollution levels in various regions of Santiago and determined that in some regions wind decreases the pollution.

In addition the temporal and spatial changes of aerosol optical properties in urban environment can be well associated with the air quality and meteorological condition. Many studies (see Hoff and Christopher (2009) for a review) have applied different methods and models to find the relationship between aerosol optical thickness (AOT) and PM2.5 or PM10. The AOT is function of optical and columnar properties of aerosol. The linear model could not explain well the relationship but can be improved with application of some conditions on auxiliary parameters, mainly meteorological variables (Gupta and Christopher, 2009 ; Pelletier et al., 2007b). The prediction of PM2.5 from AOT is on the order of ±30% (Hoff and Christopher, 2009).

The characteristic of mixing layer affects the slope of this relationship. Boyouk et al. (2009) have shown that the correlation between AOT-derived and measured PM2.5 is significantly improved when considering the mixed boundary layer height derived from Lidar observation. Schaap et al. (2008) also improved AOT and PM2.5 relationship by using Lidar observations for improving cloud screening in the AOT data. However they concluded that the AOT and PM2.5 relationship was shown to be insensitive to inclusion of the mixed layer height in their observation in the Netherlands. The altitude of the mixing boundary layer is particularly crucial during wintertime when a strong inversion traps the pollutants close to the ground.

Our aim is to investigate the relationship between PM2.5 and AOT during wintertime. The methods have been evaluated on the period of winter 2007 and 2008 in the industrial - urban-marine area of Dunkerque. Combination of ground based measurement of PM2.5, Sun photometer and Lidar helps us to analyse impact of the regional transport on local aerosol pollution.

4.2 Geography, sites location and meteorological condition during campaign

4.2.1 Location

Dunkerque (51°04′N; 2°38′E) is a city located on the southern coast of the North-Sea. The combined measurement of Sun photometer, particle mass concentration, meteorological parameters and Lidar backscatter signal have been used in our study from December 2007 to February 2008. Particle mass and other chemical pollutant concentrations are measured by automatic stations (Atmo Nord-Pas De Calais http:// www.atmo-npdc.fr) in Petite-Synthe (PS, urban station) and Dunkerque center (DC, traffic station close to MREI). The PS station is located approximately 5 km south-west from DC station. Figure 4.1 shows the main industrial sites, measurement points, motorways and major roads. The Sun photometer (AERONET instrument: http:// www.AERONET.gsfc.nasa.gov) and the Lidar are situated in MG.

Figure 4.1 Dunkerque- Main industrial sites; Measurement point, Main road, industrial area. DC is labelled Dunkerque. PS is Petite –Synthe. Lidar and sun photometer are near to MG.

4.2.2 Meteorology

Meteorology has high influence on air quality, transport of aerosol pollution and formation of primary and secondary aerosols, and their ultimate removal from the atmosphere. This variability of pollutant concentrations and the resulting clean and polluted days in an area with more or less constant emissions are determined by meteorology parameter like wind speed and wind direction and turbulence intensity. The hourly average of wind parameters (direction and speed) for three months of study (December 2007, January and February 2008) are presented in Figure 4.2 near DC station. In this region the air masses are influenced by the dominant winds blowing from South West and South with a maximum averaged of 5.5 m/s during winter. Anticyclone and low pressure conditions with a highest variation of temperature of 4° deg are observed in February (Figures are not presented). These conditions result in a high variability of the wind speed, wind direction and atmospheric stability.

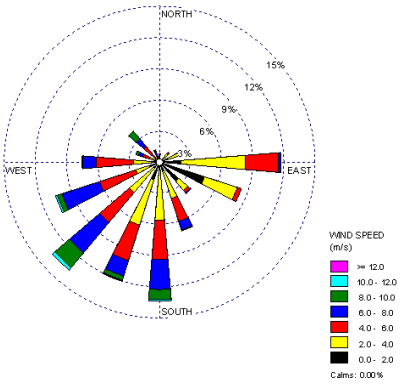

December 2007, January 2008 and February 2008

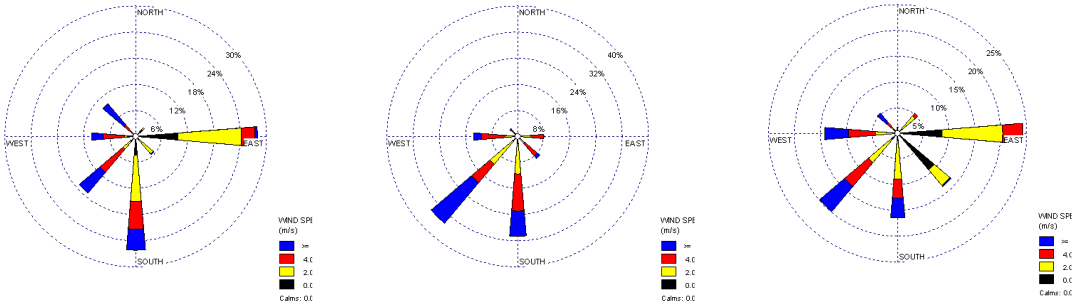

December 2007 January 2008 February 2008

Figure 4.2: Hourly average of wind component for the whole period of observations (top) and each month (bottom) (black- 0~2 m/s, yellow-2~4m/s, red-4~6m/s and blue >6m/s.

4.3 Observation and measurements of PM mass concentration and AOT

PMX means the particles with an aerodynamic diameter lower than X µm. The PMX measurement of two automatic stations (PS and DC) has been used. The PS station is at a very short distance from road of a high density traffic street. The station did not cover all of the emission sources and we have used the measurement of DC station of PM. The PM2.5 and PM10 have been measured by TEOM instrument and they have been corrected from volatile component. The correction factor used for PM10 and for PM2.5 is the same. The columnar aerosol optical depth and size information have been obtained from AERONET

network measurement. In this chapter only level 1.5 data are used during daytime and cloud free conditions.

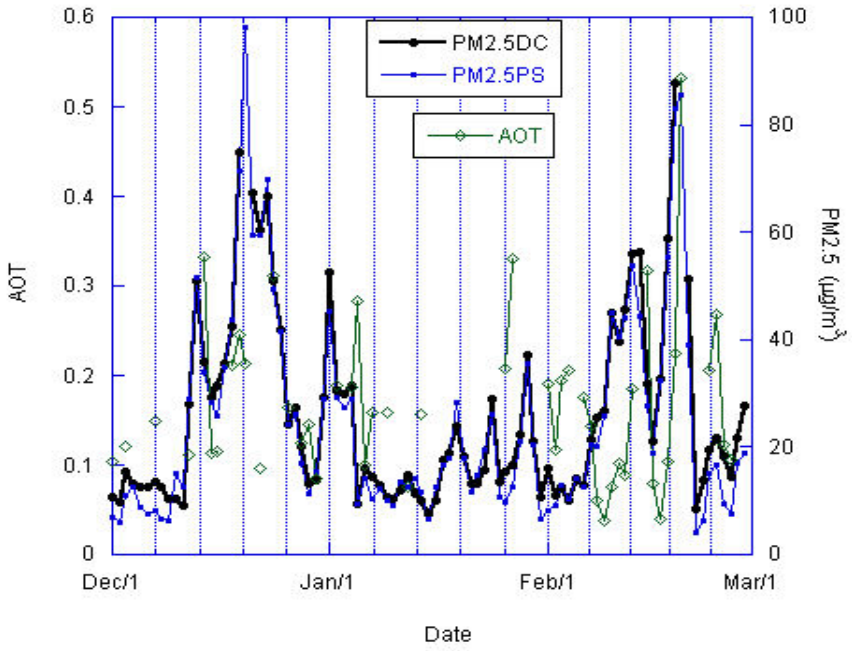

Figure 4.3 Temporal variation of the daily average of PM2.5 and AOT (532) in DC and PS Dec 2007 to Feb 2008

Figure 4.3 shows the daily average of PM2.5 and AOT during December 2007, January and February 2008 in DC and PS. The measured PM2.5 concentrations shown in the Figure 4.3 vary by a factor of less than 10 from day to day. The figure shows PM2.5 and AOT have the same trend over this period. It is observed 18 daily average measurements of PM2.5 above 40 μgm^{-3} corresponding to the "unhealthy condition for special group" category according to the US Environment Protection Agency (USEPA) and 38 times with PM2.5 in the "moderate condition" category (between 15 and 40 μgm^{-3}). The monthly mean AOT is 0.17 in December 2007, 0.18 and 0.16 in January and February 2008, respectively. The corresponding monthly mean PM2.5 is 42, 33 and 45 μgm^{-3} in December, January and February. Indeed, it has been observed two high pollution episodes due to long range transport which have been started on 14 December and 16 February. The highest hourly mean AOT observed in December, January and February are respectively 0.35, 0.39 and 0.61. The

corresponding hourly mean PM2.5 and PM10 are 38 and 43 μgm^{-3} in December, 19 and 31 μgm^{-3} in January and 101 and 160 μgm^{-3} in February.

Figure 4.4 shows the rose wind of hourly average of PM2.5 and PM10 addressed to wind direction. Here the PM2.5 limited value of 15 and 40 $\mu g/m^3$ for moderate and unhealthy condition is chosen for interval. The values of 40, 80 and 100 $\mu g/m^3$ are labeled for PM10. The PM rose wind shows that PM values above $40\mu g/m^3$ can be observed in special directions reproductible from month to month in the section between east and south in December, January and February. But in January and February there are some sources from south west. Considering wind direction both chemical industries and vehicular traffic may be considered responsible for the pollution in Dunkerque (Figure 4.4).

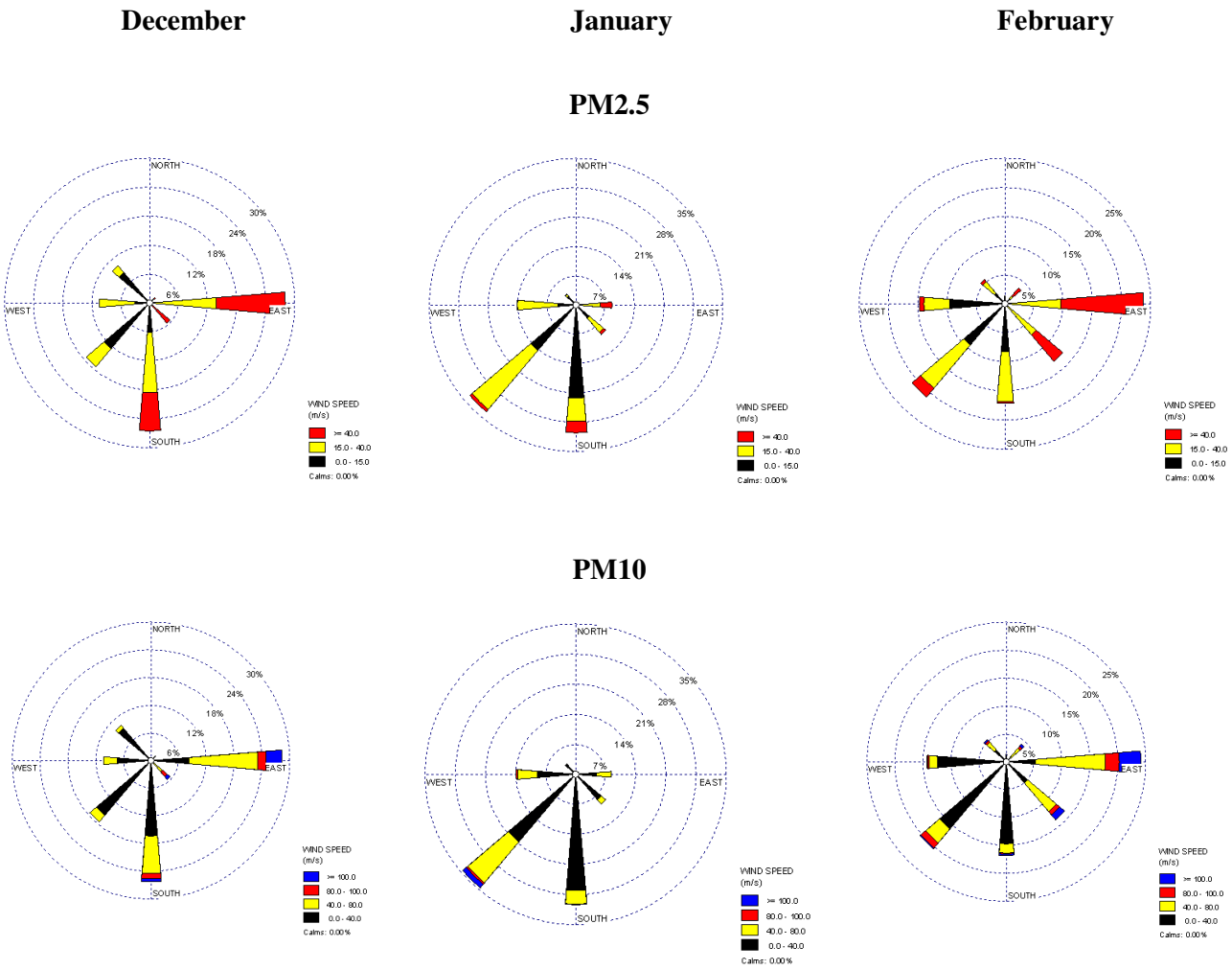

Figure 4.4 Wind rose of PM2.5 (top) (black- 0~15 µg/m^3, yellow-15~40 µg/m^3, red>40 µg/m^3 and PM10 (bottom) Dec. 2007, Jan. and Feb. 2008 at DC station (black- 0~40 µg/m^3, yellow-40~80 µg/m^3, red-80~100 µg/m^3 and blue >100 µg/m^3.

We have used hourly average of AOT and PM2.5. Figure 4.5 shows the comparison between AOT and PM2.5 for the whole period between December 2007 and February 2008. The AOT and PM2.5 have been correlated with a correlation coefficient R=0.36. The AOT and PM2.5 relationship may be categorized by observing, in Figure 4.5, the values of PM2.5 and AOT.

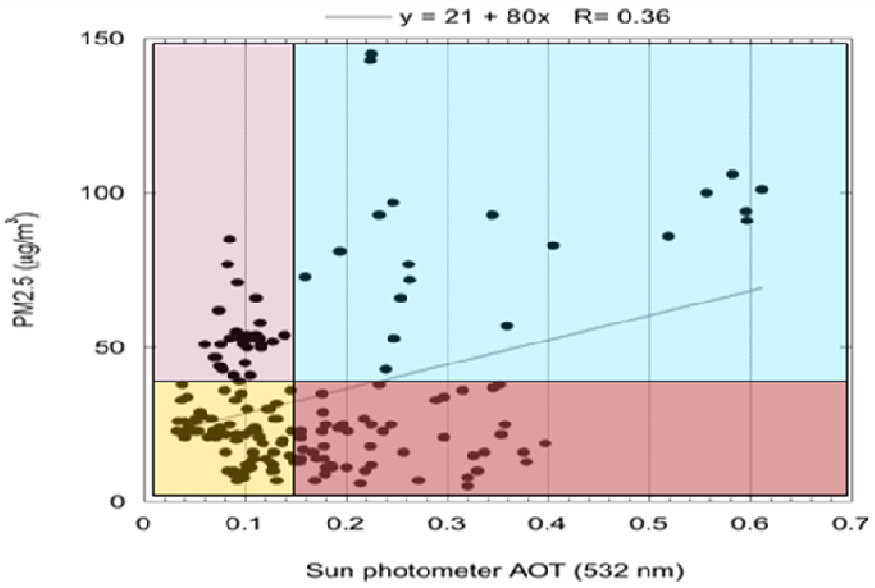

Figure 4.5 Comparison between AOT and PM2.5 using hourly measurements between Dec 2007 and Feb 2008 in Dunkerque, France.

4.3.1 Classification

The mean value of hourly average of AOT is 0.16 and we have used this value as a threshold. We consider a PM2.5 limit value of 40µg/m^3 as threshold. From 172 hourly measurements 19 cases are in the condition with AOT > 0.16 and PM2.5 > 40 µg/m^3, whereas AOT > 0.16 and PM2.5 < 40 µg/m^3 contains 45 observations. AOT < 0.16 and PM2.5 > 40 µg/m^3 represents 30 observations. The majority is for AOT < 0.16 and PM2.5 < 40 µg/m^3 with 78 points. In this method we are more interested to understand the reason why it is observed low value of AOT corresponding to high value of PM2.5 and the importance of the vertical profile. We have made four groups using the mean value of AOT and PM2.5 hourly average data. The average of meteorological and PM measurements of four groups have been shown in Table 4.1. The AOT is influenced by the long range transport of pollution aerosols, while the ground-level PM2.5 is more directly influenced by local pollution. The group 1 (AOT < 0.16 and PM2.5 < 40 µg/m^3) corresponds to the case when we have low local pollution and no long range transport of aerosols. The group 2 (AOT > 0.16 and PM2.5 > 40 µg/m^3) is the case where the long range transport and local emission influence both the AOT and PM2.5 concentrations. This situation can be explained by stable

weather conditions, calm winds, subsidence caused by high pressure system and hence suppression of vertical motions and accumulation of aerosols near the ground.

The group 3 (AOT > 0.16 and PM2.5 < 40 µg/m^3) could correspond to situations where the long range transport does not impact the ground-level concentrations or can be due to cloud contamination. In the group 4 (AOT < 0.16 and PM2.5 > 40 µg/m^3) when the boundary layer is shallow leads to high ground-level PM2.5 but low AOT. High PM2.5 and variable AOT means that boundary layer aerosol is somehow decoupled from free troposphere aerosol, meaning that as the long-range transport usually occurs in the free troposphere, it is observed by the Sun photometer but not TEOM. If there is no process which mix the aerosols down from free troposphere into the boundary layer then the free troposphere is decoupled from boundary layer. A high pressure system moved over the measuring site. The subsidence acts as a cover and suppresses vertical mixing. Therefore it can be expected that the aerosol concentration accumulates near the ground. Recirculation contributes a lot to the high boundary layer aerosol concentration. Recirculation means that the air is not renewed and stays more or less stable over a certain region. Then the emission of aerosols increases the aerosol concentration and removal processes do not work efficiently.

In the group 1 the wind direction is mostly South and it shows the condition with lowest amount of pollution from highways and industry around the site. The mean value of PM2.5/PM10 is 62% whereas the ratio of volume concentration of fine particle to total volume is 40%. The comparison between group 2 and 3 shows interesting features. First the wind is blowing from South-East in group 2 while it is from South-West in group 3. We can also observe that in group 2, the PM2.5/PM10 ratio and the fine mode fraction are close to 75%. While in the group 3, the fine mode fraction is 75% and the PM2.5/PM10 ratio is 55%. Moreover, the PM2.5 difference observed between the DC and PS stations (in relative number to the DC station concentration) is 30% in group 2 and 11% in group 3. It is in agreement with a higher wind speed in group 3 (5 m/s) than in group 2 (2 ms/s) leading to mixing of pollutants over a wide area. In group 4 the wind direction is the same as for group 2 corresponding to high PM concentrations. The wind speed is also very low. The fine mode fraction differs significantly between group 2 (75%) and group 4 (50%). The difference between the two ground-level PM2.5 stations is also higher for group 2 than group 4.

When we focus on the most problematic groups (3 and 4) we can conclude that:

- When the AOT is high and the PM2.5 is low, we have an important dilution of the plume with an advection from the S-W. The PM2.5/PM10 ratio decreases showing the contribution of coarser particles.
- When the AOT is low and the PM2.5 is high, we observe that the contribution of fine particles to the high AOT decreases.

Table 4.1. Average parameters for the classified group: 1) AOT < 0.16 and PM2.5 < 40 µg/m^3; 2) AOT > 0.16 and PM2.5 > 40 µg/m^3 ; 3) AOT > 0.16 and PM2.5 < 40 µg/m^3 ; 4) AOT < 0.16 and PM2.5 > 40 µg/m^3. Vol-F is the Sun photometer fine volume fraction, R is the PM2.5/PM10 ratio, FMF is the Sun photometer fine mode fraction, diff is the PM2.5 difference between DC and PS station, WS is the wind speed, RH is the relative humidity, WD is the wind direction.

Groups	PM10 µg/m^3	PM2.5 µg/m^3	AOT 532 nm	Vol-F µm^3/µm^2	R	FMF %	diff. µg/m^3	WS m/s	RH %	WD deg.
1	34	22	0.11	0.01	62	40	10 (57%)	4	59	189.81
2	119	86	0.36	0.08	74	75	30 (35%)	2	74	110.52
3	33	18	0.28	0.05	55	74	2 (11%)	5	68	216.63
4	80	57	0.1	0.01	71	50	17 (30%)	2	61	122.76

4.4 Vertical structure of aerosol properties

4.4.1 Restriction of the observing period

During the whole period, a lot of Lidar observations were lost because of the freezing of the surface of lens of the Lidar. We then focus on the period between February 15 and 24. As included in the preceding paragraph, this period shows an intense pollution event with changing PM2.5 and AOT from very low to high concentrations and is thus representative of different aerosol conditions. For each of AOT and PM2.5 categories we have examined Lidar profiles. We have used an aerosol micropulse Lidar manufactured by CIMEL (Boyouk et al., 2009; Pelon et al., 2008). It uses a Q-switched frequency-doubled ND:YAG laser with an expanded beam (8-10 µJ with a 200 mm exit-lens diameter) and a pulse repetition frequency of 4.7 kHz. The wavelength is 532 nm. During a 10 min data acquisition sequence, 10 individual profiles are acquired and averaged. Then the system waits for 20 min before starting another acquisition sequence. The duration of a pulse is 100 ns leading to a vertical resolution of 15 m. The profiles are averaged to reduce the influence of background noise. During the day time the background noise is dominated by direct or scattered sunlight

causing a sharp decrease in the signal-to-noise ratio. The background noise is estimated by taking the average of the backscatter signal between 22 and 30 km, then subtracting it before evaluating the signal. The data processing includes the correction of the spurious signal due to the detection of the scattered light in the receiver, called the afterpulse signal and the correction of the overlap function. The Lidar backscatter signals are calibrated for a reference altitude in which the particle backscatter coefficient is negligible compared to the known molecular backscatter. In this study the reference altitude is between 4 ~ 4.5 km on cloud-free days. Because of the after pulse the attenuated backscatter coefficients are not useful between 0 and 225 m.

We compute the aerosol extinction and backscatter coefficient using the Klett method (Klett, 1981) that requires a given Lidar ratio. We have used the method given by Boyouk et al. (2009) to compute a mean Lidar ratio from Sun photometer inversion. We obtain a Lidar ratio of 77 ± 15 sr using 37 retrievals. Due to the lake of retrieval, it is not possible to have a daily variation of this parameter. This value is the same as the one found by Cattral et al. (2005b) for urban/industrial pollution and within the range given by Ansmann et al. (2001) for continental aerosols.

We have focused on the pollution event on February considering the accessibility of Lidar data. It can be observed from the Figure 4.6 the aerosol concentration is increased between the 16 and 20 day to day about 50% every day. The lowest value of PM2.5 observed on 16 February increases to reach a maximum on 19 February. During this period, the AOT ranges between 0.05 and 0.61. On Figure 4.7, we have plotted the corresponding relative humidity and wind intensity from 15 to 24 February. We observe an increase in the wind speed and the relative humidity. The increase in AOT is in coincidence with the increase in relative humidity. Lowest AOT is observed on February 17 at 0.05 with a corresponding relative humidity of 30%, while on February 20, the AOT is 0.61 and the relative humidity is 80%.

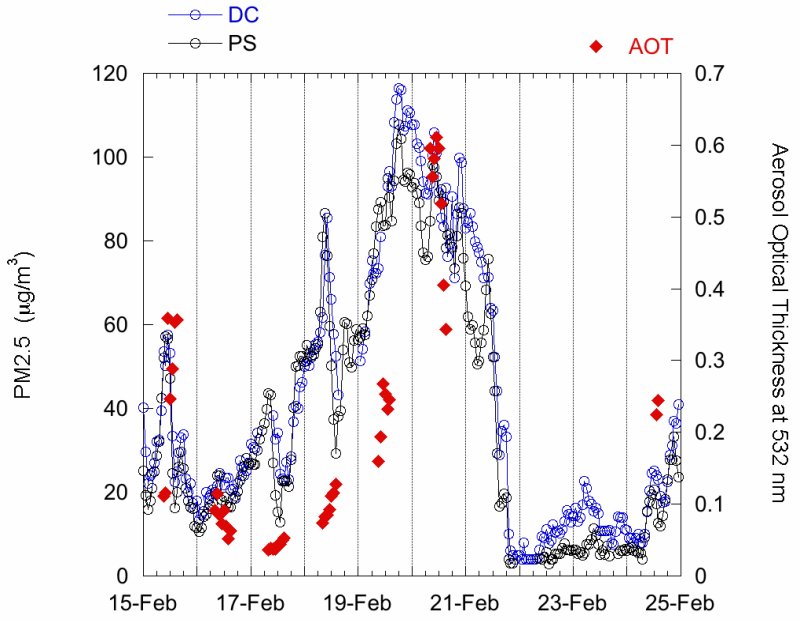

Figure 4.6 Evolution of AOT and PM2.5 at the station PS and DC from February 15 to 25, 2008

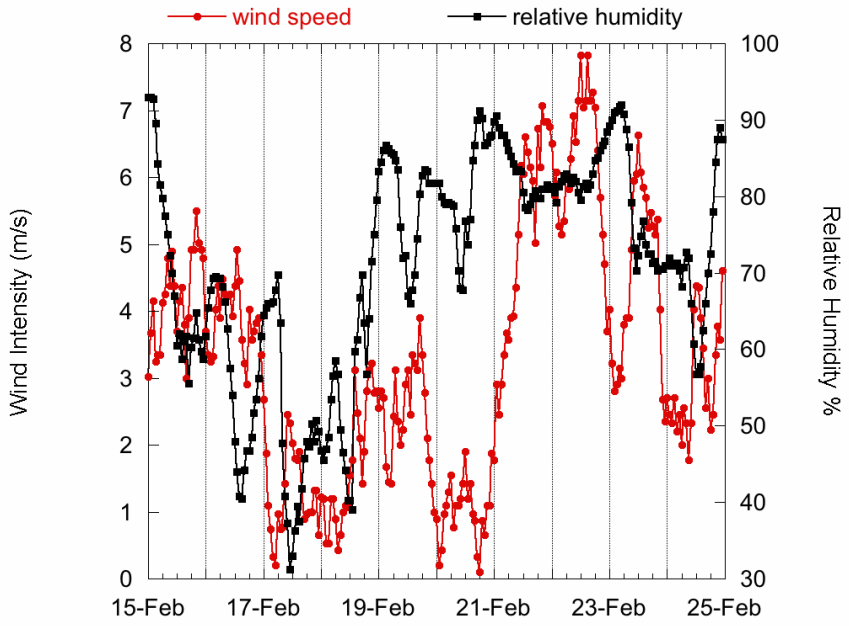

Figure 4.7 Evolution of relative humidity and wind intensity in Dunkerque from February 15 to 25, 2008

Relative humidity increase tends to enhance the aerosol size (Hänel, 1976). Consequently scattering cross section increases resulting in an enhancement on the AOT. This change in the aerosol microphysics can be also observed on the size distribution retrieved by the Sun photometer. Figure 4.8 presents the aerosol size distribution for the most accurate retrieval (small value of sky error). The aerosol size distribution shows the dominant mode is the fine mode in high and low pollution episode on 20 and 16 February respectively, with corresponding AOT at 440 nm of 0.09 (440 nm) on 16 February and 0.71 on 20 February. The fine volume of aerosol is about 74% of total volume on 20 February and 55% on 16 February. However, we can observe that the modal mean radius of the fine mode shifts to larger value on February 16 (0.1 µm) compared to February 20 (0.3 µm) which can correspond the hygroscopic growth of the particles under increasing relative humidity.

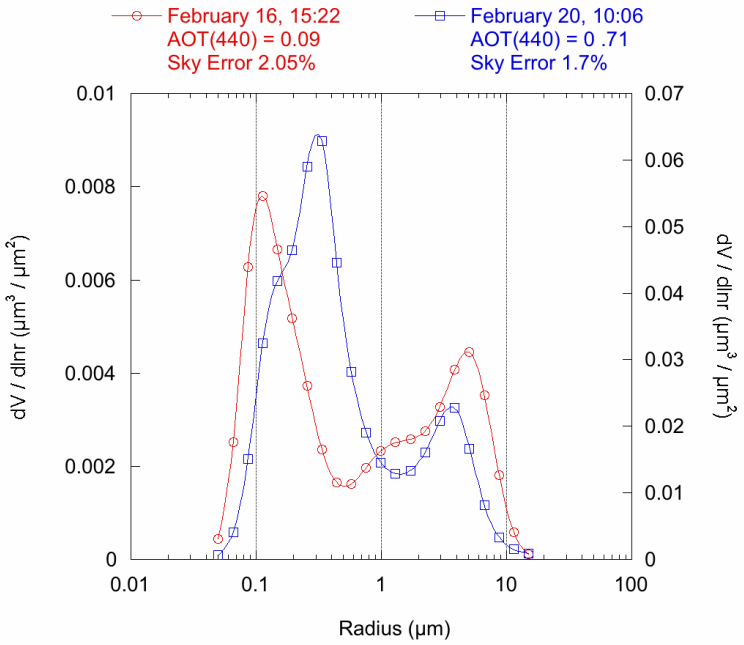

Figure 4.8 Sun photometer retrieved size distribution for February 16 and 20, 2008

Figure 4.9 presents the same relationship as displayed on Figure 4.5 but for the period between 15 and 21 February. The correlation coefficient shows an improvement considering short period of 15 to 21 February.

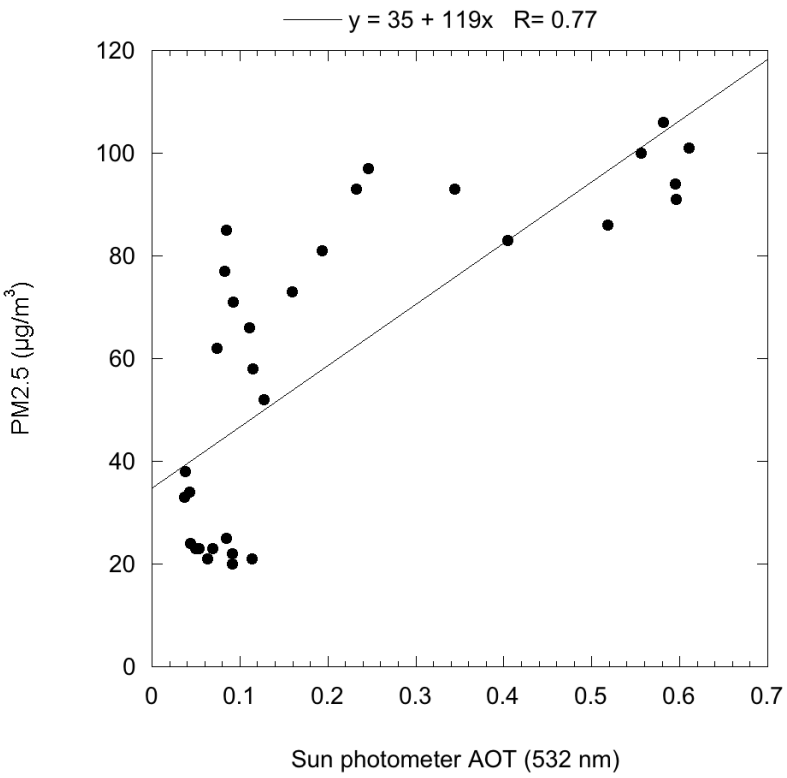

Figure 4.9 Hourly average of AOT versus PM2.5 from 15 to 21 February. The number of available data which are used is N=32.

4.4.2 Lidar observations

Figure 4.10 presents the backscatter Lidar signal between February 15 and 25. Three layers of aerosol are observed which are related to green, red and blue light color. On 17, 18 and 19 February there is high concentration of aerosol on low level layer. The low value of AOT and high value of PM2.5 on 18 February can be related to the structure of the aerosol layer with a high concentration at ground. On 16 February the aerosol layer is approximately homogenous during the day and it changes from 17 to separate to two levels of pollution observed in the ground and higher levels. On 19 February with high level of pollution of aerosol are transferring from higher level to lower layer.

The boundary layer height (BLH) has been calculated using the gradient method. The top of the mixed boundary layer (MBL) is detected using the modulus (absolute) of the minimum of the first derivative of the range corrected signal (Baars et al. 2008; Flamant et al. 1997;

Lammert and Bösenberg 2006; Menut et al. 1999; Seibert et al. 2000). Indeed, a decrease in the range corrected Lidar signal is observed in the transition zone between the aerosol load in boundary layer and the free troposphere. The BLH is shown on Figure 4.10 as black dots.

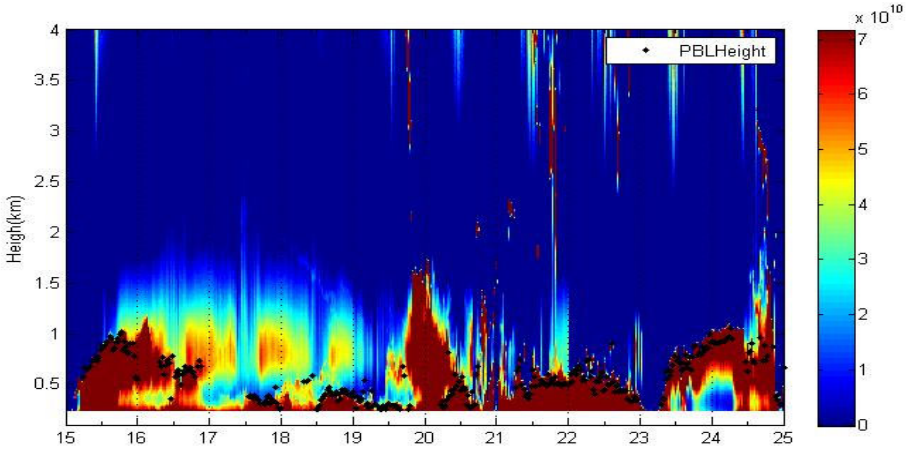

Figure 4.10 Lidar backscatter signal between 15 and 25 February 2008.

For better understanding of the relationship between AOT and PM2.5 hourly average we have selected extinction coefficient profiles corresponding to the different preceding categories. Figure 4.11 and Figure 4.12 corresponds to group 1 and 3 and categories 2 and 4. The presented figures are related to when the formation of convection process due to the solar radiation and temperature become complete at 14:00. Using Lidar measurements Janhäll et al. (2006) have shown how the mixing processes started after the morning inversion and resulted in a relatively well-mixed boundary layer with a height of 1 km around 14:00.

On Figure 4.11, we notice on the presence of large extinction coefficient (up to 0.4 km^{-1}) above 500 m and up to 1 km. This increase in the aerosol extinction coefficient is also observed on Figure 4.12 for large AOT. At the lower levels, close to the ground, there is a difference in aerosol extinction coefficient for categories 2 and 4. For category 4, the extinction coefficient is close to 0.2 km^{-1} while it is close to 1.0 km^{-1} for category 2. We observe a change in the vertical gradient of the aerosol extinction within the boundary layer for category 4 (Figure 4.12).

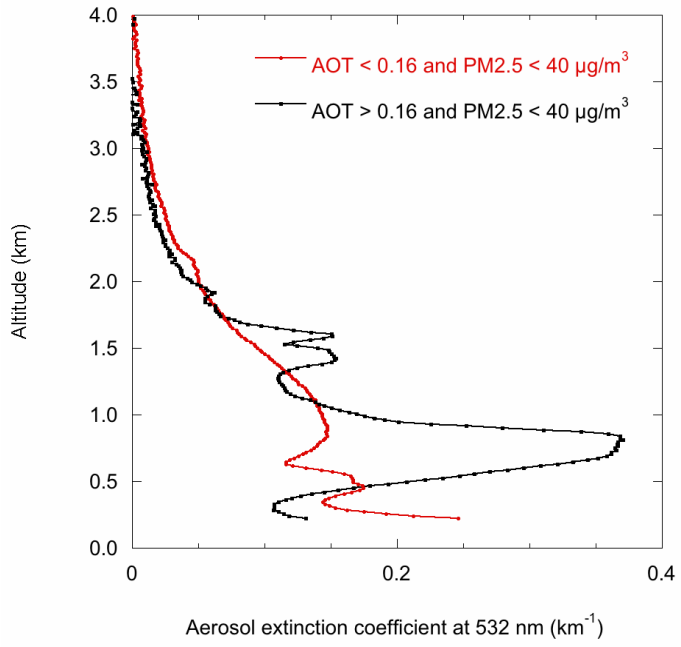

Figure 4.11 Aerosol extinction coefficient on (red) 16 February 14:00 and (black) 24 February 14:00

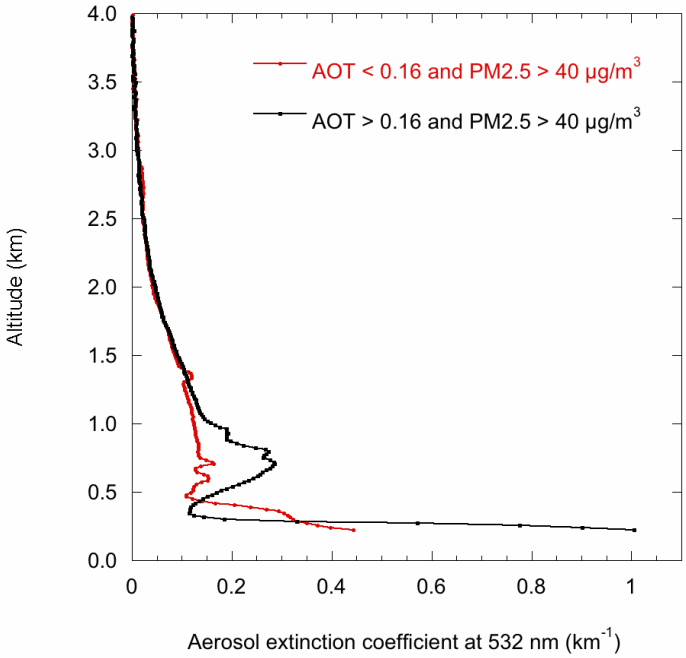

Figure 4.12 Aerosol extinction coefficient on (red) 18 February 14:00 and (black) 19 February 14:00

When focusing on the diurnal variation of coincident PM2.5 and AOT measurements, we observe that the two signals are not correlated. Figure 4.13 shows the time variation of PM2.5 and AOT between February 17 and 18. In the morning, the PM2.5 increases up to 80 µg/m^3 (on February 18) and then decreases to 30 µg/m^3 after 12:00.

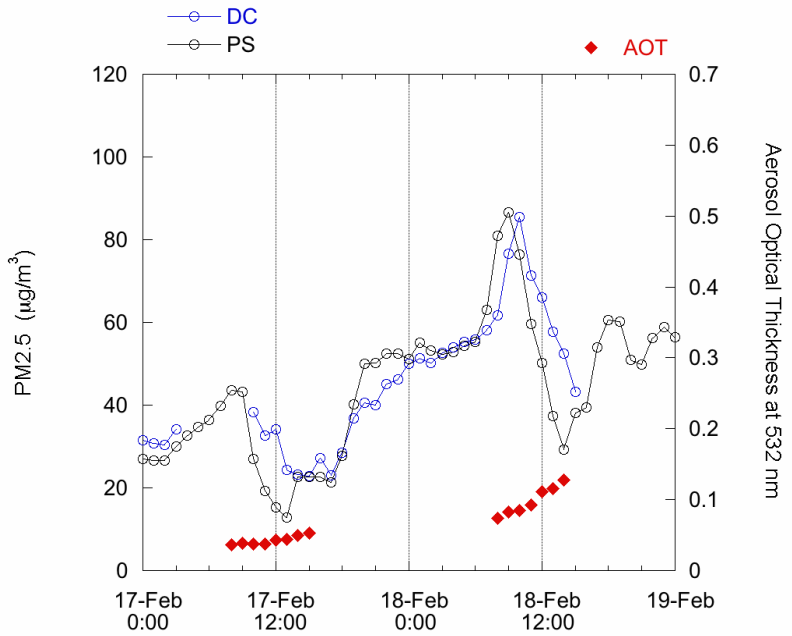

Figure 4.13 Variation of PM2.5 and AOT from February 17 to 18.

Meanwhile the AOT 0.05 changes to 0.15. The vertical profile of aerosol extinction on February 18 in the morning (10:00 UTC) and the afternoon (14:00 UTC) is presented on Figure 4.14. We can observe the increase in the boundary layer height. At 10:00, the BLH is at 270 m while at 14:00, it is at 345 m. This 30% increase in the BLH can partially explain the decrease in the ground-level PM2.5 concentration. Above 500 m the increase in the aerosol extinction coefficient is observed in the afternoon. Between 500 m and 1.5 km, the increase in the aerosol extinction coefficient represents a relative increase in the AOT of 0.02, i.e. about 20%. Surprisingly, the extinction coefficient in the lowest layer increase between 10:00 and 14:00 UTC while the PM2.5 decreases. The rapid change in relative humidity on February 18 can partly explain the change in the extinction coefficient. The relative humidity

increases from 40 to roughly 60% from 10:00 to 14:00 UTC. When considering the extinction humidity growth factor proposed by Raut and Chazette (2007), this increase in relative humidity corresponds to 25% increase in extinction, while the Lidar derived extinction increases by 50%. Because of the winter conditions, the surface layer is very shallow and probably below the Lidar vertical detection capacity. So the increase in the Lidar derived aerosol extinction coefficient is most probably due to the updraft of particles as the mixing occurs during the day and brings particles to the Lidar detection limit range.

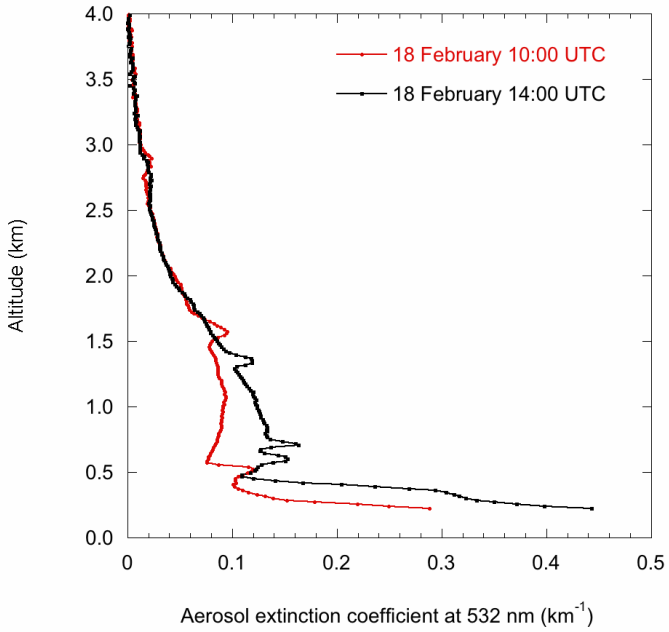

Figure 4.14 Aerosol vertical extinction profile on February 18 at 10:00 and 14:00 UTC

We have done a tentative retrieval of ground-level PM2.5 from AOT measurements. The correlation coefficient between PM2.5 and AOT is 0.76. The AOT is divided by the boundary layer height to get an average BL extinction coefficient. The fit obtained with the data presented in Figure 4.9. Three points have been removed corresponding to data acquired before 9:00 UTC on February 18 and 19. We observe a good correlation with a correlation coefficient of R=0.92. We have also applied a correction factor for relative humidity (Boyouk et al., 2009; Raut and Chazette, 2007). The regression coefficient slightly decreases to 0.90 and the slope is divided by a factor of 2. We found a slope of 5.1 (± 0.6) m^2/g when we do consider the humidity correction. This value is close to the one found fine day sea salt of 4.5

(± 0.9) m^2/g found by Hand and Malm (2007). The RMS is also decreased when applying a correction factor for relative humidity.

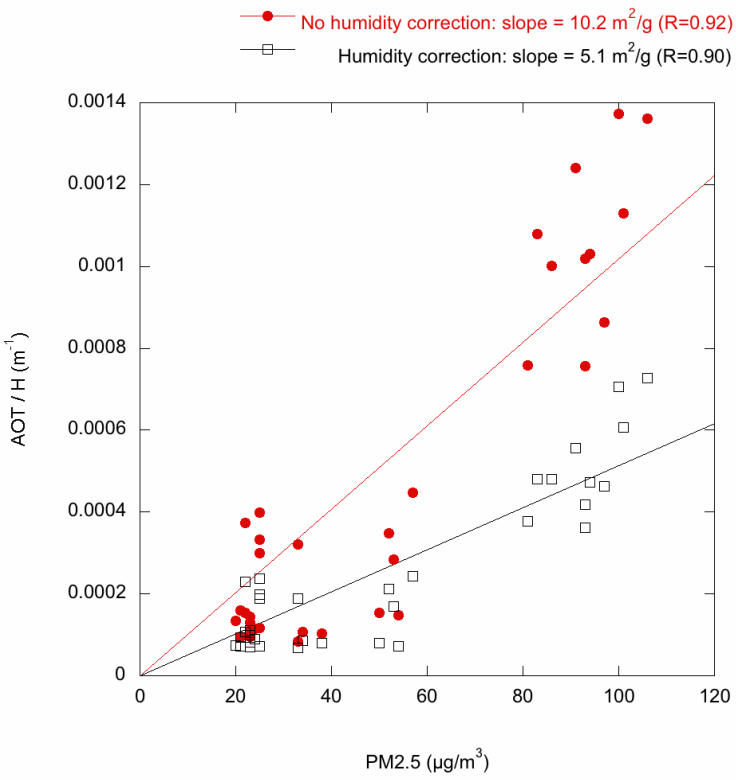

Figure 4.15 the relationship between AOT and PM2.5 (red) without RH correction (black) by RH correction during 15 to 25 Feb 2008. The number of available data which are used is N=32.

4.5 Conclusions

The retrieval of PM concentrations from optical measurements has a direct application for pollution monitoring from space. However, there are still not direct ground-level PM measurements from space instrument. All the studies that compare PM to AOT relies on direct comparison of coincident PM and AOT measurements and the use of a linear or multi-linear fitting model (Hoff and Christopher, 2009). The presented example of an atmospheric episode which depicts increases in both AOT and particle matter levels, was used to investigate local effect of aerosol pollution and find a method to distinguish local pollution from long-range transport. We have selected the winter period because this season is the most challenging when connecting PM to AOT (Kacenelenbogen, 2008). During winter time, the cold temperature prevents the development of convection and favors very shallow boundary

layer. In our study, a set of backscattering Lidar soundings, ground-level aerosol mass concentration along with Sun photometer observations were acquired during the months of December 2007 and January and February 2008. During this period, the aerosol mass concentrations were highly variable with PM2.5 between 5 and 145 $\mu g/m^3$. The observed AOT was between 0.05 and 0.61 (at 532 nm). We have classified our dataset using threshold on both PM and AOT and we have focused on the case when we observed a large mass concentration at the ground and low AOT or when we observe a low mass concentration and a large AOT. Profiles of vertical structure of aerosol in different classified PM and AOT help us to understand the vertical structure of aerosol. High AOT is always associated with a maximum in aerosol extinction coefficient above 500 m. The low PM concentration at the ground are due to dispersion by low level winds (small difference between the two stations) blowing from the South-West. In case of low AOT, the maximum of extinction is below 500 m. The wind is weak and eastward, favoring the accumulation of pollutants. The Sun photometer fine mode fraction reveals that the contribution of fine particles to the AOT is weaker than when the AOT is high.

We made a tentative inversion of ground-level PM2.5 from AOT and Lidar derived boundary layer height measurements. The use of the Lidar derived BLH strongly increases the correlation between AOT and PM2.5. The final correlation is good (R=0.90) and we found a mass extinction efficiency of 5.1 m^2/g when using a relative humidity correction factor of 0.55. This value totally depends on the relative humidity correction factor that we applied.

Data from Dec. 2007 to Feb.2008 also demonstrates the importance of vertical profiles in understanding the meteorological and dynamical control factors during pollution episodes. These measurements help in describing the dynamical processes that occur in the lower atmosphere, especially during pollution events and have shown the importance of vertical mixing, horizontal transport and the importance of local meteorology on the aerosol pollution.

5 Impact of Sea breeze on vertical structure and optical properties and mass concentration of aerosol in Dunkerque area, France.

5.1 Introduction

Sea breeze is a well-known meso-scale meteorological phenomenon (Miller et al., 2003) that is primarily attributed to the horizontal temperature differences between land and water in coastal zones. Sea breezes impact on air quality of coastal areas under different mechanisms (Abbs and Physick, 1992; Kitada, 1987; Simpson, 1994). Cool, stable marine air encounters a thermodynamically unstable situation when it advects over a hot land surface. As the marine air mass moves inland and conducts heat from the land surface, convective current begins to develop, and modified air is transported vertically. As the air moves farther inland, convective currents reach progressively greater heights. The vertical mixing results in a thermal internal boundary layer (TIBL) near Earth's surface whose upper limit increases nonlinearly with distance from the coast. Above the TIBL the remaining unmodified marine air acts as a cap that prevents mixing between destabilized marine air below and the advected air above. The locally emitted pollutants are then trapped in this shallow surface layer resulting in an increase in their surface concentration. Moreover the development of the TIBL further inland can bring pollutant-rich air aloft and also increases the surface concentrations (Lin et al., 2007). The impact of sea breezes on air quality is of particular interest in trade harbors and their vicinities, which are often concerned by poor air quality (Georgieva et al., 2007).

The harbor of Dunkerque, France (51°N, 2°E) is one of the largest trade harbor in Europe and locally contributes to major emissions of pollutants such as NO_x, SO_2, CO, CO_2, VOC and aerosols (Rimetz-Planchon et al., 2008). Dunkerque district experiences sea breezes from May to September (Damato et al., 2003). Their occurrence depends on the thermal gradient between land and sea but also on the large scale weather system, and is favored by the presence of the North European anticyclone (Damato et al., 2003). Some studies have been devoted to the detection (Bigot, 2003), characterization (Leriche et al., 1998) and numerical modelling (Talbot et al., 2007) of sea breeze in the North of France. Elastic backscatter Lidar provides an interesting insight into the structure of sea breeze (Kolev et al. 1998; Nakane and Sasano 1986; Sicard et al. 2006). Murayama et al. (1999) observed a boundary structure in the lower atmosphere, which might correspond to the mixed layer (the internal boundary

layer) or sea breeze in which crystallized sea salt and/or dust particles were diffused. The recent development of compact eye-safe micro Lidars fosters the systematic use of Lidar soundings in the characterization of land and sea breeze.

In this chapter, we report Lidar observations acquired during a field campaign on July 2008 in Dunkerque. The temporal evolution and spatial distribution of mixed layer height have been observed considering different factors, including the synoptic conditions, and local circulation patterns. The objective is to characterize the temporal and spatial variations of mixed layer height in Dunkerque area during the sea breeze study and its impact on ground-level aerosol concentrations.

5.2 Instrumentation and method

5.2.1 Lidar

We have used a Leosphere EZ- Lidar (Lolli et al., 2008). The Lidar uses a tripled pulsed laser source Nd:YAG at 355 nm with an energy of 16 mJ and pulse repetition rate of 20 Hz. The Lidar was tilted by a zenith angle of 50 degrees. The observation ranges from 134 m altitude to about 10 km and the vertical resolution is 9.6 m (it is 15 m when the Lidar is pointed to the zenith). The Lidar operated at the third floor of a building at the height of about 10 m above the ground and located at 2.368° E and 51.04° N. The building is located between the urban and industrial area of Dunkerque and less than 1 km from the sea shore (see Rimetz-Planchon et al. (2008) for a detailed map of the experimental area). The measurement period started from July 14 to 28, 2008. The Lidar was working continuously with a time step of 4 minutes, corresponding to an average over 4800 shots. Further description of this instrument can be found on the website: http://www.leosphere.fr. The signal in the upper clear air is normalized on the molecular contribution. The signal is corrected from the background sky radiance, which is acquired after each Lidar profiles. The correcting overlap factor is for short-range heights where the field of view of the telescope does not overlap the laser beam. It is close to 1 at 200 m above the telescope.

Lidar data have been inversed using a well known method, based on Bernoulli's differential form of the propagation equation (Klett, 1981). The backscatter Lidar equation is undetermined due to its dependence on the two unknown backscatter and extinction coefficients. The Lidar ratio is assumed constant as a function of the range and it is estimated

by comparing the lidar retrieved aerosol optical thickness (AOT) with Sun photometer observations. AOT was measured by an automatic Sun photometer (Holben et al., 1998) located on the same building as the Lidar.. Figure 5.1 shows the comparison between the Lidar-derived AOT and the Sun photometer derived AOT during July 24, 2008. The best fit is obtained for a Lidar ratio of 30 sr. This is a typical value for polluted marine air (Ackerman, 1998; Müller et al., 2007). The mean relative error in the Lidar AOT is about 10% compared to Sun photometer measurements.

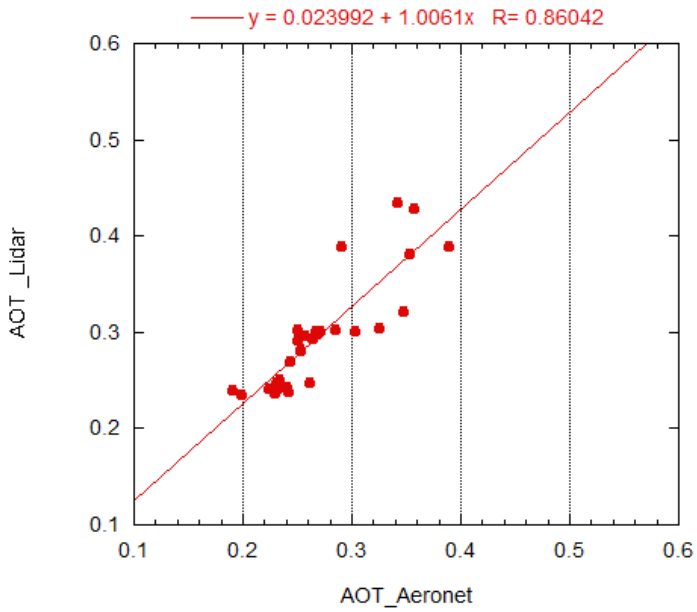

Figure 5.1 Comparison of aerosol optical thicknessat 355nm obtained by Lidar and sun photometer on 24 July 2008. The number of available data which are used is N=27.

To determine the temporal evolution and spatial distribution of the mixed layer depth during the sea breeze we have used data gathered with the Leosphere Lidar operating at 355 nm. The estimation of boundary layer height is based on detecting the gradient in the Lidar backscatter signal associated with the decrease in aerosol backscatter which is often found in the transition zone from the mixed layer to the overlying free troposphere. To objectively locate the maximum backscatter gradient at the top of the boundary layer we applied gradient

method to each Lidar profile. Outliers in the resulting time series of mixed layer depth are removed using a simple consensus algorithm. Lidar signal is proportional to particle concentration so that Lidar – derived atmospheric backscattering is generally observed to be large in the atmospheric boundary layer and in elevated aerosol layer inside the free troposphere (residual aerosol or dust aerosol layers).

5.2.2 Particle matter (PM) concentrations and meteorology measurements

The hourly averages concentrations of PM2.5, PM10 and SO_2 have continuously been monitored by air quality monitoring network of region Nord Pas de Calais (http://www.atmo-npdc.fr). They are classified as traffic, urban, suburban and industrial. We have chosen Dunkerque center station to trace the pollutant which is placed near to sea and Lidar setup and Sun photometer. PM2.5 and PM10 are measured using a Tapered Element Oscillating Microbalance (Patashnick and Rupprecht, 1991).

5.3 Detection of the sea breeze using meteorological parameters and Lidar observations

5.3.1 Overview of meteorology and lidar observation

Sea breeze experiment is scheduled between 14 and 28 July 2008. Observations discussed here were mainly made on clear days accompanying high pressure systems when sea breeze circulation developed. During this period, we have observed three consecutive days on July 23, 24 and 25 with occurrence of sea breeze. On July 23 a high pressure system (1026 mbar) was located on the North of France and moved northward to Sweden on July 24 and 25. Sea breezes are characterized by a quick shift of the wind direction to the northern sector (NNE, wind blowing from the sea), starting at around 09:00 UTC and lasting several hours simultaneously with an increase of the wind speed typically more than 1 to 3 m/s (Bigot 2003; Miller et al. 2003; Talbot et al. 2007). Following criteria identify the sea breeze days: warm season, high pressure, rapid change in the wind direction some hours after sunrise, toward winds from the N sector, low initial wind speed before the change on wind direction, wind speed increase, northerly wind lasting several hours, no night wind blowing from the N sector.

Figures 5.2, 5.3 and 5.4 present the daily variation of the ground-level relative humidity, temperature, wind speed and direction, and the 2D range corrected backscattered Lidar signal for July 23, 24 and 25, respectively. The Lidar pictures show a 4-minute time height cross section of aerosol backscatter measured on July 23, 24, 25 2008. The sharp decrease of aerosol backscatter near the top of the boundary layer is clearly visible. Overlaid blue line is the mixed layer depth estimated from the Lidar signal. On July 23 (Figure 5.2), after sunrise at about 7:00 UTC, the surface and the adjacent air masses temperature gradually increases while the relative humidity decreases. The transition preceding the sea breeze occurred at 09:45 UTC. It is marked by a sharp increase (from less than 1 to more than 4 ms^{-1}) in wind speed. The wind rotates eastward from a predominant S direction to the N. The transition period lasts for less than 1 hour. On July 24 (Figure 5.3), the surface wind speed increases as a consequence of the northward shift of the anticyclone. The transition preceding the sea breeze occurred at 12:30 UTC. The flow pattern shows southeasterly wind with average speed of 3 ms^{-1} during the morning after which the wind shifts to a N-NE and increases in speed with the onset of the sea breeze. The increase in the relative humidity and the decrease in the temperature (3 °C) are of the same order as for July 23. On July 25 (Figure 5.4), the transition preceding the sea breeze occurred at 11:30 UTC. Before the transition, the ground-level temperature (27 °C) is higher than for the previous days and temperature drops during the transition period twice more than previous day. The flow pattern is characterized by southeasterly wind at 3 ms^{-1}. The increase in the wind speed during the transition period is of the same order as for the previous days. As opposite to the previous day, the wind turns to the W and N-W and stays N-NW during the sea breeze rather than N-NE as previous observation.

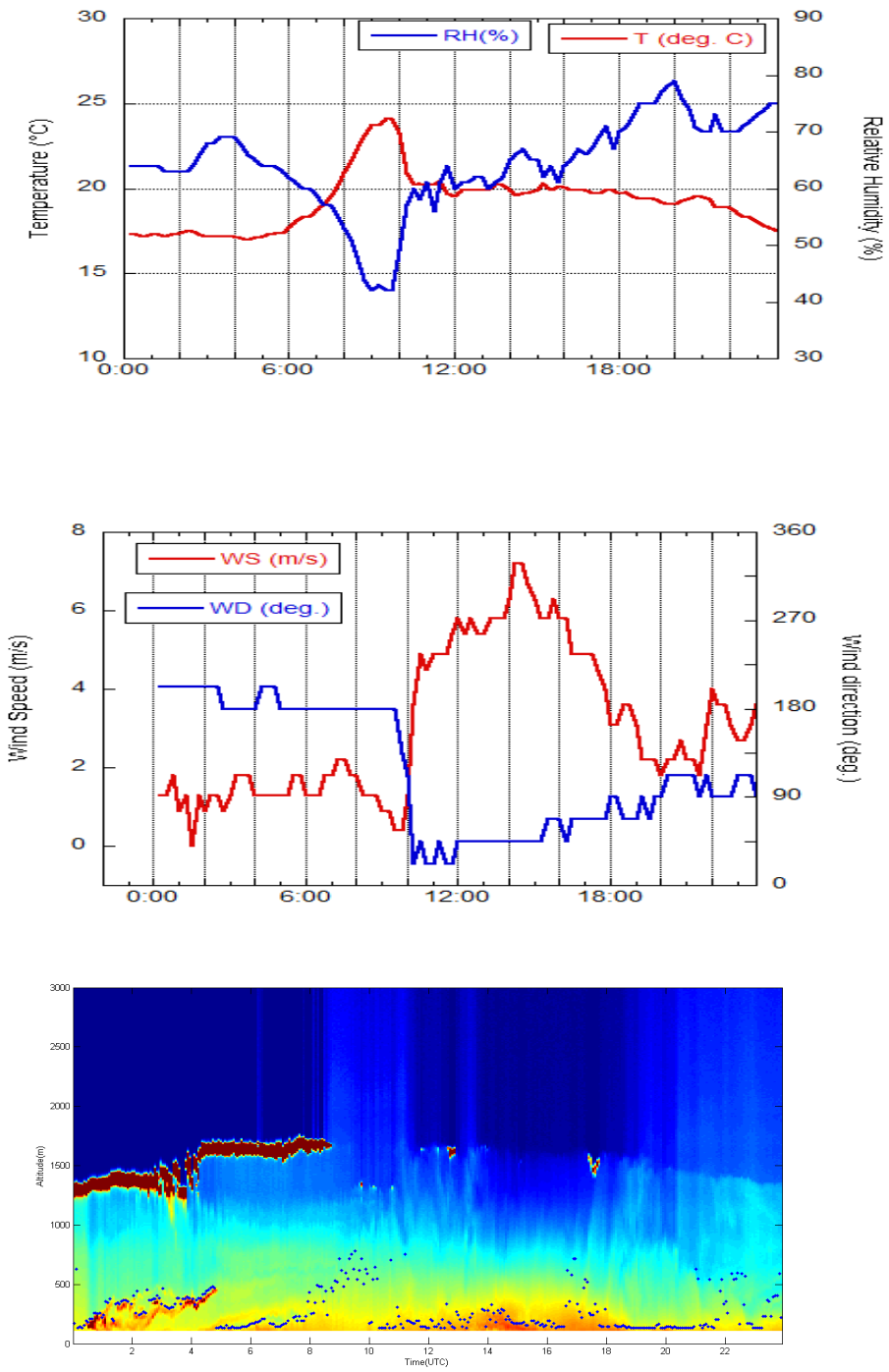

Figure 5.2 Meteorological parameters and 2D Lidar image on July 23, 2008.

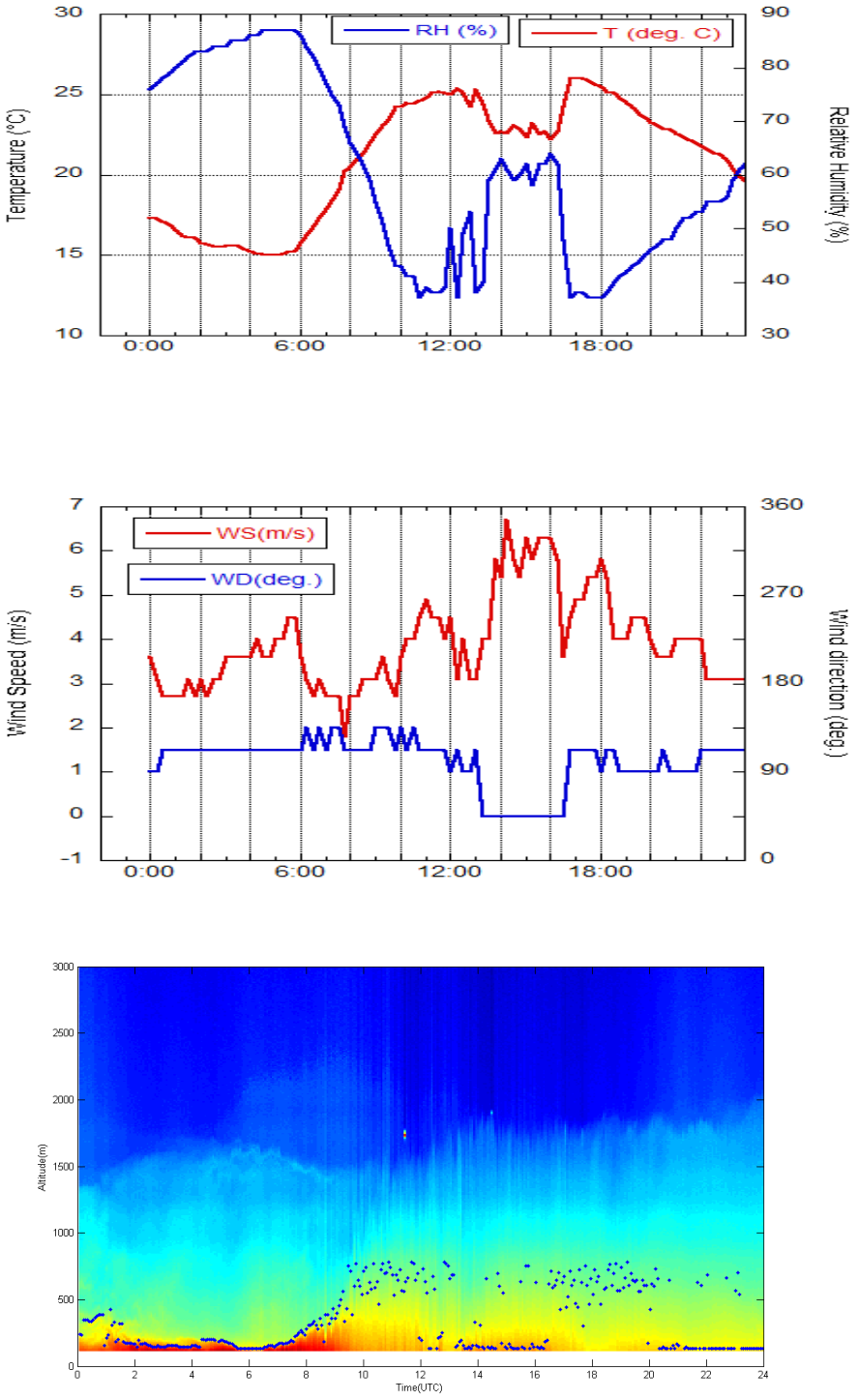

Figure 5.3 Meteorological parameters and 2D Lidar image on July 24, 2008.

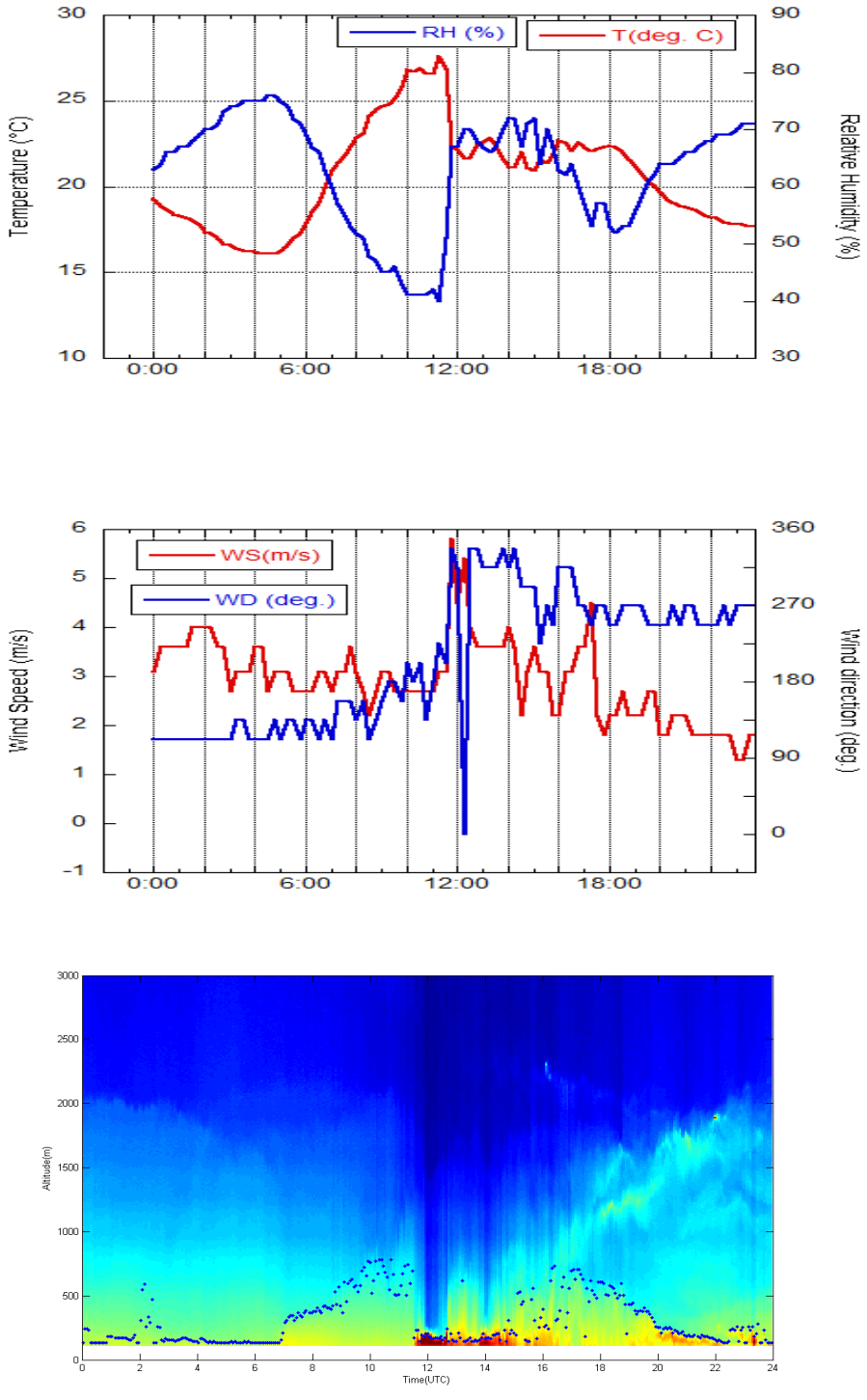

Figure 5.4 Meteorological parameters and 2D Lidar image on July 25, 2008.

On Figure 5.2, the presence of low level clouds can explain the disturbance in the nocturnal boundary layer that can be observed in the range corrected Lidar signal before 5:00 UTC. Some remaining clouds can be observed at 13:00 and 18:00 UTC.

5.3.2 Extinction profile at sea breeze onset

Two marked features are the increase and decrease of extinction coefficient at the time of onset and end of sea breeze. The start of breeze considering the time when the wind is rotating from north to other direction can be also identified in the Lidar signal (Figure 5.5).

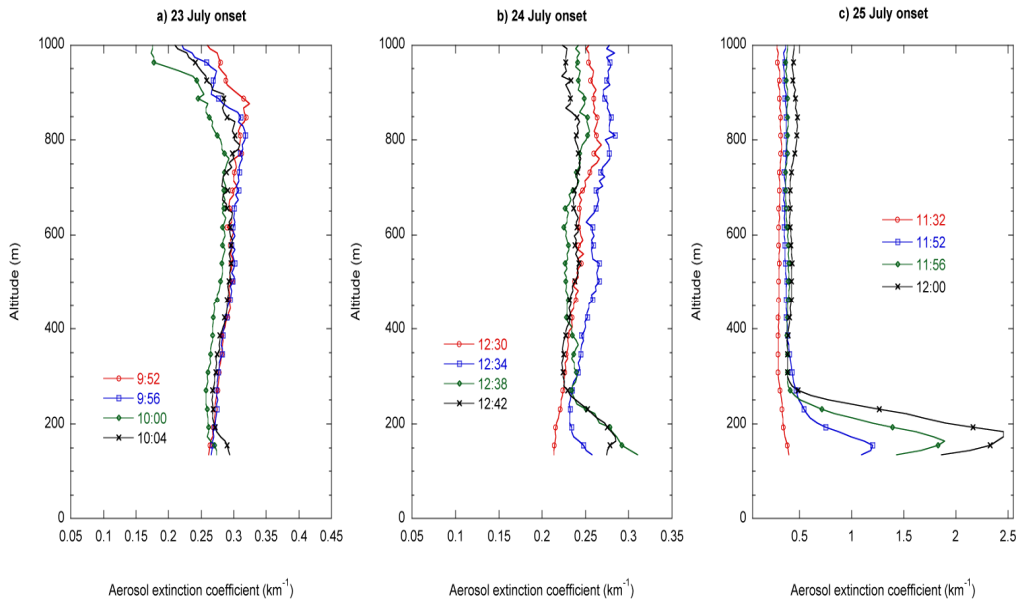

Figure 5.5 The vertical profile of aerosol extinction coefficient at the onset of the sea breeze on (a) July 23, (b) July 24 and (c) July 25, 2008

We can use the Lidar signal variation to precise the onset and end of breeze. Figure 5.5a, 5.5b and 5.5c show the evolution of the aerosol extinction profile during the transition preceding the onset of the sea breeze on July 23, 24 and 25, 2008. It presents the aerosol extinction distribution up to 1000 m every 4 minutes just before and after rotating of wind to North.

Most of the time, we can observe three aerosol layers. On July 23 (Figure 5.5a), before the breeze at 9:52 and 9:56 UTC, we observe a first layer up to 400 m with an aerosol extinction coefficient varying between 0.25 km^{-1} and 0.27 km^{-1}. A second layer is located between 400 m and 650 m with an extinction coefficient of about 0.29 km^{-1}. Above this former layer, we observe a third layer between 650 m and 1000 m with an aerosol extinction coefficient decreasing from 0.32 km^{-1} to 0.26 km^{-1}. After the breeze (10:00 and 10:04 UTC) the aerosol extinction coefficient increases in the lowest layer between 134 m and 200 m, creating a new layer with the highest extinction coefficient of 0.28 km^{-1}. The second layer has an altitude between 250 m and ~300 m with a value of 0.26 km^{-1}. The third layer from 300 to 750 m has higher value of extinction coefficient and it is increasing from 0.26 to 0.29 km^{-1}. The last layer between 750 to 1000 m has an extinction coefficient varying between 0.29 km^{-1} and 0.17 km^{-1}. Figure 5.5b shows the temporal evolution of the onset of the sea breeze on July 24. Before the breeze (at 12:30 UTC), it can be observed increasing extinction up to 650 m. After the breeze three distinct zones in the aerosol extinction coefficient are observed. The extinction coefficient is about 0.22 km^{-1} in the lowest layer (up to 250 m) and it changes to 0.32 km^{-1} after sea breeze (at 12:38 UTC). The second layer is about 270–320 m and the extinction coefficient is approximately 0.22 km^{-1}. The second layer separates the region with least extinction from that with the greatest extinction (at 12:42 and 12:38 UTC). On July 25 (Figure 5.5c), the situation is different because of the high extinction value in the lowermost layer. It is more than 5 times compared to layer above 250 m and up to 1 km. The extinction in the first layer increases between 0.5 km^{-1} (at 11:32 UTC) and 2.5 km^{-1} (12:00 UTC). Up to 700 m the extinction coefficient is between 0.47 and 0.5 km^{-1} and in the last layer between 700 to 900 m the aerosol extinction coefficient is increasing from 0.49 to 0.51 km^{-1}.

5.4 Impact of the thermal internal boundary layer on the particle matter observations

5.4.1 PM and boundary layer height observations

Dunkerque area has a considerable spatial variability of mixed layer height due to its coastal location and variations in land use. Marine boundary layers are typically only in order of several hundred meters deep and their depth does not vary much over the course of the day. The mixed layer height over land, however, exhibits a strong diurnal cycle and typically peaks in the afternoon at depths of up to 1 km.

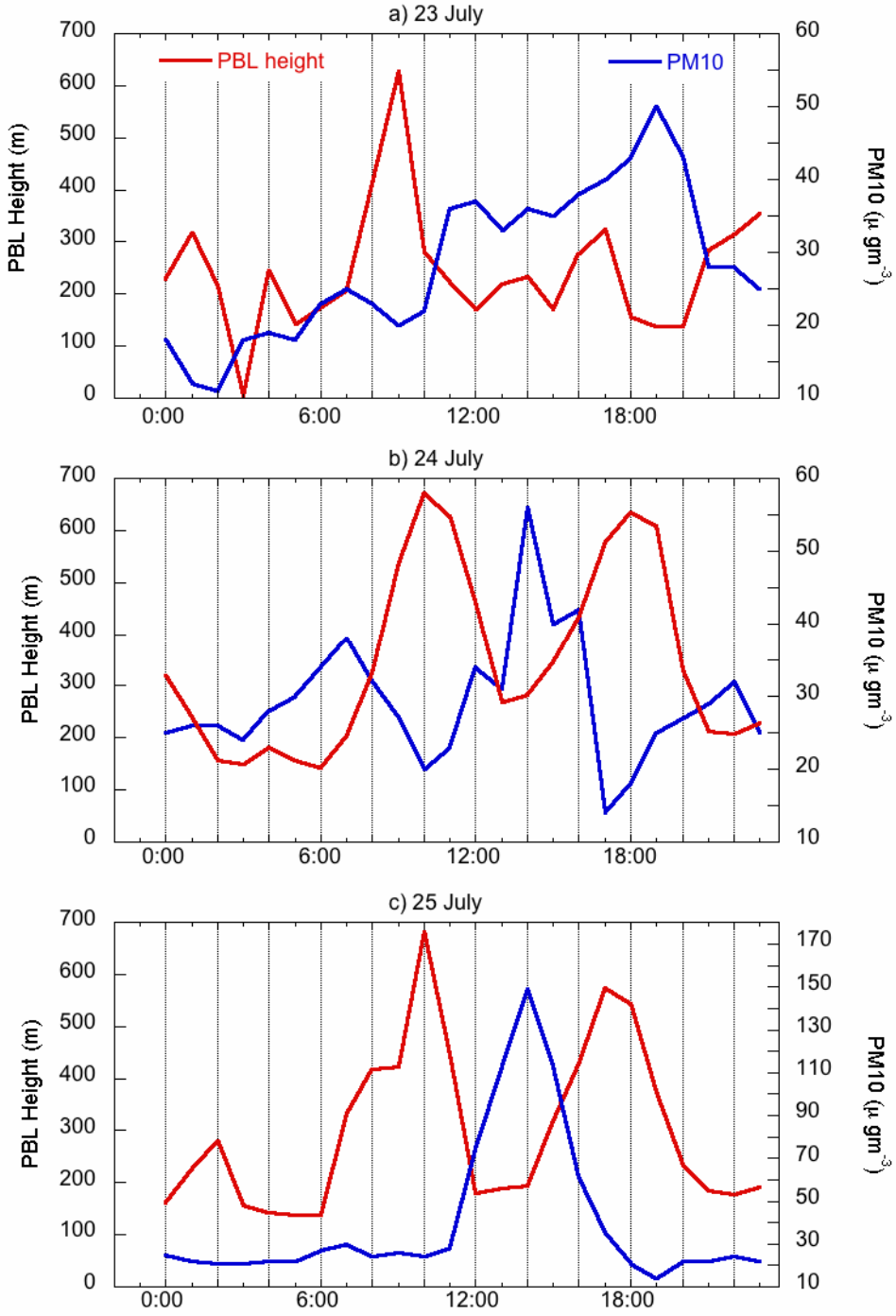

Figure 5.6 Diurnal cycle of PBL height and PM10 for July a)23, b)24 and c)25, 2008

As the sea breeze became established in the early afternoon, mixing heights declined due to the advection of marine air with shallow mixing depths. Mixed layer height is an important meteorological parameter that affects near-surface atmospheric pollutant concentrations since it determines the volume of air into which pollutants and their precursors are emitted.

The hourly PM10 recorded at the DC station are presented on Figure 5.6 along with the hourly change in the boundary layer height (BLH). The sea breeze occurrence is characterized by a dramatic decrease in the BLH due to the advection of cool air from the sea. After a steady growth because of solar heating, the BLH tends to reach 600-700 m around 8:00 UTC. The sharp BLH decrease is smoothed out on the hourly average (see Figure 5.2c, 5.3c and 5.4c for 4-min data). The meteorology condition and wind patterns were very similar on July 24 and 25, and the boundary layer depths show a similar temporal evolution of mixing heights. The PM10 increases from 20 to 35 $\mu g/m^3$ after the sea breeze on July 23. On July 24, the PM10 increases from 20 to 55 $\mu g/m^3$ while on July 25, it changes from 20 to 149 $\mu g/m^3$.

The situation on July 23 is clearly different from July 24 and 25. On July 23, because of the early onset of onshore flow the temporal evolution and spatial distribution of boundary layer height was dominated by advection of marine air with shallow mixing depths. The same day, after the decrease in the mixing height, the BLH remains at about 200 m due to the advection of marine air (see Figure 5.2b) from the North. The PM10 tends to slightly increase during the day. These results from the accumulation of urban and industrial pollutants offshore in the morning with a southerly wind creating an offshore reservoir: the sea breeze then brings back these pollutants inland. On July 24 and 25, the PM10 peak is less than 2 hours after the occurrence of the sea breeze front. Then PM10 reach to level close to before the onset of the sea breeze, typically 15 $\mu g/m^3$ on July 24 and 25. This decrease in the PM10 is well correlated with the increase in the BLH. Figure 5.7 shows the negative correlation between BLH and PM10 for July 24 and 25 between 10:00 and 18:00 UTC. The difference in slopes (a factor of 3) clearly indicates that BLH decrease is not the only phenomena that can explain the increase in the PM10 content. The main difference between both days is due to rotation of wind direction during the sea breeze onset. On July 25, wind turns westward and then the observation site is directly under the influence of the main industrial area and trade harbor. While on July 24, the wind turns eastward, blowing from an area with less emission.

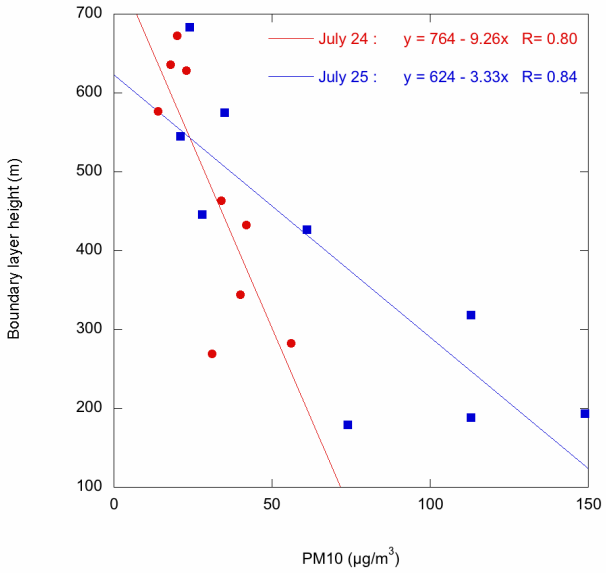

Figure 5.7 Comparison between hourly PM10 and boundary layer height acquired from 10:00 to 18:00 UTC on July 24 (red) and July 25 (blue) 2008. The number of available data which are used is N = 9.

.

5.4.2 Temporal variation of PM2.5/PM10 on 23, 24 and 25 July

Figure 5.8 shows the variation of PM2.5/PM10 ratio as a function of the time of the day. On July 25, the PM2.5/PM10 ratio drops from 0.7 to 0.2 while on July 24 it goes down upto 0.5. This indicates the advection of coarse particles. The SO2 concentration also shows a sharp increase on July 25 indicating an industrial origin. It is observed the high variation of SO2 concentration from less than 5µg/m^3 to 30µg/m3 during the sea breeze. Pollutant such as SO2 or PM can be rapidly mixed to the surface when they encounter the convective currents within the TIBL (Barbato, 1975; Gangoiti et al., 2002). Fumigation occurs when air pollution plumes emitted in stable regions of the marine air mass encounter the top of the TIBL and are rapidly mixed down to the surface. Plume mixed to the surface may be vertically transported hundreds of meters aloft in updrafts associated with convention or lines of low level convergence, then divided into multiple branches which move in many different directions. Some may eventually be caught up in the seaward return flow, transported many tens of kilometers offshore, and recirculated landward within the sea breeze cell. The pollutant

concentration within the sea breeze cell can grow throughout the day as fresh emissions are fumigated downward into the TIBL, adding to order pollutants already in the sea breeze system (Miller et al., 2003).

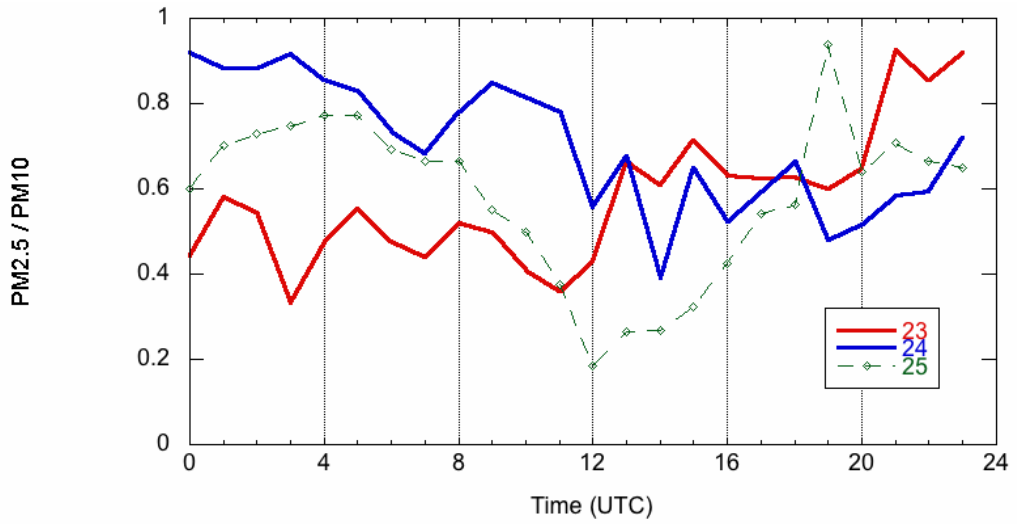

Figure 5.8 Temporal variation of PM2.5/PM10 ratio on July 23 (red, the sea breeze starts at 09:45 UTC), 24 (blue, the sea breeze starts at 12:30 UTC) and 25 (green dash, the sea breeze starts at 11:30 UTC) 2008.

5.4.3 Lidar signal at the lowest level

Temporal variation of the backscatter Lidar signal at the lowest level is related to the aerosol concentration close to the ground. Figure 5.9 shows diurnal evolution of Lidar signal for lowest observed layer at 134 m and the ground-level PM10 and PM2.5 on July 23, 24 and 25. We can observe a remarkable similarity between the ground-level concentration and the Lidar signal on July 23. An excellent correlation between the Lidar signal and PM2.5 (correlation coefficient R=0.91) and PM10 (R=0.80) is obtained when considering data before 18:00 UTC corresponding to the end of the sea breeze. However, on 24 July the signal is well correlated to PM2.5 (R=0.72) but not to PM10 (R=0.08). The signal is also correlated to the relative humidity (R=0.66). On July 25, the signal is not correlated to the PM2.5 (R=0.23) but well correlated to PM10 (R=0.72) and to PM10-PM2.5 (R=0.79).

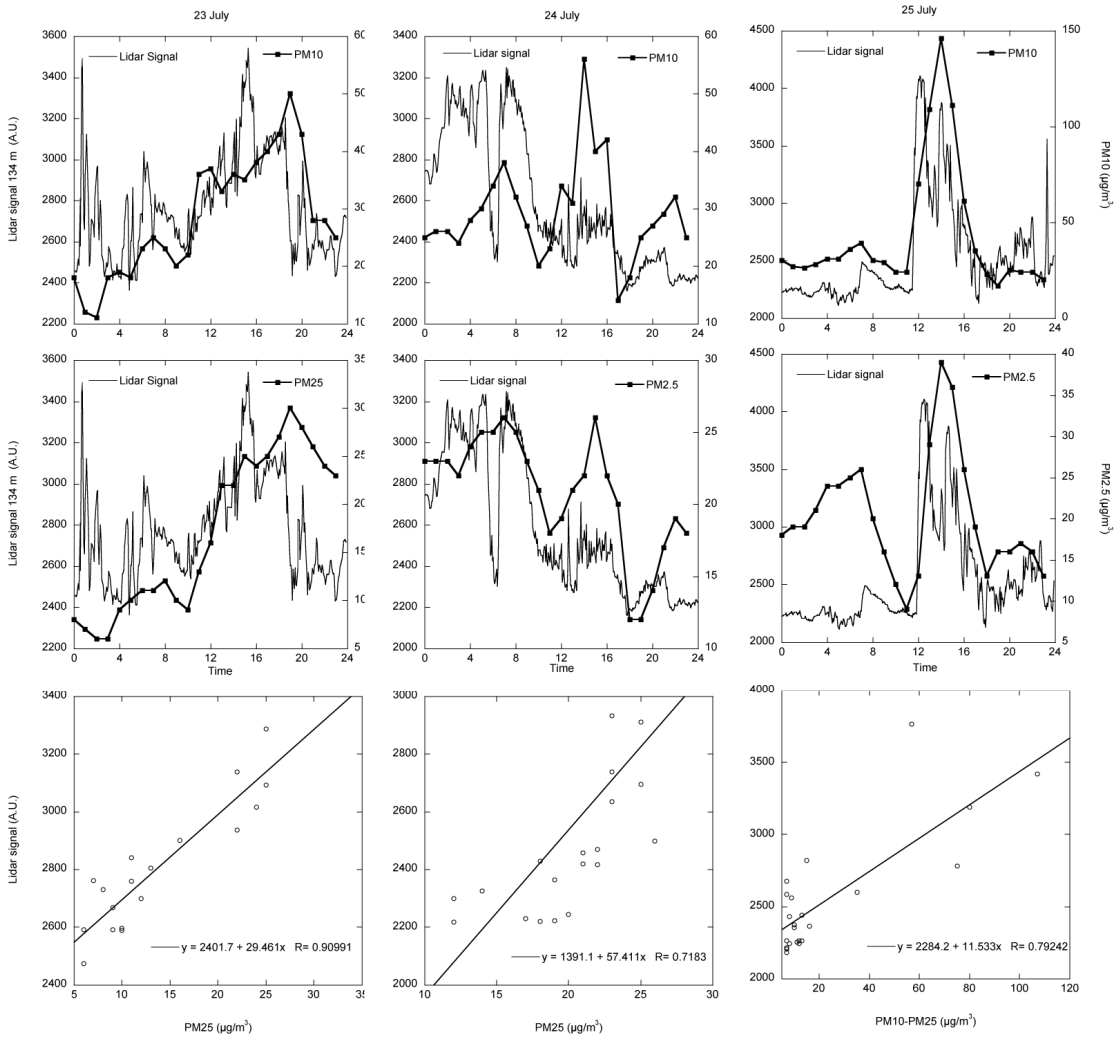

Figure 5.9 Daily variation of the Lidar signal recorded at 134 m and the ground-level and PM10 (first row) and PM2.5 (second row) ground-level concentrations on July 23 (left column), 24 (center column), and 25 (right column), 2008. The third row corresponds to the correlation between hourly average of Lidar signal at lowest level and PM2.5 on 23, and 24 and between the differences of PM10-PM2.5 on 25 July 2008.

5.5 Columnar and vertical aerosol optical properties during the sea breeze

5.5.1 Variation of AOT and size distribution

Moorthy et al. (1992) have shown that sea breeze has a significant and short lived impact on the columnar optical depth, and size distribution at a tropical coastal. Aerosol optical depths increase during the occurrence of the sea breeze front. This increase is associated with sea-breeze front which could be attributed to the combined effect of sharp increase in RH in front convergence zone (updraft region) and to increase in small particle content due to advection of marine aerosol (Moorthy et al., 1992). During our experiment, we did not observe such a feature. We have quasi-continuous AOT observation during daytime only for July 24. The AOT ranges between 0.2 and 0.4 (see Figure 5.10 and Figure 5.11) and increases continuously during daytime. We can observe a slight increase in the AOT when the sea breeze front occurs, but there is no evidence of a direct impact. The same conclusion can be drawn for the retrieved aerosol size distribution.

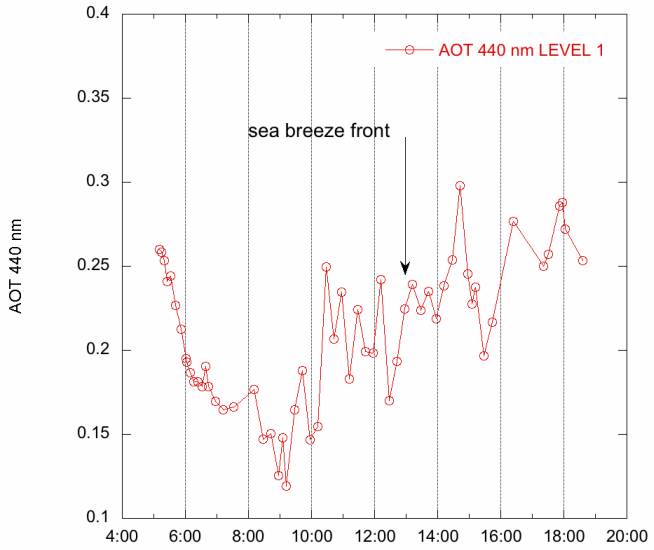

Figure 5.10 Variation of aerosol optical thickness obtained by Sun photometer (Level 1 data) on July 24.

Figure 5.11 compares the two size distribution measured by Sun photometer at 8:11 and 16:24 on July 24. The amplitude of the coarse and fine increases as AOT increases but the shape of the size distribution remains the same. However, we can note that the mode peaking at 1 µm observed in the morning does not appear in the afternoon. This change in the shape of the distribution might be due to the hygroscopic growth or the settlement of large particles.

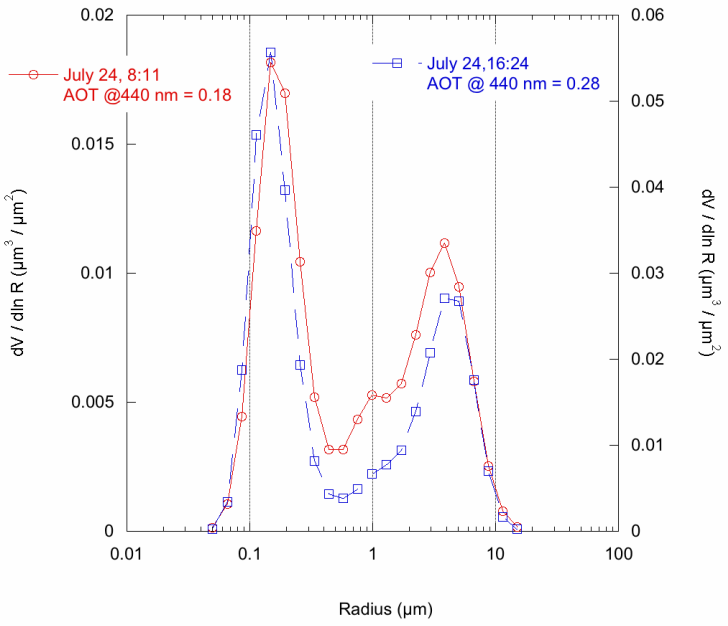

Figure 5.11 Sun photometer retrieved size distribution on July 24. Note the scales are different for each distribution.

5.5.2 Evolution of extinction profiles

The sea breeze is a challenging atmospheric phenomenon difficult to characterize because it happens at relatively small temporal and spatial scales and its onset strongly depends on synoptic weather conditions. The rapid change in the vertical structure of the atmosphere is depicted by the 2D cross sections of Lidar signal(Figure 5.2c, 5.3c and 5.4c). Using Lidar cross section at the Black Sea shoreline, Skakalova et al. (2003) demonstrate that during the transition period the relative extinction distribution reveals existence of 3 different zones: 1) a zone above the surface, which possesses the optical properties of the entire layer which develops subsequently; 2) a second zone which possesses the optical characteristics typical for circulation before the transition and 3) a third zone, characterized by the lowest relative extinction coefficient and placed between the other two, which dissipates by the end of the transition. The sea breeze during the day can pass along an area and replace the aged air mass with moist, cool, and clean air. In addition, the nocturnal boundary layer jet can carry out pollutants hundreds of kilometers without producing much of a signal at the surface. By developing the boundary layer in next morning, pollutants enter to the surface and make rapid increase in concentrations of pollution which is not due to local urban primary and secondary

production. 25 July is a follow of sea breeze days when the impact of sea breeze from 23 and 24 has influenced the level of pollution and vertical structure of extinction coefficient at a regional scale.

The evolution of aerosol extinction coefficient and Lidar signal S on 25 July are presented on Figure 5.12. The sun rises at about 6:00 UTC. Approximately 1 hour after sunrise, the temperature in land has increased and it causes the land breeze becoming weak. We present in Figure 12 the aerosol extinction profile acquired at 6:55 UTC. There is a layer below 180 m with an aerosol extinction coefficient between 0.20 and 0.24 km^{-1} and another layer with extinction coefficient between 0.15 and 0.20 km^{-1} is observed at the altitude between 220 and 300 m. Above this layer and up to 1 km, the extinction coefficient varies between 0.10 and 0.15 km^{-1}. At 7:59 UTC, the lowest layer disappears because of the vertical mixing and the development of boundary layer. At 9:31 the boundary layer top reaches at 550 m and the extinction is 0.21 km^{-1}. Our observation is similar to what Skakalova et al. (2003) have observed. After solar radiation because of heating and the unstable stratification of the air masses near the surface, the moist air which becomes warmer rose. Most probably, at the height of the observed layer the relative humidity of the rising air increased considerably. When the aerosols grow consequently their microphysical, optical properties and extinction profiles change (07:59 UTC figure 5.11). Skakalova et al. (2003) explains that the increase of relative humidity and sea salt are two reasons for the increase in aerosol extinction coefficient. The observation shows that the boundary layer height is increasing from 300 m to 600 m approximately between 7:59 to 9.31 UTC. Consequently the aerosol extinction coefficient is increasing.

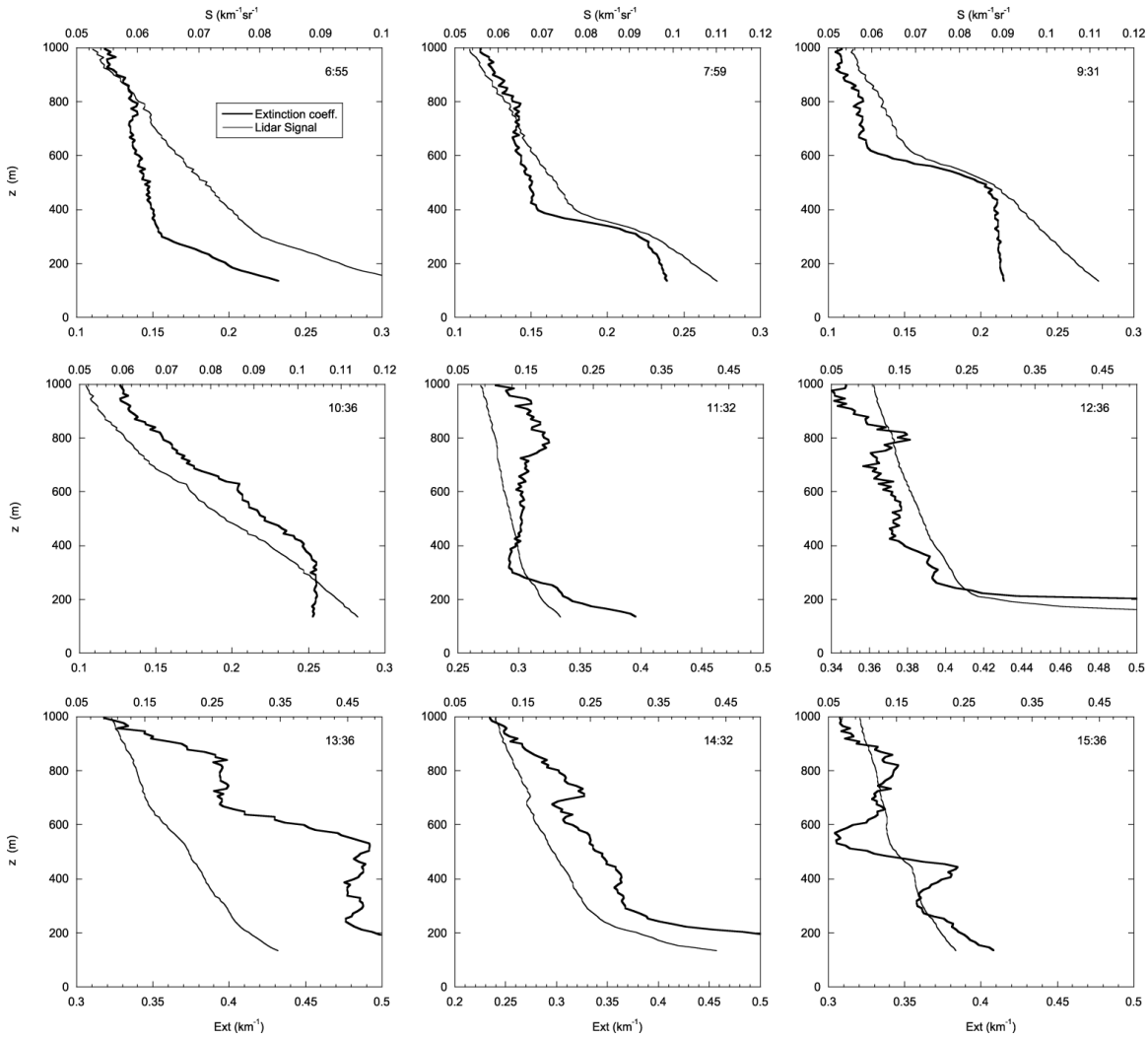

Figure 5.12 Evolution of the aerosol extinction coefficient during the transition period on 25 July at 6:55, 7:59,9:31, 10:36, 11:32,12:36,13:36, 14:32, and 15:36 UTC. In every plot the black is the calibrated Lidar signal and the red one is the extinction coefficient, yaxis is altitue x above axis is the calibrated Lidar signal and extinction coefficient(xbelow axis).

It can be observed that the gradient of extinction coefficient decreases between 9:31 to 10:36 UTC between 450 and 600 m. At 9:31 UTC the layer has extinction coefficient between 0.2 and 0.1 km^{-1} and at 10:36 UTC it changes between 0.24 and 0.2 km^{-1} and extinction coefficient does not vary approximately between 580 and 600, above this layer, it decreases continuously up to 1 km.

Approximately 5 hours after the sunrise temperature in land decreases consequently a change in wind direction is observed. The sea generates the air which is more humid about 30% and is hold back by onshore flow. From 10:36 to 11:32 UTC there is a high decrease in marine boundary layer height which is related to breeze onset. The TIBL development is due to the interaction of complex terrain and sea-breeze circulations (Liu et al., 2001). The diurnal temperature variation is different with height resulting in some diurnal variation in lapse rate above the inversion. Vertical extinction and intensity as well as growth rate of thermal internal boundary layer are characteristic of sea breeze circulation (Melas et al., 1995). It can be observed that this two important parameters have influenced on aerosol extinction profile during the transition proceeding.

At 11:32 UTC we observe that the aerosol relative extinction coefficient increases near to the ground up to 220 m. Two layers of aerosol can be observed below 220 m. We have an extinction coefficient between 0.4 and 0.33 km^{-1} in first layer whereas in second layer the value of extinction coefficient varies between 0.32 and 0.29 km^{-1} and the extinction coefficient increases for some meters between 400 and 430 m and then it is approximately constant above this layer up to 600 m. It is observed that the aerosol extinction coefficient increased in 11:32 UTC in upper layer due to the evolution of boundary layer and sea breeze circulation. Skakalova et al. (2003) have observed a windless layer between the lower and upper layer during and after transition which is due to the temperature increase result in the decrease in the relative humidity. These two factors influence on dissipating the windless layer: about 1 hour after the transition (Figure 5.12 at 12:36 UTC), its thickness decreased from 180 m. After 2h (Figure 10 at 13:36 UTC) it was about 150 m. Comparison between 12:36 and 13:36 UTC shows that after stabilization of the sea breeze extinction coefficient in upper layer is increased but due to Northerly wind the effect of sea breeze is clear on lower layer structure. The extinction coefficient varies from 0.5 to 0.4 km^{-1} in upper layer between 200 and 600 m and from 0.4 to 0.3 km^{-1} between 600 and 1000m. At 13:36 UTC the mixing process approximately becomes complete and it cause an increase in the aerosol extinction coefficient in upper layer. The variations in aerosol relative extinction over the sea surface during the transition period in the late afternoon hours differed considerably from the ones observed during the morning change. During the evening change, above the sea surface the layer with high extinction was considerably deeper; its height reached about 400–600 m. At 14:36 UTC we observed the aerosol extinction coefficient above 650 m increases whereas

because of mixing process in lower layer it decreases between 200 and 600 m. At 15:36 UTC it can be observed three layers of aerosols. A lower layer up to 220 m and above this layer up to 550 m and then from 550 to 1000 m three different layers is shown. The aerosol extinction coefficient increased in upper layer and decrease in lower layer. The aerosol layers are associated to layers of different stability. As the afternoon developed the aerosol join into additional layers which are positioned above the low level layer. This aerosol transport in one side is due to the sea breeze progress other hand is related to mixing process which will be finish by the evening.

5.6 Conclusion

The sea breeze system has a high influence on the transport and diffusion of air pollutants in Dunkerque coastal urban area. During our short period campaign, a set of a backscatter Lidar pulse laser source Nd:YAG at 355 nm, Sun photometer and meteorology parameters have been used for identification and characterization of sea breeze and its special impact on aerosol mass concentration and optical properties. The aerosol mass concentration has a high variability during sea breeze days. On July 23, 24 and 25, 2008 the transition preceding the sea breeze occurred at 09:45, 13:00 and 11.30 UTC. The sea breeze is marked by a sharp increase (between 1 and 4 ms^{-1}) in the wind speed. The wind rotates to north. The sea-breeze period lasts between less than 1 to 4 hours. The temperature drops more than 3 deg. It was found that, because of the steady-state convection from the warmer sea surface, a thermal internal boundary layer (TIBL) forms over the sea in the lowest parts of the land-to-sea flow. The sharp decrease of boundary layer height is related to increase on PM10 mass concentration due to the advection of cool air from the sea. However, the decrease in the BL height is not the only factor influencing the aerosol concentration variation during the sea breeze. The PM10 increase strongly depends on the wind rotation. The case of July 25 clearly shows the influence of the industrial area with a sharp increase in SO_2 concentration and a drop in the PM2.5/PM10 from 0.7 to 0.2. The Lidar signal in the first 200 m is also well correlated to PM10 and to the PM10-PM2.5 hourly variation. A different situation is observed on July 24. The low level Lidar signal is correlated to PM2.5 ground level concentration but not to PM10. As opposite to July 25, during the sea breeze onset the wind rotate N-NE bringing pollution from the downtown city.

We don't have many Sun photometer observations. We can see on July 24 that the amplitude of the coarse and fine modes increases as the AOT increases but the shape of the size distribution remains the same. However, we can note that the mode peaking at 1 µm observed in the morning does not appear in the afternoon. This change in the shape of the distribution might be due to the hygroscopic growth or the settlement of large particles. In the case of atmospheric convective boundary layer, an increase in the value of aerosol extinction coefficient in the lowest layer was observed.

According to Lidar backscatter signal observation it seems that the different circulation of air pollutants before, after and at onset of breeze is experienced. It can be related to change of their physical properties (temperature and water content) and the dynamic and vertical structure of sea breeze during their circulation. In the early morning, aerosols are accumulated in the first few hundred meters of the atmosphere because the nocturnal surface temperature inversion (potential temperature profile region of strong and positive gradient) prevents aerosols that originated near the surface from moving up. During the day, the weak synoptic situation and solar heating help to the development of mesoscale flows and growth of the boundary layer. At the nose of sea breeze front (onset of sea breeze), the denser sea breeze air overruns the less dense land air mass, an occurrence that extend to a height of approximately 150 m. As time passes, the convection progress and the aerosol extinction coefficient has high value in altitude and in low level of atmosphere. The evolution of aerosol is related to dynamic of nose of breeze up to 600 m. In the early afternoon, layers are created when aerosols are injected into the return flow that completes the sea-breeze circulatory cell. As the day progresses and the breeze penetrates further inland, the circulatory cell associated with it grows, and its associated return flow occurs at higher altitudes. Injections of aerosols from the surroundings are added to this return flow. The vertical velocity in sea breeze in less than horizontal velocity, consequently the aerosol is transported horizontally and vertical motion and mixing are not strong. In the afternoon the landward flow causes the formation of an elevated layer of aerosols at about 800 m; aerosols carried aloft by the return flow of the breeze feed this elevated layer. As the afternoon advances, more aerosols are integrated into an additional layer positioned at higher altitudes.

General Conclusion

Clean air is considered to be a basic requirement of human health and well-being. Particulate matter is known to have a significant impact on health. PM concentrations recorded at ground-level reveals the influence of the boundary layer dynamics, local emissions, and advection and mixing of large scale transported aerosols. Thus a global scale monitoring of ground-level PM from satellite-derived aerosol optical measurements remains a challenge. Satellites provide columnar aerosol optical thickness that can be significantly different from the ground-level PM concentration. The link between columnar AOT and ground-level PM depends on the relationship between mass and optical properties and on the vertical distribution of aerosols in the atmosphere.

In this work we have adopted a strategy based on field campaigns for the analysis of atmospheric aerosols optical characteristics and their vertical structure. Presently, the development of aerosol Lidar technology makes it possible to use small, simple devices for field measurements and we have made an extensive use of such devices. Two compact Lidar systems were used: a microJ pulse Lidar (CIMEL) at 532 nm wavelength emission, and a mJ pulse UV Lidar (LEOSPHERE) at 355nm. The general conclusions of the work can be summarized as the answers to three main questions.

What did we observed from the Lidar measurements?

We have used Lidar profiles to detect the mixed layer top in continental and coastal locations. Different methods (gradient, wavelet, non-linear fitting) were compared on a case study and lead to similar results. The MBL top using gradient method was observed as highly variable during the day and from day to day. The classic diurnal growth of the continental PBL was well detected. Moreover, local disturbances like morning fog and sea breeze occurrences are also seen by both instruments. The use of Lidar remote sensing is found to be unavoidable to understand such rapid changes in the aerosol vertical structure. However a full interpretation of the boundary layer dynamics also requires quantitative analysis of meteorological data (temperature, humidity, wind intensity and direction, solar radiation). When the boundary layer is well mixed consequently we have proper profile and we can determine the ABL height with more accuracy. We cannot detect ABL height in case of thick cloud and thin low level cloud makes the detection with low accuracy. The Lidar blind

distance (200 m for the Leosphere and 240 m for the Cimel) may be a strong limitation for investigating very low boundary layer as it can be observed during wintertime, or nocturnal conditions or even sea breeze internal boundary layer. In this case, angular scanning system is required to monitor the surface layer and to analyze the stratification of the boundary layer. Moreover, these observations remain local and are not sufficient to fully describe the 3D structure of the boundary layer at the regional scale, especially in case of sea breeze. In this latter case, the analysis would benefit of a Lidar network.

Both systems are well suitable for the analysis of the distribution of aerosol extinction and backscatter coefficient. The inversion method (following Klett integration method) needs assumption on the Lidar ratio. Using Sun photometer inversions; we were able to estimate the Lidar ratio at 532 nm. We have found 67 sr in Lille during a spring pollution event in 2007 and 77 sr in Dunkerque in winter 2007-2008. These values clearly indicate the predominance of fine particle to scattering properties of the atmosphere. This technique was not possible at 355 nm. The Lidar ratio at 355 nm was then estimated to give the best agreement between the Lidar derived AOT and the Sun photometer measured one. We have found a value of 30 sr in summer at the Dunkerque coastal site. This lower value reveals the influence of the marine aerosol advected by the sea breeze. The retrieved extinction profiles were used to analyze the vertical stratification of aerosol in the low atmosphere. The sea breeze has a significant impact on the extinction profile in the boundary layer. But we did not detect the impact on the atmospheric AOT because the change involved corresponds mainly to a vertical redistribution of aerosol or to an increase of aerosol concentration in the very first hundred meters.

Can we estimate PM using Lidar signal in the lower atmospheric layer?

The Lidar signal in the first hundred meters is found to be well correlated with the ground-level PM measurements. In the Lille urban site, we found an excellent correlation between PM2.5 and low level (225 m high) Lidar signal with R=0.92. This correlation is also observed in the coastal site of Dunkerque with R=0.90. However, under sea breeze condition that advects industrial and marine aerosol, we observe that the low level Lidar signal can be more correlated to PM10 and PM10-PM2.5 difference than PM2.5. These various behaviors reveal that low level Lidar signal evolution must interpreted by accounting for the specific

meteorological features, and the variety and variability of aerosol sources influencing the measuring site.

The direct application of the correlation between Lidar signal and PM is the retrieval from space borne Lidar. A real improvement will come from the use of advanced systems (multi wavelength, Raman or HSRL) that can provide additional information on the aerosol microphysics. The impact of relative humidity on aerosol scattering properties is a burning issue. We have applied a very simple model to account for hygroscopic swelling of particles and increase in the scattering coefficient and we found that it can increase our relationship (R^2= 0.84) between Lidar signal and PM. We also observe that the retrieved aerosol mass scattering coefficient tends to a more realistic value (5.1 m^2/g in winter in Dunkerque) when applying a humidity correction factor. However this latter parameter is deeply dependent on the humidity impact parameterization (in our case we use a power coefficient of 0.55). A further interpretation of correlation between in situ PM and Lidar signal would require much deeper information on the size distribution, chemical composition of particles and their solubility properties.

Can we connect the atmospheric aerosol optical thickness to the ground-level PM?

At the seasonal scale (monthly means) we can observe a significant variability in the AOT to PM relationship which is most probably due to the change in the mixed layer height. At the scale of large pollution event (daily means), the AOT and PM2.5 are fairly correlated. However, the diurnal cycle in the mixed layer height (hourly means) is one of the major processes that impact the AOT-PM relationship. When accounting for the MBL height detected by our Lidar system, we have shown that the correlation is significantly increased. The correlation coefficient changes from R=0.63 to R=0.73 for the experiment in Lille and from 0.77 to 0.9 for the experiment in Dunkerque. Accounting for the MBL height in the AOT-PM relationship needs that the aerosol be homogeneously mixed and that the extent of the PBL be accurately defined. This situation is encountered only during some portion of the day, when the convection processes are active (late morning and early afternoon). More information on the vertical distribution of turbulent fluxes would benefit to the interpretation of the vertical mixing of aerosols in the boundary layer and thus the relationship between ground and PBL integrated PM.

We did not succeed to improve the PM-AOT relationship by estimating the relative contribution of the boundary layer and the free troposphere to the total AOT. First the profile of Lidar ratio remains unknown and we must recall that the relative humidity is not homogeneous vertically and thus the Lidar ratio should change as a function of the range. Moreover, different kind of aerosol can also be present as a function of the altitude. Secondly, the Cimel Lidar has a rather poor overlap function below 1 km and the determination of the overlap function could be a limit for determining the PBL AOT.

The layered vertical distribution of absorbing and non-absorbing troposphere aerosols is important to be considered in local and global scale numerical models. The vertical structure of aerosol extinction coefficient obtained by Lidar can be used to validate the profile simulated by the model. Furthermore, the large uncertainties in model simulations of aerosols chemical properties make difficult to use these models for evaluating aerosol characteristics and forecast their trends. It is necessary to also measure simultaneously parameters like vertical profile of relative humidity or flux to well define the dynamic structure of aerosol in the model.

References

Abbs, D.J., & Physick, W.L. (1992). Sea-breeze observations and modelling: A review. *Aust. Meteorol. Mag, 41*, 7-19

Ackerman, A.S., Toon, O.B., Stevens, D.E., Heymsfield, A.J., Ramanathan, V., & Welton, E.J. (2000). Reduction of tropical cloudiness by soot. *Science, 288*, 1042-1047

Ackerman, J. (1998). The extinction-to-backscatter ratio of tropospheric aerosol: A numerical study. *J. Atmos. Oceanic Tech., 15*, 1043-1050

Allen, G., & Ress, R. (1997). Evaluation o the TEOM method for measurement of ambiant particulate mass in urban areas. *J. Air Waste Manage. Assoc., 47*, 682-689

Aman, M., Cabala, R., Cofala, J., Heyes, C., Klimont, Z., Schöpp, W., Tarrason, L., Simpson, D., Wind, P., & Jonson, J.-E. (2004). CAFE scenario analysis Report Nr.2: The 'current legislation' and the 'Maximum technically feasible reduction' cases for the CAFE baseline emission projections. Background paper for the meeting of the CAFE working group on target setting and policy advice. In: International Institute for Applied Systems Analysis

Ansmann, A., & Müller, D. (2005). Lidar and atmospheric aerosol particle. In C. Weitkamp (Ed.), *LIDAR: Range resolved optical remote sensing of the atmosphere* (pp. 105-141). Geessthacht, Germany: Springer

Ansmann, A., Wagner, F., Althausen, D., Müller, D., Herber, A., & Wandingen, U. (2001). European pollution outbreaks during ACE 2: lofted aerosol plumes observed with Raman lidar at the Portuguese coast. *J. Geophys. Res., 106*, 20,725-720,733

Baars, H., Ansmann, A., Engelmann, R., & Althausen, D. (2008). Continuous monitoring of the boundary-layer top with lidar. *Atmos. Chem. Phys., 8*, 7281-7296

Barbato, J.P. (1975). The sea breeze of the Boston area and its effect on the urban atmosphere. *Ph.D. dissertation, Boston Univ., Boston, Mass., 1975.*

Baron, P.A., & Willeke, K. (2005). *Aerosol measurement: Principles, techniques, and applications*. New-York: Wiley

Bigot, S., Planchon, O. (2003). Identification and characterization of sea breeze days in Northern France using Singular Value Decomposition. *International Journal of Climatology, 23*, 1397-1405

Bodhaine, B.A., Wood, N.B., Dutton, E.G., & Slusser, J.R. (1999). On Rayleigh optical depth calculations. *J. Atmos. Oceanic Tech., 16*, 1854-1860

Bösenberg, J., & et al. (2003). EARLINET: A European aerosol research lidar network to establish an aerosol climatology. In. Hamburg: Max Planck Inst. for Meteorol.

Boubel, R.W., Fox, D.L., Bruce Turner, D., & Stern, A.C. (1994). *Fundamentals of air pollution, third edition*. London, UK: Academic Press

Boyouk, N., Léon, J.-F., Delbarre, H., Podvin, T., & Deroo, C. (2009). Impact of the mixing boundary layer on the relationship between PM2.5 and aerosol optical thickness. *Atmos. Environ., in press*

Brooks, I.M. (2003). Finding boundary layer top: application of a wavelet covariance transform to lidar backscatter profiles. *J. Atmos. Oceanic Tech., 20*, 1092-1105

Bucholtz, A. (1995). Rayleigh-scattering calculations for the terrestrial atmosphere. *Appl. Opt., 34*, 2765-2773

Cattrall, C., Reagan, J., Thome, K., & Dubovik, O. (2005a). Variability of aerosol and spectral lidar and backscatter and extinction ratios of key aerosol types dervied from selected Aerosol Robotic Network locations. *J. Geophys. Res., 110*, 10.1029/2004JD005124

Cattrall, C., Reagan, J., Thome, K., & Dubovik, O. (2005b). Variability of aerosol and spectral lidar and backscatter and extinction ratios of key aerosol types dervied from selected Aerosol Robotic Network locations. *J. Geophys. Res., 110*, 10.1029/2004JD005124

Chazette, P., & Liousse, C. (2001). A case study of optical and chemical ground apportionment for urban aerosols. *Atmos. Environ., 35*, 2497-2506

Chu, D.A., Kaufman, Y.J., Zibordi, G., Chern, J.D., Mao, J., Li, C., & Holben, B.N. (2003). Global monitoring of air pollution over land from the Earth observing system-Terra Moderate imaging spectroradiometer (MODIS). *J. Geophys. Res., 108*, 10.1029/2002JD003179

Cohn, A.S., & Angevine, W.M. (2000). Boundary layer height and entrainment zone thickness measured by lidars and wind-profiling radars. *J. Appl. Meteor., 39*, 1233-1247

Colbeck, I., Chung, M.-C., & Eleftheriadis, K. (2002). Formation and transport of atmospheric aerosol over Athens, Greece. *Water, Air, and soil Pollution: Focus, 2*, 223-235

Damato, F., Planchon, O., & Dubreuil, V. (2003). A remote sensing study of the inland penetration of sea breeze fronts from the English channel. *Weather, 58*, 219-226

Dho, S.W., Park, Y.J., & Kong, H.J. (1997). Experimental determination of a geometric form factor in a lidar equation for an inhomogeneous atmosphere. *Appl. Opt., 36*, 6009-6010

Dockery, D.W., & Pope, C.A.I. (1994). Acute respiratory effects of particulate air pollution. *Annual Review of Public Health 15*, 107-132

Dockery, D.W., Pope III, C.A., Xu, X., Splenger, J.D., Ware, J.H., Fay, M.E., Ferris, B.G., & Speizer, F.E. (1993). An association between air pollution and mortality in Six U.S. cities. *The New England Journal of Medicine, 329*

Dubovik, O., Alexander sinyuk, Tatyana lapyonok, Brent N. Holben (2006). Application of spheroid models to account for aerosol particle nonsphericity in remote sensing of desert dust. *Journal of Geophysical Research, 111*, D11208

Dubovik, O., Holben, B.N., Eck, T.F., Smirnov, A., Kaufman, Y.J., King, M.D., Tanré, D., & Slutsker, I. (2002). Variability of absorption and optical properties of key aerosol types observed in worldwide locations. *J. Atmos. Sci., 59*, 590-608

Dubovik, O., & King, M.D. (2000). A flexible inversion algorithm for retrieval of aerosol optical properties from sun and sky radiance measurements. *J. Geophys. Res., 105*, 20,673-620,696

Dubovik, O., Smirnov, A., Holben, B.N., King, M.D., Kaufman, Y.J., Eck, T.F., & Slutsker, I. (2000). Accuracy assessments of aerosol optical properties retrieved from Aerosol Robotic Network (AERONET) Sun and Sky radiance measurements. *J. Geophys. Res., 105*, 9791-9806

Flamant, C., Pelon, J., Flamant, P.H., & Durand, P. (1997). Lidar determination of the entrainment zone thickness at the top of the unstable marine atmospheric boundary layer. *Boundary-Layer Meteorol., 83*, 247-284

Forster, P., Ramaswamy, V., Artaxo, P., Berntsen, T., Betts, R., Fahey, D.W., Haywood, J.M., Lean, J., Lowe, D.C., Myhre, G., Nganga, J., Prinn, R., Raga, G., Schulz, M., & Van Dorland, R. (2007). Changes in atmospheric constituents and in radiative forcing. In S. Solomon, D. Qin, M. Manning, Z. Chen, M. Marquis, K.B. Averyt, M. Tignor & H.L. Miller (Eds.), *Climate change 2007: The physical basis. Contribution of Working group I to the fourth assessment report of the Intergovernmental panel on climate change*. Cambridge, United Kingdom and New York, NY, USA: Cambridge University Press

Franke, K., Ansmann, A., Müller, D., Althausen, D., Wagner, F., & Scheele, R. (2001). One-year observations of particle lidar ratio over the tropical Indian Ocean with Raman lidar. *Geophys. Res. Lett., 28*, 4559-4562

Gangoiti, G., Alonso, L., Navazo, M., Albizuri, A., Perez- Landa, G., Matabuena, M., Valdenebro, V., Maruri, M., Garcia, J.A., & Millan, M.M. (2002). Regional transport of pollutants over the Bay of Biscay: Analysis of an ozone episode under a blocking anticyclone in west-central Europe. *Atmos. Environ., 36*, 1349-1361

Georgieva, E., Canepa, E., & Builtjes, P. (2007). Harbours and air quality. *Atmos. Environ., 41*, 6319-6321

Gupta, P., & Christopher, S.A. (2009). Particulate matter air quality assessment using integrated surface, satellite, and meteorological products: Multiple regression approach. *J. Geophys. Res, 114*, doi:10.1029/2008JD011496

Gupta, P., Christopher, S.A., Wang, J., Gehrig, R., Lee, Y., & Kumar, N. (2006). Satellite remote sensing of particulate matter and air quality assessment over global cities. *Atmos. Environ., 40*, 5880-5892, 10.1016/j.atmosenv.2006.03.016

Hand, J.L., & Malm, W.C. (2007). Review of aerosol mass scattering efficiencies from ground-based measurements since 1990. *J. Geophys. Res., 112*, doi:10.1029/2007JD008484

Hänel, G. (1976). The properties of atmospheric aerosol particles as functions of the relative humidity at thermodynamic equilibrium with surrounding moist air. *Adv. in Geophys., 19*, 73-188

Hansen, J., Sato, M., & Ruedy, R. (1997). Radiative forcing and climate response. *J. Geophys. Res, 102*, 6831-6864

Hoff, R.M., & Christopher, S.A. (2009). Remote sensing of Particulate Pollution from Space: Have we reached the promised land ? *J. Air Waste Manage. Assoc., 59*, 645-675

Holben, B.N., Eck, T.F., Sluster, I., Tanré, D., Buis, J.P., Setzer, A., Vermote, E., Reagan, J.A., Kaufman, Y.J., Nakajima, T., Lavenu, F., Jankowiak, I., & Smirnov, Z. (1998). AERONET-A federated instrument network and data archive for aerosol characterisation. *Rem. Sens. Environ., 66*, 1-16

Holben, B.N., Tanré, D., Smirnov, A., Eck, T.F., Slutsker, I., Abuhassan, N., Newcomb, W.W., Schafer, J.S., Chatenet, B., Lavenu, F., Kaufman, Y.J., Vande Castle, J., Setzer, A., Markham, B., Clark, D., Frouin, R., Halthore, R., Karneli, A., O'Neill, N.T., Pietras, C., Pinker, R.T., Voss, K., & Zibordi, G. (2001). An emerging ground-based aerosol climatology: Aerosol optical depth from AERONET. *J. Geophys. Res., 106*, 12,067-012,097

IDEM (2001). *Risk Integrated system of closure technical guide*: Indiana Department of Environmental Management

Janhäll, S., Olofson, F.G., Andersson, P.U., Petterson, J.B.C., & Hallquist, M. (2006). Evolution of the urban aerosol during winter temperatire inversion episodes. *Atmos. Environ., 40*, 5355-5366

Jeong, M.-J. (2007). Effect of aerosol humidification on the column aerosol optical thickness over the Atmospheric Radiation Measurement Southern Great Plains site. *J. Geophys. Res, 112*, doi:10.1029/2006jd007176

Kacenelenbogen, M. (2008), Application de la télédétection spatiale à la surveillance de la pollution en aérosols, 181 pp, Université de Lille 1, Villeneuve d'Ascq, France.

Kacenelenbogen, M., Léon, J.-F., Chiapello, I., & Tanré, D. (2006). Characterization of aerosol pollution events in France using ground-based and POLDER-2 satellite data. *Atmos. Chem. Phys., 6*, 4843-4848-4849

Kaufman, Y.J., Tanré, D., & Boucher, O. (2002). A satellite view of aerosols in the climate system. *Nature, 419*, 215-223

King, M., Byrne, D., Herman, B. and reagan, J. (1978). Aerosol size distribtion obtained of spectral depth measurement. . *J. Atmos. Sci, 35*, 2153-2167

King, M.D., Kaufman, Y.J., Tanré, D., & Nakajima, T. (1999). Remote sensing of tropospheric aerosols from space: past present and future. *Bull. Amer. Meteor. Soc., 80*, 2229-2259

Kitada, T. (1987). Turbulence structure of sea breeze front and its implication in air pollution transport—Application of k-e turbulence model. *Boundary Layer Meteorol., 41*, 217-239

Klett, J.D. (1981). Stable analytical inversion solution for processing lidar return signal. *Appl. Opt., 20*, 211-220

Klett, J.D. (1985). Lidar inversion with variable backscatter/extinction ratios. *Appl. Opt., 24*, 1638-1643

Kotchenruther, R.A., & Hobbs, P.V. (1998). Humidification factors of aerosols from biomass burning in Brazil. *J. Geophys. Res., 103*, 32081-32089

Künzly, N., Kaier, R., Medina, S., Studnicka, M., Chanel, O., Filliger, P., Herry, M., Horak, F., Puybonnieux-Texier, V., Quénel, P., Schneider, J., Seethaler, R., Vergnaud, J.-C., & Sommer, H. (2000). Public-health impact of outdoor and traffic-related air pollution: a European assessment. *The Lancet, 356*, 795-801, 10.1016/S0140-6736(00)02653-2

Lammert, A., & Bösenberg, J. (2006). Determination of the convective boundary layer height with laser remote sensing. *Boundary-Layer Meteorol., 119*, 159-170

Leriche, P., Kergomard, C., & Chapelet, P. (1998). Etudes des brises de mer sur le littoral français de la mer du Nord. *Publications de l'association internationale de climatologie, 11*, 107-114

Lin, C.-H., Lai, C.-H., Wu, Y.-L., Lin, P.-H., & Lai, H.-C. (2007). Impact of sea breeze air masses laden with ozone on inland surface ozone concentrations: A case study of the northen coast of Taiwan. *J. Geophys. Res., 112*, doi:10.1029/2006JD008123

Lin, C.-Y., Liu, S.C., Huang, S.-J., Liu, C.-M., Kuo, C.-H., & Young, C.-Y. (2005). Long-range transport of aerosols and their impact on the air quality of Taiwan. *Atmos. Environ., 39*, 6066-6076

Liu, H., Chan, J.C.L., & Cheng, A.Y.S. (2001). Internal boundary layer structure under sea-breeze conditions in Hong Kong. *Atmos. Environ., 35*, 683-692

Liu, Y., Park, R.J., Jacob, D.J., Li, Q., Kilaru, V., & Samat, J.A. (2004). Mapping annual mean ground-level PM2.5 concentrations using multiangle imaging spectroradiometer

aerosol optical thickness over the contiguous United States. *J. Geophys. Res., 109*, 10.1029/2004JD005025

Lolli, S., Welton, E.J., & Sauvage, L. (2008). EZ LIDAR measurement results in the frame of Indian Monsoon TIGER-Z NASA campaign. In, *SPIE* (p. 71110I). Cardiff, U.K.

Mattis, I., Ansmann, A., Müller, D., Wandinger, U., & Althausen, D. (2004). Multiyear aerosol observations with dual-wavelength Raman lidar in the framework of EARLINET. *J. Geophys. Res., 109*, 10.1029/2004JD004600

Mayer, H. (1999). Air pollution in cities. *Atmos. Environ., 33*, 4029-4037

McCormick, M.P. (2005). Airborne and spaceborne lidar. In C. Weitkamp (Ed.), *LIDAR: Range resolved optical remote sensing of the atmosphere* (pp. 355-397). Geessthacht, Germany: Springer

Melas, D., Ziomas, I.C., & Zerefos, C.S. (1995). Boundary layer dynamics in an urban coastal environment under sea breeze conditions. *Atmos. Environ., 29*, 3605-3617

Menut, L., Flamant, C., Pelon, J., & Flamant, P.H. (1999). Urban boundary-layer height determination from lidar measurements over the Paris area. *Appl. Opt., 38*, 945-954

Miller, S.T.K., Keim, B.D., Talbot, R.W., & Mao, H. (2003). Sea breeze: structure, forecasting, and impacts. *Rev. Geophys., 41*, 1011

Moorthy, K.K., Murthy, B.V.K., & Nair, R.P. (1992). sea-breeze front effects on boundary layer aerosols at a tropical coastal station. *J. Appl. Meteorol, 32*, 1196-1205

Müller, D., Ansmann, A., Mattis, I., Tesche, M., Wandingen, U., Althausen, D., & Pisani, G. (2007). Aerosol-type dependent lidar ratios observed with Raman lidar. *J. Geophys. Res., 112*, doi:10.1029/2006JD008292

Murayama, T., Okamoto, H., Kaneyasu, N., Kamataki, H., & Miura, K. (1999). Application of lidar depolarization measurement in the atmospheric boudanry layer: Effects of dust and sea-salt particles. *J. Geophys. Res, 104*, 31,781-731,792

Oke, T. (1978). *Boundary layer climate, second edition*. London, UK: Methuen

Patashnick, H., & Rupprecht, E.G. (1991). Continuous PM10 measurements using the tapered element oscillating microbalance. *J. Air Waste Manage. Assoc., 41*, 1079-1083

Pelletier, B., Santer, R., & Vidot, J. (2007a). Retrieving of particulate matter from optical measurements: a semiparametric approach. *J. Geophys. Res., 112*, 10.1029/2005JD006737

Pelletier, B., Santer, R., & Vidot, J. (2007b). Retrieving of particulate matter from optical measurements: a semiparametric approach. *J. Geophys. Res., 112*, doi:10.1029/2005JD006737

Pelon, J., Mallet, M., Mariscal, A., Goloub, P., Tanré, D., Bou Karam, D., Flamant, C., Haywood, J.M., Pospichal, B., & Victori, S. (2008). Microlidar observations of biomass burning aerosol over Djougou (Benin) during African Monsoon Multidisciplinary Analysis Special Observation Period 0: Dust and Biomass Burning Experiment. *J. Geophys. Res., 113*, doi:10.1029/2008JD009976

Penner, J.E., Andreae, M.O., Annegarn, H.J., Barrie, L., Feichter, J., Hegg, D.A., Jayaraman, A., Leaitch, R., Murphy, D., Nganga, J., & Pitari, G. (2001). Aerosols, their direct and indirect effects. In J.T.H.e. al. (Ed.), *Climate change 2001, the scientific basis. Contribution of the working group I to the third assessment report of the intergovernmental panel on climate change* (pp. 289-348). Cambridge, United Kingdom and New York, NY, USA

Pope III, C.A., Dockery, D.W., & Schwartz, J. (1995). Review of epidemiological evidence of health effects of particulate air pollution. *Inhalation Toxicology, 7*, 1-18

Querol, X., Alastuey, A., Ruiz, C.R., Artinano, B., Hansson, H.C., Harrison, R.M., Buringh, E., Ten Brink, H.M., Lutz, M., Bruckmann, P., Straehi, P., & Schneider, J. (2004). Specification and origin of PM10 and PM2.5 in selected European cities. *Atmos. Environ., 38*, 6547-6555

Raut, J.C., & Chazette, P. (2007). Retrieval of aerosol complex refractive index from a synergy between lidar, sunphotometer and in situ measurements during LISAIR experiment. *Atmos. Chem. Phys., 7*, 2797-2815

Raut, J.C., & Chazette, P. (2008). Vertical profiles of urban aerosol complex refractive index in the frame of ESQUIF airborne measurements. *Atmos. Chem. Phys., 8*, 901-919

Rimetz-Planchon, J., Perdrix, E., Sobanska, S., & Brémard, C. (2008). PM10 air quality variations in an urbanized and industrialized harbor. *Atmos. Environ., 42*, 7274-7283

Romero, H., Ihl, M., Rivera, A., Zalazor, P. and Azacar, P. (1999). Rapid urban growth, land-use changes and air pollution in Santiago, Chile. *Atmos. Environ.*, 4039-4017

Rotach , M.W., Gryning, S.E., Batchvarova, E., Christen, A., & Vogt, R. (2004). Pollutant dispersion close to an urban surface - the BUBBLE tracer experiment *Meteorol. Atm. Phys. , 87*, 39-56

Rotach, M.W., Vogt, R., Bernhofer, C., Batchvarova, E., Christen, A., Clappier, A., Feddersen, B., Gryning, S.-E., Martucci, G., Mayer, H., Mitev, V., Oke, T.R., Parlow, E., Richner, H., Roth, M., Roulet, Y.-A., Ruffieux, D., Salmond, J.A., Schatzmann, M., & Voogt, J.A. (2005). BUBBLE – an Urban Boundary Layer Meteorology Project. *Theor. Appl. Climatol., 81*, 231-261

Russel, P.B., & Heintzenberg, J. (2000). An overview of the ACE-2 clear sky column closure experiment (CLEARCOLUMN). *Tellus B, 52*, 463-483

Schaap, M., Apituley, A., Timmermans, R.M.A., Koelemeijer, R.B.A., & de Leeuw, G. (2008). Exploring the relation between aerosol optical depth and PM2.5 at Cabauw, the Netherlands. *Atmos. Chem. Phys., 9*, 909-925

Schutz, B.E., Zwally, H.J., Shuman, C.A., Hancock, D., & Dimarzio, J.P. (2005). Overview of the ICESat mission. *Geophys. Res. Lett., 32*, doi:10.1029/2005GL024009

Schwartz, J., et al. (2003). Morbidity and mortality among elderly residents of cities with daily PM measurements. . In, *Revised analysis of time-series of air pollution and health* (pp. 25-58). Boston, MA: Health Effect Institute

Seibert, P., Beyrich, F., Gryning, S.-E., Joffre, S., Rasmussen, A., & Tercier, P. (2000). Review and intercomparison of operational methods for the determination of the mixing height. *Atmos. Environ., 34*, 1001-1027

Seinfeld, J.H., & Pandis, S.N. (2006). *Atmospheric chemistry and physics: from air pollution to climate change, second edition*. Hoboken, N.J.: J. Wiley & Sons

Shettle, E.P., & Fenn, R.W. (1979). Models for the aerosols of the lower atmosphere and the effects of humidity variations on their optical properties. In. Hanscomb, Mass.: U.S. Air Force Geophysics Laboratory

Shinozuka, Y., Clarke, A.D., Howell, S., Kapustin, V.N., McNaughton, C.S., Zhou, J., & Anderson, B.E. (2007). Aircraft profiles of aerosol microphysics and optical properties over North America: Aerosol optical depth and its association with PM2.5 and water uptake. *J. Geophys. Res., 112*, 10.1029/2006JD007918

Simpson, J.E. (1994). *Sea Breeze and Local Wind*. New York: Cambridge Univ. Press

Skakalova, T.S., Savov, P.B., Grigorov, I.V., & Kolev, I.N. (2003). Lidar observation of breeze structure during the transition periods at the southern Bulgarian Black Sea coast. *Atmos. Environ., 37*, 299-311

Sloane, C.S. (1984). Optical properties of aerosols of mixed composition. *Atmos. Env., 18*, 871-878

Steyn, D.G., Baldi, M., & Hoff, R.M. (1999). The detection of mixed layer depth and entrainment zone thickness from lidar backscatter profiles. *J. Atmos. Oceanic Tech., 16*, 953-959

Stull, R.B. (1988). *An introduction to boundary layer meteorology* Dordrecht: Kluwer Academic Publishers

Talbot, C., Augustin, P., Leroy, C., Willart, V., Delbarre, H., & Khomenko, G. (2007). Impact of a sea breeze on the boundary-layer dynamics and the atmospheric stratification in a coastal area of the North Sea. *Boundary-Layer Meteorology, 125*, 133-154

Tanré, D., Bréon, F.-M., Deuzé, J.-L., Herman, M., Goloub, P., Nadal, F., & Marchand, A. (2001). Global observation of anthropogenic aerosols from satellite. *Geophys. Res. Lett., 28*, 4555-4558

Van Dingenen, R., Raes, F., & et al. (2004). A European aerosol phenomology - 1: physical characteristics of particulate matter at kerbside, urban, rural and background sites in Europe. *Atmos. Environ., 38*, 2561-2577

Van Donkelaar, A., Martin, R.V., & Park, R.J. (2006). Estimating ground-level PM2.5 using aerosol optical depth determined from satellite remote sensing. *J. Geophys. Res., 111*, 10.1029/2005JD006996

Verma, S., Boucher, O., Venkataraman, C., Reddy, M.S., Müller, D., Chazette, P., & Crouzille, B. (2006). Aerosol lofting from sea breeze during the Indian Ocean Experiment. *J. Geophys. Res, 111*, doi: 10.1029/2005JD005953

Veselovskii, I., Kolgotin, A., Griaznov, V., Müller, D., Wandingen, U., & Whiteman, D.N. (2002). Inversion with regularization for the retrieval of tropospheric aerosol parameters from multiwavelength lidar sounding. *Appl. Opt., 41*, 3685-3699

Wang, H., Bi, X., Sheng, G., & Fu, J. (2006). Chemical composition and sources of PM10 and PM2.5 aerosols in Guangzhou, China. *Environmental Monitoring and Assessment, 119*, 425-239

Wang, J., & Christopher, S.A. (2003a). Intercomparison between satellite-derived aerosol optical thickness and PM2.5 mass: Implications for air quality studies. *Geophys. Res. Lett., 30*, doi:10.1029/2003GL018174

Wang, J., & Christopher, S.A. (2003b). Intercomparison between satellite-derived aerosol optical thickness and PM2.5 mass: Implications for air quality studies. *Geophys. Res. Lett., 30*, 2095, 10.1029/2003GL018174

Wang, M., & Gordon, H.R. (1995). Estimation of aerosol columnar size distribution and optical thickness from the angular distribution of radiance exiting the atmosphere: simulations. *Appl. Opt., 34*, 6489-7001

Whiteman, D.N., Melfi, S.H., & Ferrare, R.A. (1992). Raman lidar system for the measurement of the water vapor and aerosols in the Earth's atmosphere. *Appl. Opt., 31*, 3068-3082

Wiegner, M., Emeis, S., Freudenthaler, V., Heese, B., Junkermann, W., Münkel, C., Schäfer, K., Seefeldner, M., & Vogt, S. (2006). Mixing layer height over Munich, Germany: Variability and comparisons of different methodologies. *J. Geophys. Res., 111*, doi:10.1029/2005JD006593

Winker, D.M., Couch, R.H., & McCormick, M.P. (1996). An overview of LITE: Nasa's Lidar In-space Technology Experiment. *Proc. IEEE, 84*, 164-180

Winker, D.M., Pelon, J., & McCormick, M.P. (2003). The CALIPSO mission: spaceborne lidar for observation of aerosol and clouds. In, *SPIE* (pp. 1-11)

World Health Organization (2006). *Air quality guidelines - global update 2005*. Copenhagen, Denmark: WHO Regional office for Europe

Wöste, L., Wedekind, C., Wille, H., Rairoux, P., Stein, B., Nikolov, S., Werner, C., Niedermeier, S., Schillinger, H., & Sauerbray, R. (1997). Femtosecond atmospheric lamp. *Laser und Optoelectronik, 29*, 51-53

Wyngaard, J.C. (1990). Scalar fluxes in the planetary boundary layer- theory, modeling and measurement *Boundary Layer Meteorol., 50*, 49-75

Yu, H., Liu, S.C., & Dickerson, R.E. (2002). Radiative effects of aerosols on the evolution of the atmospheric boundary layer. *J. Geophys. Res, 107*, doi: 10.1029/2001JD000754

Table of figures

Annex: Aerosol characterization and transport path-way using ground-based measurement and space borne remote sensing

Neda Boyouk, Jean- François Léon and Hervé Delbarre

Remote sensing of clouds and the Atmosphere XII, edited by Richard H. Picar, Adolfo Comeron, Aldo Amodeo, Michiel Van Weele, Proc. Of SPIE Vol. 7107, 71070Y, doi:10.1117/12.810867, 2008.

ABSTRACT

Using two years of measurements of aerosol extinction coefficient retrieval from CALIPSO (http://www-CALIPSO.larc.nasa.gov) as a joint NASA-CNES satellite mission along with ground-based measurements of particle mass concentration (PM2.5), we assess particulate matter air quality over different urban and periurban areas in France. In order to understand the influence of the long range transport onto the local aerosol load we have focused on analysis of pollution event in Lille - urban area and Dunkerque - industrial area. We compared ground-based measurements with CALIPSO measurements. The CALIPSO level 2 aerosol records are more useful because the extinction coefficient is available. We use the extinction coefficient profiles which are provided by CALIPSO to depict the vertical structure of the aerosol properties. The combination of ground-based measurements of PM2.5, aerosol optical thickness (AOT's) obtained by Aeronet network data (http://aeronet.gsfc.nasa.gov) and CALIOP data enhances the possibilities of studying transport pathway of aerosol in the atmosphere and aerosol optical properties (aerosol extinction coefficient, aerosol optical depth, atmosphere transparency). The linear relationship between the AOT _CALIPSO and AOT _ Aeronet network shows a slope of 0.4 in north of France. Moreover, we observed the good relationship between PM2.5 and AOT by CALIPSO profiles with a slope of 57.59 and correlation coefficient of 0.75 over France.

1. Introduction

Determining and quantifying the spatial and temporal distribution of the atmospheric aerosols is critical for climate change studies. Because of the short lifetime of aerosol chemical compositions and the corresponding strong spatial variations of satellite and ground-based measurements can be very helpful in characterizing the properties of aerosols on large time and space scales as required by global models.

Almost half of the present world's population lives in urban areas. Particle matters are one of the major pollutants that affect air quality in urban and even in rural areas of the world. To understand the effect of PM on the earth's climate system and human health it is necessary to routinely monitor PM2.5 (particulate matter with diameter less than 2.5µm) on a global basis. Air quality has been widely monitored at the surface through ground–based monitors. These monitors are used to characterize air quality and to determine compliance with ambient air quality standards. Even these ground based measurements represent point measurements and do not have the necessary coverage to map the regional to global distribution of aerosols [1].

Space borne active remote sensing of atmospheric aerosol is the key to provide observations that are needed to better understand a variety of aerosol – radiation- climate feedback processes in regional and global scale [2]. The vertical structure of aerosol optical parameters is important to understand and estimate the vertical distribution of pollutants within the layer above the base of the temperature inversion, the role of surface pollutant on higher level of atmosphere and the role of large scale transport on the local aerosol load. The elevated pollution layers are important to understand, since the contaminants trapped within them may be fumigated to lower levels during the same day or on subsequent days as the boundary layer deepens due to convective thermals generated by surface heating. This deepening in turn causes a more rapid build up of pollutant concentrations at the surface than might be expected. Such fumigation may occur near the origin of the elevated layer or another location depending on the kinematics of the boundary layer structure [3].

The objective of this work is to study the aerosol characterization, and their vertical structure. In addition we aim to quantify the role of local as well as large scale trans-boundary atmospheric circulation on the total aerosol load and its spatial and temporal distribution.

2. Instruments and methods

In this study the particle mass concentration of fine aerosol (PM2.5) are obtained from data archive of Air quality agencies French Environment and Energy Management Agency (ADEME; http://www.atmonet.org). Automatic stations provide us the hourly average of PM2.5 for the urban and periurban and traffic stations. Aerosol optical thickness was obtained by sun photometers of the Aeronet network. CALIPSO extinction coefficients and aerosols layer height of CALIPSO data is used to compare with ground and sun photometer measurement.

2.1 CALIPSO

CALIPSO is designed to provide vertical distribution and optical and physical properties of aerosol and clouds in the atmosphere. CALIPSO which has a large volume of Lidar profile data received each day (~1.74 million shots) was launched into a sun synchronous orbit at an altitude of 705 km and inclination of 98.2° on 28 April 2006. The backscatter profiles and extinction coefficient which are used from Level 2 profiles are averaged over 40km or 5 km horizontally.

2.2 Sun photometer

The measurement of aerosol optical properties was made by Cimel sun photometers, which are a part of AERONET global network. These instruments are described in detail by Holben [4]. The automatic –tracking sun and sky scanning radiometers make direct sun measurement with a 1.2° full field of view at least every 15 min at four wavelengths (440, 670, 870, 1020nm). These solar extinction measurements are then used to compute aerosol optical properties at each wavelength. The aerosol optical thickness is calculated at 532 nm wavelength to compare with CALIPSO extinction coefficient at the same wavelength.

2.3 TEOM

Tapered element oscillating microbalance (TEOM) measures the PM2.5. This measures the change in resonant frequency of the oscillating filter that gets loaded with particles. These

measurements provide us the hourly average of fine particle mass concentration in urban and periurban stations over France.

2.4 Geographical locations

This study is carried out over France. In addition, two cities Lille and Dunkerque have been chosen for the study of the influence of long range transport on local aerosol load considering different source of aerosol pollution in each city. Lille and Dunkerque are located in different geographical and meteorological situation. Lille (50.61°N, 3.14° E) is an urban area 220 km far from Paris. Dunkerque (51.38°N, 2.37° E) is an industrial city next to the sea at a distance of 80 km from Lille.

2.5 Methods

There are a number of effective methods for deriving particulate extinction and backscatter coefficients from the signals measured by elastic-backscatter Lidars. For CALIOP, effective approaches need to consider situations where the particulate attenuation is usually significant and variable. The algorithms and formulae that have been used to solve the Lidar equation fall broadly into two classes. First, the iterative methods were developed for the analysis of searchlight data on aerosols in the upper atmosphere. Second, analytical formulae developed for the analysis of rainfall radar data and based on the solution to the Bernoulli equation were also adopted by Lidar researchers. These, so called, single-component solutions only consider one atmospheric scattering component and are not applicable to situations where molecular and particulate scattering might be comparable in magnitude. Two-component analytical solutions were developed for these situations [5, 6].

For an elastic backscatter Lidar system as used in CALIPSO, the retrieval of profiles of particulate backscatter and extinction involves the solution of the Lidar equation as following where P(r) is detected backscatter signal from range r from Lidar , ξ: Lidar system parameter, E_0 average laser energy for single shot, $\beta_M(r)$ Molecular volume backscatter coefficient, $T_M^2(0,r)$ two way transmittance between Lidar and range r, $\sigma_M(r)$ Molecular volume extinction coefficient, S_M; molecular extinction to back scatter ratio, $\beta_P(r)$; particular volume backscatter coefficient, $T_p^2(0,r)$; Particular two way transmittance, $\tau_P(0,r)$; Particulate optical

thickness, $\sigma_P(r)$; particulate volume extinction coefficient, S_P ;particulate extinction to backscatter coefficient , and multiple scatter factor is $\eta(r)$.

$$P(r) = \frac{1}{r^2} E_0 \xi [\beta_M(r) + \beta_P(r)] T_M^2(0,r) T_{O3}^2(0,r) T_P^2(0,r) \quad (1)$$

$$T_M^2(O,r) = \exp[-2\int_0^r \sigma_M(r')dr'] \quad (2)$$

$$\sigma_M(r) = S_M \beta_M(r) \quad (3)$$

$$T_P^2(O,r) = \exp[-2\eta(r)\tau_P(0,r)] \quad (4)$$

$$\tau_P(0,r) = \int_0^r \sigma_P(r')dr' = S_P \int_0^r \beta_P(r')dr' \quad (5)$$

$$\sigma_P(r) = S_P \beta_P(r) \quad (6)$$

It can be seen that the Lidar equation cannot be solved without ancillary information like molecular number density. For operations at the CALIPSO wavelengths (532 nm and 1064 nm), the molecular number density and ozone absorption coefficient profiles must be known. For CALIPSO, these are obtained from meteorological analyses produced by NASA's Global Modeling and Assimilation Office (GMAO). A key aspect of CALIPSO analysis system is that it uses an innovative nested multi-grid averaging scheme to process a composite Lidar 'scene'. Scenes are segments of what are commonly referred to as CALIPSO curtain files.

For CALIOP, effective approaches need to consider situations where the particulate attenuation is usually significant and variable. The CALIOP level 2 processing system is composed of three modules and performing extinction retrievals which have the general function of detecting layers, classifying these layers by type, and performing extinction retrieval. These three modules are Selective Iterated BoundarY Locator (SIBYL), Scene Classifier Algorithm (SCA) and Hybrid Extinction Retrieval Algorithms (HERA). Level 2 Lidar processing begins with SIBYL operating on a sequence of scenes. It consist of segments of Level 1 data covering 80 km in along-track distance, corresponding to a collection of 240 consecutive, single-shot profiles. The module averages these profiles to

horizontal resolutions of 5, 20, and 80 km, consisting of averages of 15, 60, and 240 profiles, respectively, and detects features at each of these resolutions. The SCA module then classifies these generic features as clouds or one of five aerosol types, based primarily on scattering strength and the spectral dependence of the Lidar attenuated backscatter. The module can further discriminate between ice/water clouds by relying on the layer-averaged Lidar depolarization ratio and ancillary information such as altitude and temperature. The SCA module also uses a combination of observed parameters and *a priori* information to select appropriate values for the initial Lidar ratios and multiple scattering factors required for retrieving extinction and optical thickness by HERA. These automated analysis techniques are able to identify different optical properties of cloud and aerosol features (e.g., the particulate extinction-to-backscatter –ratio, also commonly known as the Lidar ratio) over different regions of the globe as well as within the same column [7, 8].

To compare ground-based to space-based measurements, it's a whole lot easier to use the level 2 data products. Exact matches between ground-based and space-based platforms are almost non-existent, so a statistical analysis of derived properties is the best approach. We get a reasonable estimate of the optical depth using the integration of the extinction coefficient of aerosol from CALIPSO profiles. Since AERONET reports a column optical depth, the most straightforward comparison to CALIPSO is provided by integrating the extinction coefficient profile products to get the CALIPSO estimate of column aerosol optical depth. The objective of the combination of ground base measurement and space borne measurement is to understand the role of long range transport of aerosol in local aerosols load.

3. Results

3.1 Aerosol optical properties obtained by CALIPSO profiles

The extinction coefficient is a fundamental parameter on which the transfer pathway of aerosol may be based. Also aerosol physical characteristics such as number density or mass concentration are more closely related to the extinction coefficient than the backscatter coefficient [9].

The vertical structure of particulate extinction coefficients by space-borne elastic-backscatter Lidar CALIOP provides us more knowledge about aerosol optical properties in

the different levels of the troposphere. CALIOP, as LITE (Lidar In space Technology Experiment) and GLAS (laser altimeter to measure ice sheet topography), backscatter Lidar, cannot provide direct measurement of back scatter and extinction profiles [10]. Aerosol optical parameters like the extinction coefficient and backscatter coefficient are obtained by two components method [5, 11]. The single scattering and other developed method for multiple scattering [12, 13] are applied for retrieval of CALIPSO data (Level 2- 40 km).

Lidar level 2-40km aerosol profiles have the spatial resolution of 120m vertically and it is average over 40 km. The profiles of the aerosol extinction coefficient were obtained from level2-40 km of CALIPSO data between 2006 and 2008. The time interval of these records covered of half orbit (day and night). The vertical resolution varies for upper layers of atmosphere.

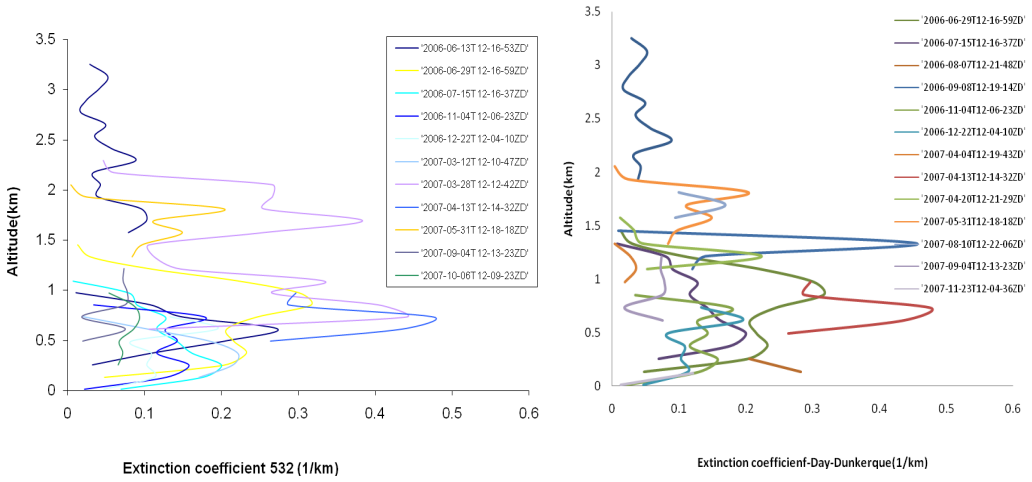

(a)Lille (b)Dunkerque

Fig.1 Daytime vertical profiles of extinction_coefficieint_532 (a) Lille (b)Dunkerque

Figures 1(a) and 1(b) show the extinction coefficient_532 profile obtained by level 2-40 km CALIPSO data at the time of CALIPSO trace near to Lille and Dunkerque. The nearest distance between the CALPSO trace (center of a pixel) and Lille or Dunkerque is less than 30km. The aerosol layer exceeds 3.5 km in the day time profiles. The maximums of the

aerosols extinction coefficient are observed just less than 2km. For these two years of observation, the highest values of the aerosol extinction coefficients have been observed in the boundary layer (less than 2 km).

Figures 2(a) and 2(b) show the night time profile of the aerosols extinction coefficient in Lille and Dunkerque. By comparison Lille and Dunkerque the highest extinction coefficients are observed in 367 m and 247 m respectively. In Lille aerosol layer are observed up to 5.5 km whereas they are only to 3.5 km in Dunkerque. The night time profiles are more accurate than day time profiles. For the day time profile the background noise is dominated by direct or scattered sun light whereas at night time it is due to the moon and stars. The aerosol layer altitude is influenced by seasonal variation, the metrological situation and limit of existence of data, as well as the accuracy of data (existence of noise).

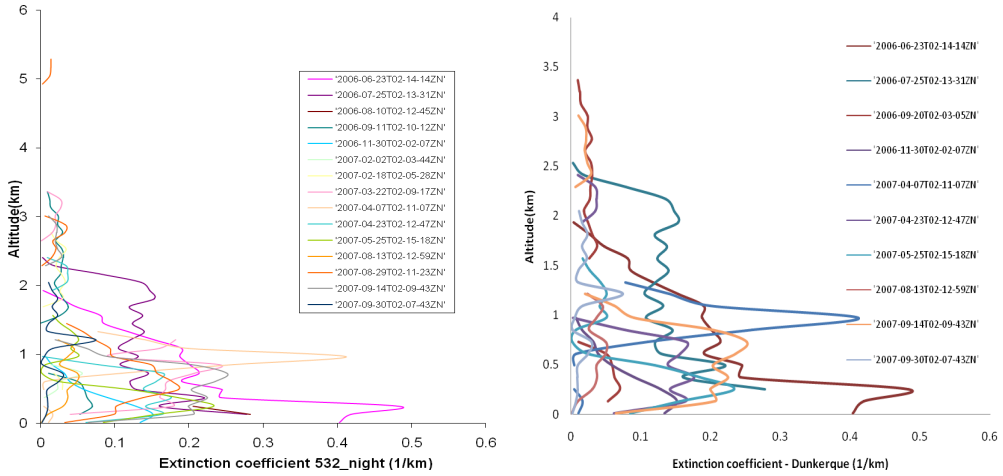

Fig.2 Night time vertical structure of extinction_coefficeint_532 (a) Lille (b) Dunkerque

Because of the geographical and meteorological conditions in Dunkerque, the boundary layer top is lower by comparison to Lille. The aerosol layers appear in higher altitude when there is long range transport. In some unstable meteorological situations with vertical wind speed and intensive turbulence the aerosols have transferred to upper layer.

3.2 Comparison of Aerosol optical thickness obtained by CALIPSO and Aeronet data

We have compared AOT of CALIOP profiles and AOT of Aeronet data at the north of France in Lille and Dunkerque between 2006 and 2008. The AOT's of CALIPSO are obtained by integration of extinction coefficient at 532 nm wavelength. The CAlIPSO overpass traces and PM2.5 automatic stations have a distance of less 30 km. Lille (urban) and Dunkerque (urban-industrial) have different sources of pollution.

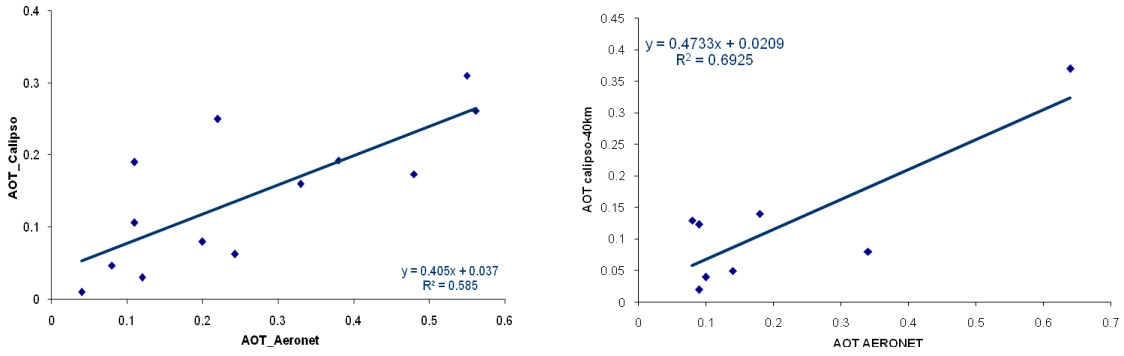

(a)Dunkerque (b) Lille

Fig.3 Comparison of aerosol optical thickness for the available data of CALIPSO and Aeronet network (a) Dunkerque (b) Lille

Figures 3(a) and 3(b) show a good relationship between AOT_ Aeronet and AOT_CALIOP in Dunkerque and Lille. It is observed the slopes of 0.405 and 0.4733 and R; correlation coefficient of 0.76 and 0.83 in Dunkerque and Lille respectively. The figure illustrates that the AOT obtained by CALIPSO have smaller values than AOT of Aeronet data. In the extinction coefficient_532 CALIPSO data in some levels near to ground the aerosol extinction coefficient are not available.

3.3 Relation ship between particle matter concenteration ans aerosol optical thickness

The Hourly average of PM2.5 and AOT of AERONET data at the time of CALIPSO overpass was used for this study. The AOT is the integration of available extinction coefficients of (Level 2- 40 km) data for night or day profiles. Figures 4(a) and 4(b) show the linear regression of the hourly average of PM2.5 versus AOT obtained from CALIPSO and Aeronet data in Lille and Dunkerque. The comparison between PM2.5 and AOT of CALIPSO shows correlation coefficients of 0.7 and 0.73 and slope of 45 and 75 in Dunkerque and Lille respectively.

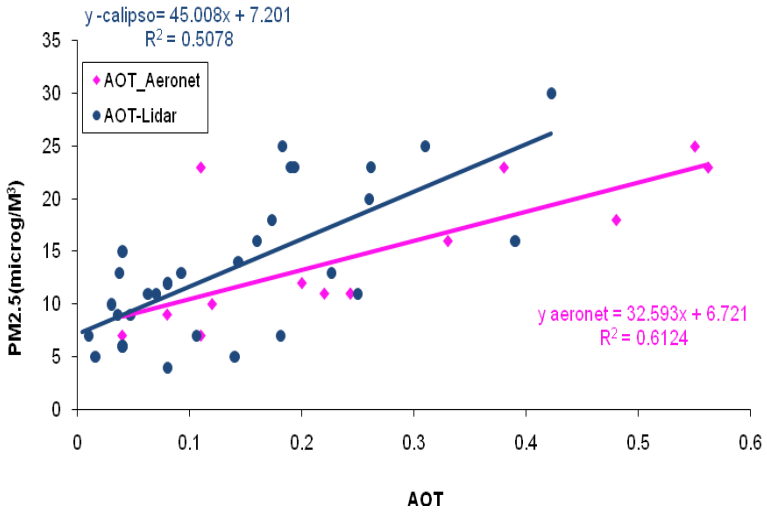

a)Dunkerque

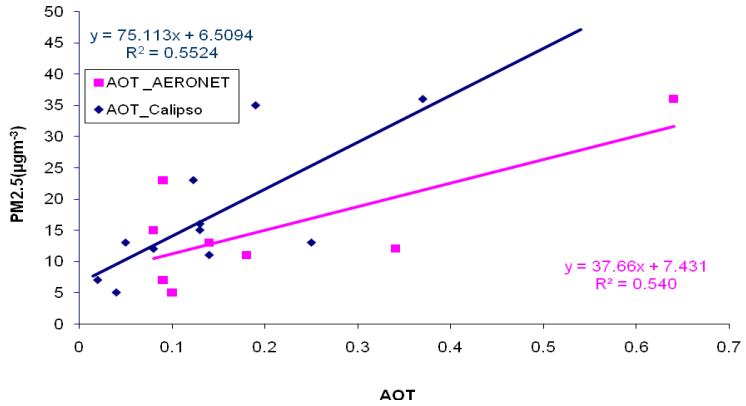

(b)Lille

Fig.4 Hourly average of PM2.5 versus aerosol optical thickness obtained by CALIPSO profiles and Aeronet data in

a) Dunkerque b) Lille

These values are different from CALIPSO data to Aeronet data with correlation coefficient of 0.77 and 0.73 and slope of 32 and 37 (Figures 4a and b). The hourly average of PM2.5 versus AOT has a slope of 45 and 32 and correlation coefficient of 0.7 and 0.77 for

CALIPSO and Aeronet in Dunkerque. Linear equation between PM2.5 and AOT, for CALIPSO data is about two times more than AOT of Aeronet in Lille due to the lower values of aerosol optical thickness obtained by CALIPSO data.

3.4 Aerosol layers (5 km Lidar Aerosol Layer Record)

We have used the Lidar 5 km Column Record in which spatial resolution is 5 km horizontal and these data provide us the integrated attenuated backscatter for 8 level. In this study the layer top and layer base altitude is used which help to study the vertical transport of aerosol. Fig.3 shows the layer top and layer base altitude for two years trace of CALIPSO near to Lille. The aerosol layer height obtained by CALIPSO data – (profiles of days and night time measurement) shows elevated aerosol layer near to 6 km in the troposphere. Using the values of integrated backscatter coefficient which are observed at different altitudes we observed that the contribution of aerosol is about 39% in the altitude between 1km and 2km, 28.57 % in less than 1km and 15.8% between 2km and 3km while 10% of the aerosol layer is observed between 3km and 5km and about 4% at greater than 5km. The average height of the planetary boundary layer which is calculated using the gradient method is about 1.5km. More than 63% of the aerosol layer is observed between 0-1.5km. It is shown that most of the aerosols are in the boundary layer. According to the study on the air pollution episode in April 2007, there is a long range transport of pollution to north of France during April 2007. Consequently the high variations of PM2.5 values were observed on 13 April2007. From CALIPSO data the vertical transport of aerosol is observed up to 3km during this episode of pollution.

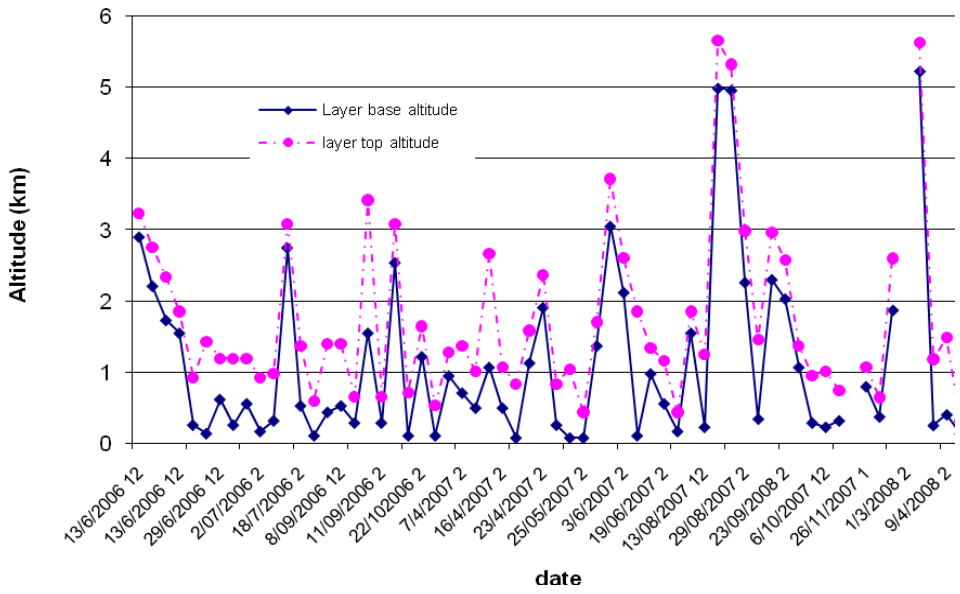

Fig.5 Aerosol layer altitude (CALIPSO level 2-5km data) between 2006 and 2008, day and night time profile.

3.5 Comparison of particle mass concentration and AOT-CALIPSO data

It is important to note that $PM_{2.5}$ and AOT represent two different atmospheric loadings of pollutants. The $PM_{2.5}$ is the dry mass of aerosols measured at ground level and represents the particle mass concentration with aerodynamic diameter less than 2.5 μm. In regions with relatively low dust concentrations, the mineral dust contributes 5–10% to the total $PM_{2.5}$ mass [14]. On the other hand, the extinction coefficient of CALIPSO represents total columnar loading of all aerosol particles from the surface to detector which is averaged over a large spatial area (40km, 5km). Although differences are to be expected in these comparisons, it is important to develop air quality indices based on CALIPSO data especially for regions that have very few ground observations. The relationship between $PM_{2.5}$ (measured at ground) and columnar AOT could also be different due to variations in source regions and aerosol transportation at different heights. The contribution of aerosol in boundary layer could be different in columnar measurements and layers in different heights can have different chemical and physical composition [15]. However, vertical profiles of aerosol obtained from observations show maximum concentrations near-ground and up to the boundary layer [16]

as we observed by CALISO data. The mean $PM_{2.5}$ values are less (from 0 to 25 μg m^{-3}) over clean environments and greater (from 0 to 60 μg m^{-3}) over relatively highly polluted regions or because of long range transport. There are occasions when $PM_{2.5}$ mass values reached more than 60 μgm^{-3} over France which could be attributed to possible local aerosol events reported in surrounding areas or long range transported that are not included in this data because of CALIPSO traces. Here we use the hourly average of PM2.5 obtained by automatic stations (TEOM).There are 20 urban and periurban stations in France. The nearest distance between the stations and CALIPSO trace is less than 30 km. Figure 6 shows the PM2.5 versus AOT for two years of observations. There are the low values of AOT with high values of PM2.5 which are related to some profiles in that one level of measurement exists. At first we have studied the relationship between extinction coefficient and PM2.5 in the different levels (below 1000 m). Even if PM2.5 is measured at the ground level, we did not find any significant relationship between PM2.5 and extinction coefficient measurement near to the ground (127m). There is not enough available data near to the ground. Among 18 stations, the 15 stations show the slope of 57.59 and coefficient correlation of 0.75 for PM2.5 versus AOT of CALIPSO measurements. There are many factors that can affect the relationship between AOT_CALIOP and PM2.5. The AOT of CALIOP provides columnar information for ambient conditions whereas PM2.5 measurements are representative of near-surface dry mass concentration. CALIPSO represents large spatial areas and PM2.5's are local measurement and they do not capture pollution over large areas. Meanwhile the meteorological conditions especially relative humidity can affect this relationship.

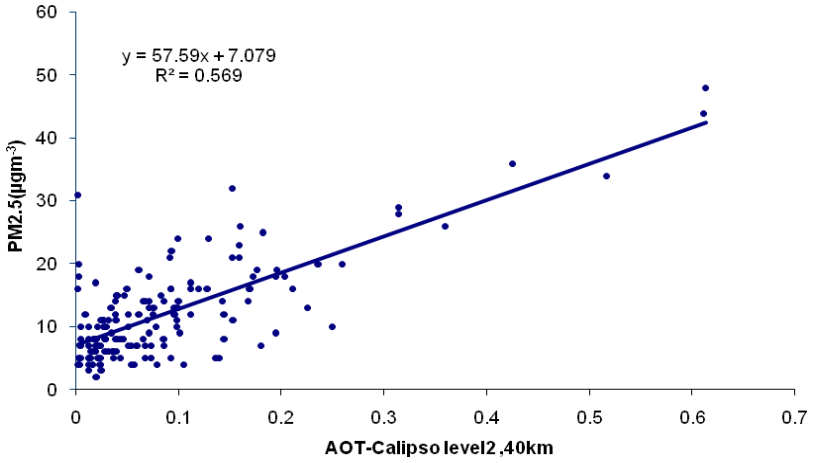

Fig.6 Hourly average of PM2.5 versus AOT-obtained by CALIPSO data over France between 2006 and 2008

4. Conclusion and further research

Using RMS analysis, the empirical relationship between hourly mass concentration (μgm^{-3}) and CALIOP AOT (532nm) shows that the CALIOP derived AOT is a good tool for air quality study over large spatial areas. Since PM2.5 represents point observations they do not capture the pollution over large areas and CALIPSO data can be used in areas where measurement of pollution is not available and surface measurements cannot capture the nature of some source of pollution. The vertical transportation of pollution can be examined and we see the aerosol layers are located in higher altitude for in Lille (continental location) compared to Dunkerque (industrial - maritime). The combination of CALIPSO and ground-based measurement PM2.5 monitoring data and Aeronet data can form the basis of an integrated characterization of air quality in 3 dimensions.

There are a number of steps that need to be taken to further the understanding and applicability of these datasets. Further work needs to be conducted to better understand the quantitative relationships between Lidar-CALIPSO, ground –based Lidar and PM2.5 monitors and sun photometer. Lidar data for more regions and for longer period are needed to define effect of other variables on the variability of the PM2.5 –AOT relationship such as relative humidity, temperature and geospatial biases. These could help to correct for aerosol

height for meteorological effects and may improve the PM2.5- AOT relationship. Extinction data from CALIPSO and ground base systems can determine the impact of regional transport as well as local transport on aerosol load.

References

[1] Gupta, P., Christopher, S. A., Wang, J., Gehrig, R., Lee, Y. C., and Kumar, N.: 2006, "Satellite remote sensing of particulate matter and air quality over global cities", Atmos. Environ., 40(30), 5880– 5892 (2006).

[2] Kim. S.- W et al., "Validation of aerosol and cloud layer structures from the space borne Lidar CALIOP using Seoul National University ground-based Lidar", Atmos. Chem. Phys, 7, 11207-11222 (2007)

[3] Wakimoto, R.M., McElroy, J.L., 1986. "Lidar observation of elevated pollution layers over Los Angeles" J. Clim. Appl. Meteorol. 25, 1583– 1599 (1986).

[4] Holben, B. N., et al. "AERONET—A federated instrument network and data archive for aerosols characterization", Remote Sens. Environ., 66, 1 –16 (1998).

[5] Klett, J. D., "Stable analytical inversion for processing Lidar returns", *Appl. Opt.*, **20,** 211- 220 (1981).

[6] Fernald, F.G., B. M. Herman and J. A. Reagan, "Determination of aerosol height distributions with Lidar", *J. Appl. Meteorol.,* **11,** 482-489(1972).

[7] Stuart A. Young et al, "CALIOP algorithm theoretical basic document: part 4, extinction retrieval algorithm" (2008).

[8] Liu, Z., M. Vaughan, D. Winker, C. Hostetler, L. Poole, D. Hlavka, W. Hart, and M. McGill, " Use of probability distribution functions for discriminating between cloud and aerosol in Lidar backscatter data" , *J. Geophys. Res.* 109, D15202 (2004)

[9] pinhirne et al, "vertical distribution of aerosol extinction cross section and inference of aerosol imaginary index in the troposphere by Lidar technique", *J. APPL. METEO*., 19, 426-438 (1979).

[10] Wang. X et al, " Retrieval of atmospheric particles optical properties by combining ground-based and space borne Lidar elastic scattering profiles", Opt. Press, 11,vol. 15, 6734-6743 (2007).

[11] Fernald, F.G., B. M. Herman and J. A. Reagan, "Determination of aerosol height distributions with Lidar", *J. Appl. Meteorol.,* **11,** 482-489 (1972).

[12] Platt, C. M. R., "Lidar and radiometer observations of cirrus clouds", *J. Atmos. Sci.,* **30**, 1191-1204 (1973).

[13] Sassen, K., and B. S. Cho,"Sub-visual thin cirrus Lidar dataset for satellite verification and climatologically research" *J. Appl. Meteor.,* **31**, 1275-1285 (1992).

[14] Hueglin, R. Gehrig, U. Baltensperger, M. Gysel, C. Monn and H. Vonmont, "Chemical characterisation of PM2.5, PM10 and coarse particles at urban, near-city and rural sites in Switzerland", *Atmospheric Environment* **39**, 637– 651 (2005).

[15] Franke, K, A. Ansmann, D. Müller, D. Althausen, C. Venkataraman, M.S. Reddy, F. Wagner and R. Scheele, "Optical properties of the Indo-Asian haze layer over the tropical Indian Ocean", *J. o Geoph. Res.* **108**, 4059 (2003)

[16] Kaufman. Y.J., J.M. Haywood, P.V. Hobbs, W. Hart, R. Kleidman and B. Schmid, "Remote sensing of vertical distributions of smoke aerosol off the coast of Africa", *Geophysical Research Letters* 30, **16**, 1831 (2003)